

5

3429

3430

3431

Longevity studies and Consolidation of the present CMS RPC system

3432 The RPC system, located in both barrel and endcap regions, provides a fast, independent muon
3433 trigger over a large portion of the pseudo-rapidity range ($|\eta| < 1.6$). During HL-LHC operations
3434 the expected conditions in terms of background and pile-up will make the identification and correct
3435 p_T assignment a challenge for the muon system. The goal of the RPC upgrade is to provide additional
3436 hits to the Muon System with more precise timing. All this information will be elaborated by the
3437 Trigger System in a global way enhancing the performance of the muon trigger in terms of efficiency
3438 and rate control. The RPC Upgrade consists of two projects: an improved Link Board System and
3439 the extension of the RPC coverage up to $|\eta| = 2.4$.

3440 The Link Board System is responsible for the processing, the synchronization and the zero-
3441 suppression of the signals coming from the RPC FEBs. The Link Board components have been
3442 produced between 2006 and 2007 and will be subjected to ageing and failure on a long term scale.
3443 An upgraded Link Board System will overcome the ageing problems and will allow for a more
3444 precise timing information to the RPC hits from 25 to 1.5 ns.

3445 In order to develop an improved RPC that fulfills CMS requirements, an extensive R&D program is
3446 being conducted. The benefits of adding two new RPC layers in the innermost ring of stations 3 and
3447 4 will be mainly observed in the neutron-induced background reduction and efficiency improvement
3448 for both the muon trigger and the offline reconstruction.

3449 The coverage of the RPC System up to higher pseudo-rapidity $|\eta| = 2.1$ was part of the original
3450 CMS TDR. Nevertheless, the expected background rates being higher than the certified rate capa-
3451 bility of the present CMS RPCs in that region and the budget being limited, RPCs were restricted to
3452 a smaller pseudo-rapidity range. Even though the iRPC technology that will equip the extension of
3453 the Muon System will be different than the current CMS RPC technology, it is necessary to certify
3454 the rate capability and longevity of the existing detectors as the radiation level will increase together
3455 with the increase of instantaneous luminosity of the LHC. For this purpose, unused spare CMS RPC
3456 detectors have been installed in different irradiation facilities, first of all, to certify the detectors to

the new levels of irradiation they will be subjected to and, finally, to study their ageing and certify their good operation throughout the HL-LHC program.

This chapter will discuss the longevity and consolidation studies of the present CMS RPC system to which I have contributed. Two different irradiation facilities have been used at CERN. In each of them I took a leading role in defining the experimental set-up, but also in the data collection and data analysis. In the first facility in which preliminary tests were conducted, I also worked on simulations of the experimental setup and I made predictions on the particle rate expected at the detector level. During the last 4 years of longevity test conducted in the second facility, I became a DAQ expert and built a software which is now the base for the data collection to study the longevity of CMS RPCs. Moreover, I also worked together with the Detector Control Software (DCS) expert to provide an online monitoring of the collected data. Indeed, I developed a software that automates the extractions of the detectors' data and produces plots at destination of the users thanks to a fast analysis. This software is a corner stone for the final data analysis. Documentations of both these softwares are given in Appendix A and Appendix B.

In a first section of the chapter, the irradiation facilities will be described. The study conducted will then be summarized in details. A description of the set-ups as well as a comprehensive review of the obtained results will be provided.

5.1 Testing detectors under extreme conditions

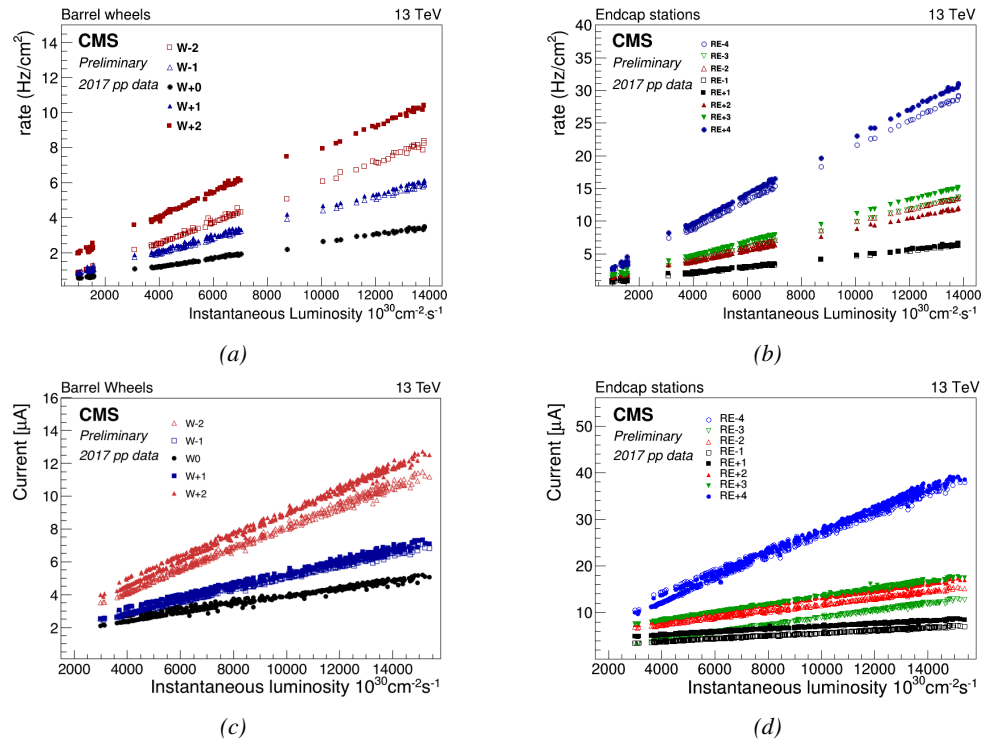


Figure 5.1: Mean RPC Barrel (left column) and Endcap (right column) rate (top row) and current (bottom row) as a function of the instantaneous luminosity as measured in 2017 p-p collision data.

The upgrade from LHC to HL-LHC will increase the peak luminosity from 10^{34} $\text{cm}^{-2} \text{s}^{-1}$ to 5×10^{34} $\text{cm}^{-2} \text{s}^{-1}$, increasing the total expected background to which the RPC system will be subjected. Mainly composed of low energy gammas, neutrons, and electrons and positrons from $p\text{-}p$ collisions, but also of low momentum primary and secondary muons, punch-through hadrons from calorimeters, and particles produced in the interaction of the beams with collimators, the background will mostly affect the regions of CMS that are the closest to the beam line, i.e. the RPC detectors located in the endcaps.

Data collected during 2017, presented in Figure 5.1, allows to study the values of the background rate in the entire RPC system. This was achieved thanks via the monitoring of the rates in each RPC rolls and of the current in each HV channel. A linear dependence of the mean rate or current on the instantaneous luminosity is shown in selected runs with identical LHC running parameters. It is assumed that such a linear behaviour should be observed at even higher luminosities and is therefore used to extrapolate the rates and currents that will be expected during HL-LHC. In Figure 5.2, a linear extrapolation of the distribution of the background hit rate per unit area as well as the integrated charge is shown at a HL-LHC condition. The maximum hit rate per unit area in the endcap detectors at HL-LHC conditions is expected to be of the order of 600 Hz/cm² while the charge deposition should exceed 800 mC/cm². The detectors will thus have to be certified up to an irradiation of 840 mC/cm². These extrapolations are provided with a required safety factor 3 for the certification study.

In the past, extensive long-term tests were carried out at several gamma and neutron facilities certifying the detector performance. Both full size and small prototype RPCs have been irradiated with photons up to an integrated charge of $\sim 0.05 \text{ C/cm}^2$ and $\sim 0.4 \text{ C/cm}^2$ respectively and were certified for rates reaching 200 Hz/cm² [262, 263]. Since the beginning of Run-I until December 2017, the RPC system provided stable operation and excellent performance. The average integrated charge is of about 1.66 mC/cm² in the Barrel and 4.58 mC/cm² in the Endcap, closer to the beam line, as can be seen in Figure 5.3). The detectors did not show any ageing effects for a maximum integrated charge in a detector of the order of 0.01 C/cm² and a peak luminosity reaching 1.4×10^{34} $\text{cm}^{-2} \text{s}^{-1}$ during the 2017 data taking period.

To perform the necessary studies on the present CMS RPC detectors, facilities offering the possibility to irradiate the chambers are necessary in order to recreate HL-LHC conditions or stronger and

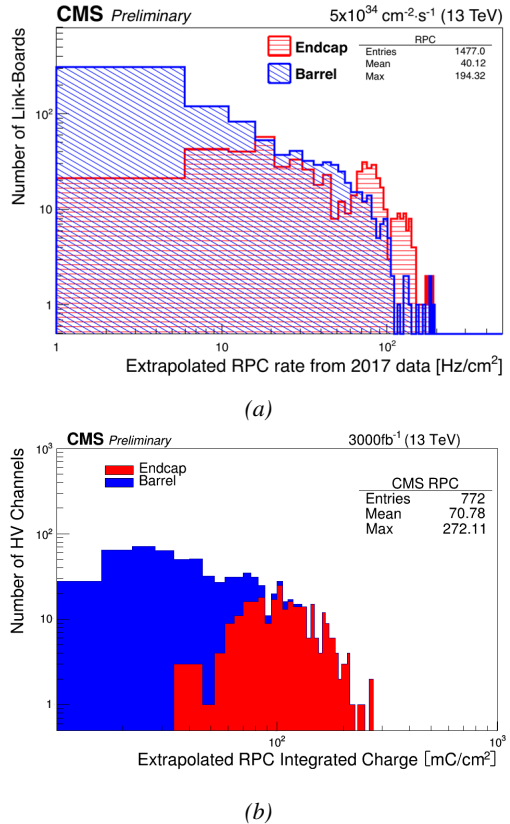


Figure 5.2: Linear extrapolation of the hit rate (a) and of the integrated charge (b) per region (Barrel, Endcap) respectively to HL-LHC instantaneous luminosity ($5 \times 10^{34} \text{ cm}^{-2} \text{s}^{-1}$) and HL-LHC integrated luminosity (3000 fb^{-1}).

study the detector performance through time. A first series of such studies was conducted in the former Gamma Irradiation Facility (GIF) of CERN before its dismantlement starting from September 2014. This preliminary study was used as a stepping stone towards the building of a more powerful irradiation fully dedicated to longevity studies of CMS and ATLAS subsystems in the perspective of HL-LHC. The period of preliminary work has also been a key moment in the elaboration and improvement of data acquisition, offline analysis and online monitoring tools that are extensively used in the new gamma irradiation facility.

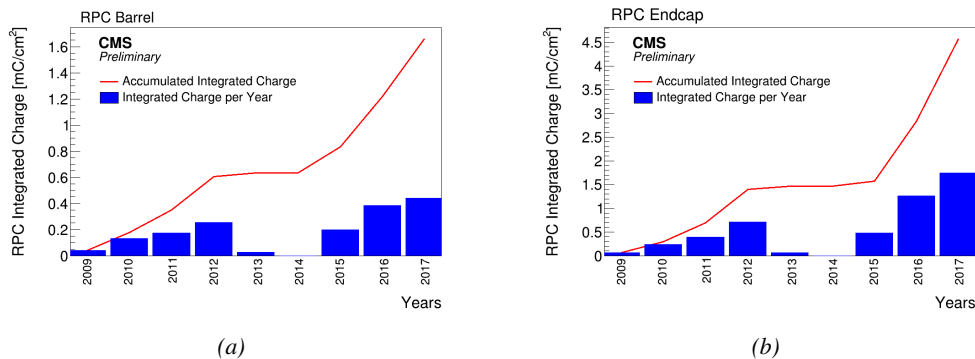


Figure 5.3: CMS RPC mean integrated charge in the Barrel region (a) and the Endcap region (b). The integrated charge per year is shown in blue. The red curve shows the evolution of the accumulated integrated charge through time. The blank period in 2013 and 2014 corresponds to LS1.

5.1.1 The Gamma Irradiation Facility

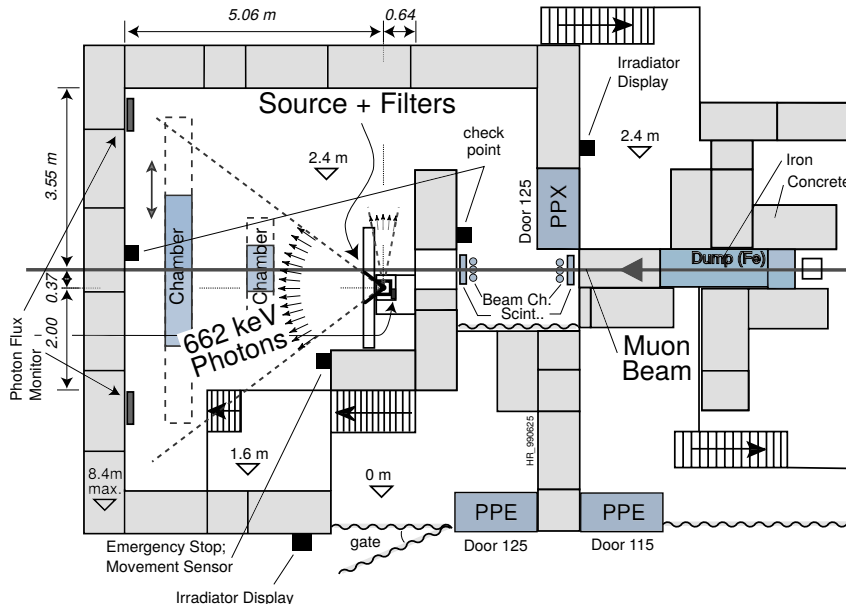


Figure 5.4: Layout of the test beam zone of GIF at CERN.

3529 Located in the SPS West Area at
 3530 the downstream end of the X5 test beam, the GIF was a test area in
 3531 which particle detectors were exposed to a particle beam in presence of an adjustable gamma background [264]. Its goal was to reproduce background conditions these detectors would endure in their operating environment at LHC. The layout of the GIF is shown in Figure 3538
 3539 5.4. Gamma photons are produced by a strong ^{137}Cs source installed in the upstream part of the zone inside
 3540

3541 a lead container. The source container includes a collimator, designed to irradiate a $6 \times 6 \text{ m}^2$ area at
 3542 5 m maximum distance to the source. A thin lens-shaped lead filter helps providing with a uniform
 3543 out-coming flux in a vertical plane, orthogonal to the beam direction. The photon rate is controlled
 3544 by further lead filters allowing the maximum rate to be limited and to vary within a range of four
 3545 orders of magnitude. Particle detectors under test are then placed within the pyramidal volume in
 3546 front of the source, perpendicularly to the beam line in order to profit from the homogeneous photon
 3547 flux. Adjusting the background flux of photons can then be done using the filters and choosing the
 3548 position of the detectors with respect to the source. The zone is surrounded by 8 m high and 80 cm
 3549 thick concrete walls. Access is possible through three entry points. Two access doors for personnel
 3550 and one large gate for material. A crane allows installation of heavy equipment in the area.
 3551

3552 As described on Figure 5.5, the ^{137}Cs source emits a 662 keV photon in 85% of the decays. An
 3553 activity of 740 GBq was measured on the 5th of March 1997. The half-life of Cesium is well known
 3554 ($t_{1/2} = (30.05 \pm 0.08) \text{ y}$) and can be used to compute the activity of the source at the time of the
 3555 study. The GIF tests were done in between the 20th and the 31st of August 2014, i.e. at a time $t =$
 3556 (17.47 ± 0.02) y resulting in an attenuation of the activity from 740 GBq in 1997 to 494 GBq in
 3557 2014.
 3558

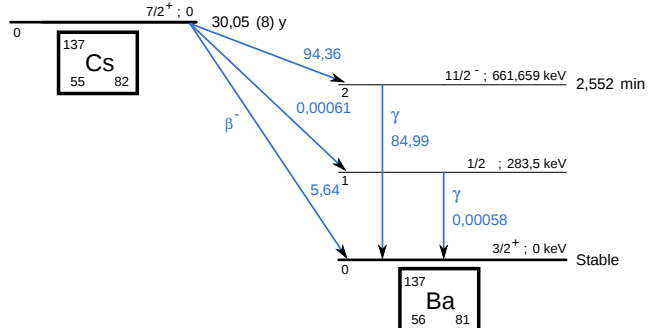


Figure 5.5: ^{137}Cs decays by β^- emission to the ground state of ^{137}Ba ($BR = 5.64\%$) and via the 662 keV isomeric level of ^{137}Ba ($BR = 94.36\%$) whose half-life is 2.55 min.

3559 5.1.2 The new Gamma Irradiation Facility

3560 The GIF++, located in the SPS North Area at the downstream end of the H4 test beam, has replaced
 3561 its predecessor during LS1 and has been operational since spring 2015 [265]. Like GIF, GIF++
 3562 features a ^{137}Cs source of 662 keV gamma photons, their fluence being controlled with a set of
 3563 filters of various attenuation factors. The source provides two separate large irradiation areas for
 3564 testing several full-size muon detectors with homogeneous irradiation, as presented in Figure 5.6.
 3565

3566 The source activity was measured to be about 13.5 TBq in March 2016. With the photon flux
 3567 being far greater than HL-LHC expectations, GIF++ provides an excellent facility for accelerated
 3568 ageing tests of muon detectors. The source is situated in a bunker designed to perform irradiation
 3569 test along a muon beam line, which is available during selected periods throughout the year.
 3570 The H4 beam, providing the area with muons with a maximum momentum of about 150 GeV/c,
 3571 passes through the GIF++ zone and is used to periodically study the performance of the detectors
 3572 placed under long term irradiation. Its flux is of 104 particles/s/cm² focused in an area of about
 3573 $10 \times 10 \text{ cm}^2$.

	1	2	3
A	1	10	100
B	1	1.468	100
C	1	2.154	4.642

Table 5.1: Attenuation of single filters on each filter plane of the GIF++ Cesium source.

attenuation factor (for example $333 = 100 \times 100 \times 4.642 = 46420$).

Adjusting the gamma flux is possible thanks to the three planes (A, B and C) of adjustable absorbers featured on the Cesium source [266]. With properly adjusted filters, one can simulate the background expected at HL-LHC and study the performance and ageing of muon detectors in HL-LHC environment. Each plane of filters features three filters (1, 2 and 3) with different Absorption factor (ABS) listed in Table 5.1. The source absorber settings can be referred by a three digit number with a format ABC or by its

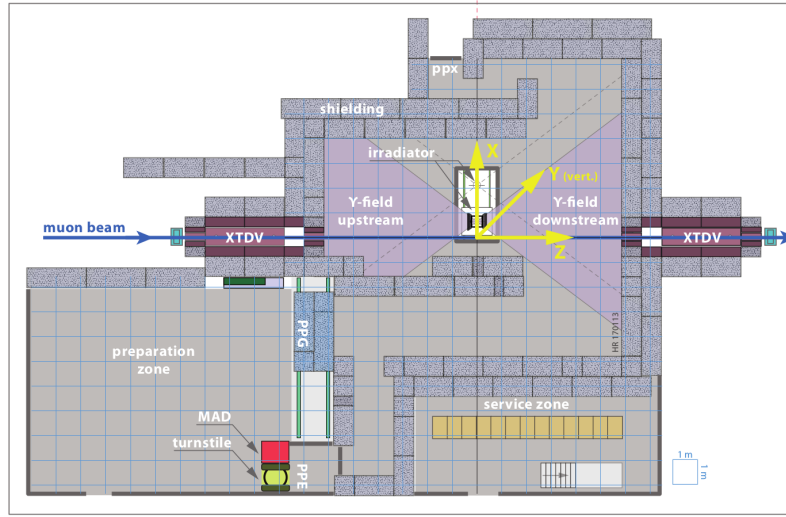


Figure 5.6: Floor plan of the GIF++ facility. When the facility downstream of the GIF++ takes electron beam, a beam pipe is installed along the beam line (z -axis). The irradiator can be displaced laterally (its center moves from $x = 0.65$ m to 2.15 m), to increase the distance to the beam pipe.

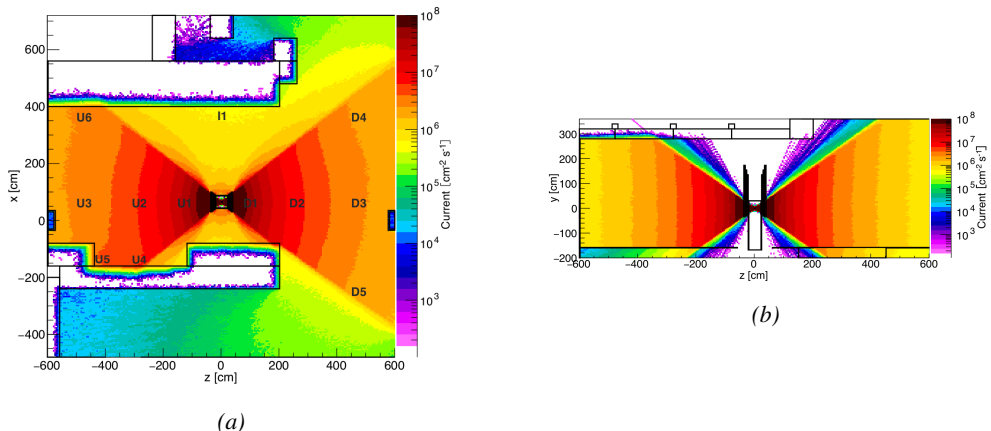


Figure 5.7: Simulated unattenuated current of photons in the xz plane (a) and yz plane (b) through the source at $x = 0.65$ m and $y = 0$ m [267]. With angular correction filters, the current of 662 keV photons is made uniform in xy planes.

The gamma current as simulated with GEANT4 is presented in Figure 5.7. In their simulation paper [267], Pfeiffer et al. define the particle current as "a measure of the net number of particles crossing a flat surface with a well-defined orientation. The unit of current is $\text{m}^{-2} \text{s}^{-1}$ and thus identical to the unit of flux. Current is meaningful in cases where particles are counted without any interest in their interactions." The labels UN, DN, with $N \in [1 : 5]$ and I1 correspond to the position of different Radiation Monitoring (RADMON) sensors measuring the irradiation in the bunker area [267]. According to the simulation results, that agree within 12% to the doses measured with the RADMONs, the RPCs that will be tested in GIF++ can expect a maximal gamma current of the order of 2 to $5 \times 10^6 \text{ cm}^{-2} \text{s}^{-1}$ assuming they will always stay in a region in between sensor U5 and the back wall of the upstream area.

5.2 Preliminary studies at GIF

5.2.1 RPC test setup

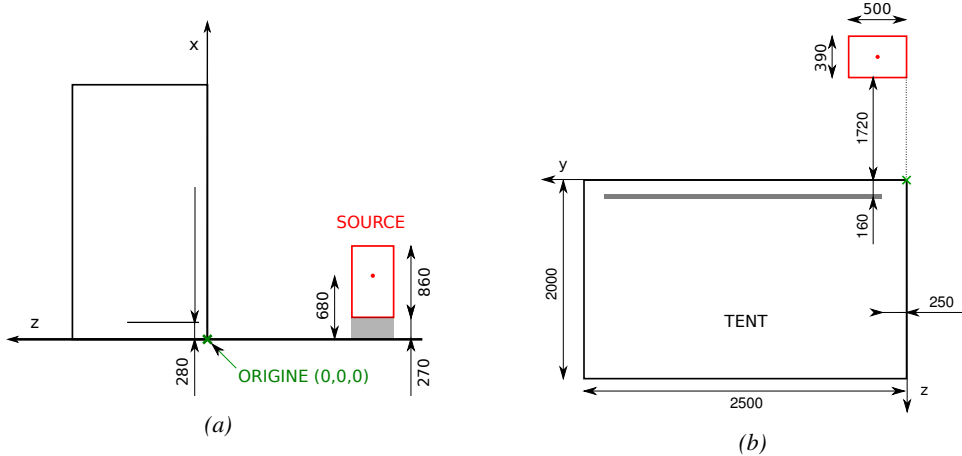


Figure 5.8: Description of the RPC setup. Dimensions are given in mm. A tent containing RPCs is placed at 1720 mm from the source container. The source is situated in the center of the container. RE-4-2-BARC-161 chamber is 160 mm inside the tent. This way, the distance between the source and the chambers plan is 2060 mm. Figure (a) provides a side view of the setup in the xz plane while Figure (b) shows a top view in the yz plane.

During Summer 2014, preliminary tests have been conducted in the GIF area on an endcap chamber of type RE4/2 and labeled RE-4-2-BARC-161 produced for the extension of the endcap with a fourth disk in 2013. This chamber has been placed into a trolley covered with a tent in order to control the temperature. The positions of the RPC inside the tent and of the tent with respect to the source in the bunker are described in Figure 5.8. The goal of the study was to have a preliminary understanding of the rate capability of the present technology used in CMS. It was decided to measure the efficiency of the RPC under irradiation for detecting cosmic muons as, at the time of the tests, the beam was not operational anymore. Three different absorber settings were used and compared to the case where the detector was not irradiated in order to study the evolution of the performance of the detector with increasing exposure to gamma radiation. First of all, measurements were done with the fully opened source. To complete this preliminary study, the gamma flux has been attenuated by

3605 a factor 2, a factor 5 and finally the source was shut down. The efficiency of the RPC at detecting
 3606 the cosmic muons in coincidence with a cosmic trigger as well as the background rate as seen by the
 3607 detectors were measured.

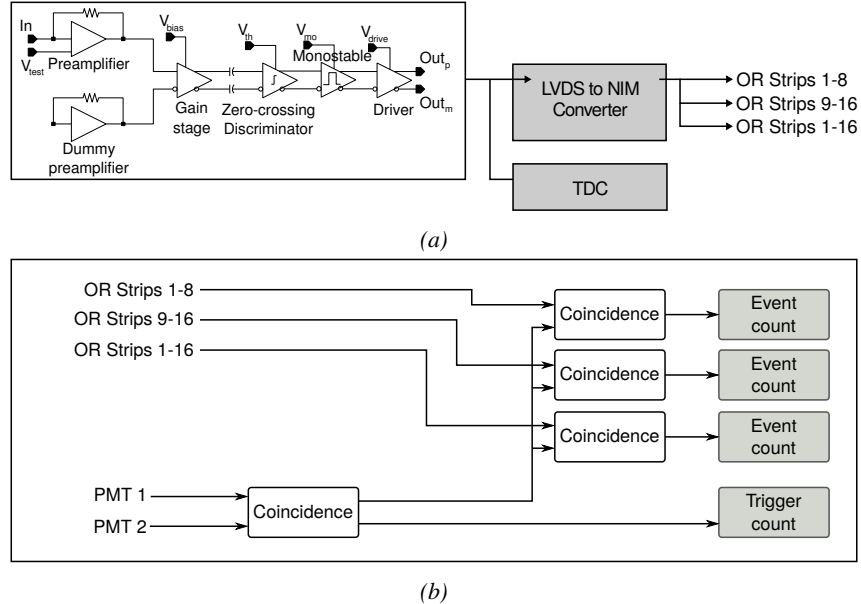


Figure 5.9: (a) Shaping of the signals from the RPC strips by the FEE. The output LVDS signals are then read-out by a TDC module connected to a computer or converted into NIM and sent to scalers. (b) Trigger logic implementation with the RPC and photomulitplier signals.



Figure 5.10: RE-4-2-BARC-161 chamber is inside the tent as described in Figure 5.8. In the top right, the two scintillators used as trigger can be seen.

3621
 3622
 3623
 3624
 3625
 3626
 3627
 libraries and the data collected by the TDCs was saved into .dat files is analysed with an algorithm
 computing parameters such as efficiency, hit profile, cluster size, or gamma and noise rates which
 was developed with C++ as well. Finally, histograms and curves are produced using ROOT.

The data taking was performed using a CEAN TDC module of type V1190A [268] to which the digitized output of the RPC Front-End Board is connected, as described in Figure 5.9a and the trigger signal from the telescope. The communication with the computer is performed thanks to a CAEN communication module of type V1718 [269]. In order to control the rates recorded by the detector, the digitized RPC signals are also sent to scalers as described in Figure 5.9b. The C++ DAQ software used in GIF was developed as an early attempt towards the understanding of the CAEN li-

3628 The trigger system was com-
 3629 posed of two plastic scintillators and
 3630 was placed in front of the setup with
 3631 an inclination of 10° with respect to
 3632 the detector plane in order to look at
 3633 cosmic muons. Using this particular
 3634 trigger layout, shown in Figure 5.10,
 3635 lead to a cosmic muon hit distribution
 3636 into the chamber similar to the
 3637 one of Figure 5.11. As mentioned
 3638 in Chapter 2, the endcap RPC read-
 3639 out is segmented into three pseudo-
 3640 rapidity partitions. The outer most
 3641 partition, corresponding to the wide
 3642 end of the chamber, is the partition
 3643 A. The other two partitions are the
 3644 partitions B and C. Each of them
 3645 consists in 32 copper strips. These
 3646 32 strips are connected to the FEEs
 3647 by groups of 16. The trigger is
 3648 placed in front of the half-partition
 3649 B2 which corresponds to the last 16 strips of partition B (49 to 64).

3650 Measured without gamma irradiation, two peaks can be seen on the profile of readout partition
 3651 B, centered on strips 52 and 59. Some events still occur in other half-partitions than B2 contributing
 3652 to the inefficiency of detection of cosmic muons. In the case of partitions A and C, the very low
 3653 amount of data can be interpreted as noise. On the other hand, it is clear that a little portion of
 3654 muons reached the half-partition B1 (strips 33 to 48). Section 5.2.2 will help us understand that
 3655 these two peaks are due respectively to forward and backward coming cosmic particles. Forward
 3656 coming particles are detected first by the scintillators and then the RPC while the backward going
 3657 muons are first detected in the RPC.

3658 **5.2.2 Geometrical acceptance of the setup layout to cosmic muons**

3659 In order to profit from a constant gamma irradiation, the detectors inside of the GIF bunker had to be
 3660 placed in a plane orthogonal to the beam line. The muon beam that used to be available was meant to
 3661 test the performance of detectors under test. This beam being not active anymore, another solution
 3662 to test detector performance had to be used. Thus, it was decided to use cosmic muons detected
 3663 through a telescope composed of two scintillators. Lead blocks were used as shielding to protect the
 3664 photomultipliers from gammas as can be seen from Figure 5.10.

3665 An inclination of $\sim 10^\circ$ was given to the cosmic telescope to increase the muon trigger rate for
 3666 this otherwise horizontal setup. A good compromise had to be found between good enough muon
 3667 flux and narrow enough hit distribution to be sure to contain all the events into a single half-partition
 3668 as required from the limited available readout hardware. It was then foreseen to detect muons and
 3669 read them out only from half-partition B2. Nevertheless, a misplacement of the trigger scintillators
 3670 resulted in an inefficiency, as can be seen in Figure 5.11 with events appearing in half-partition B1.

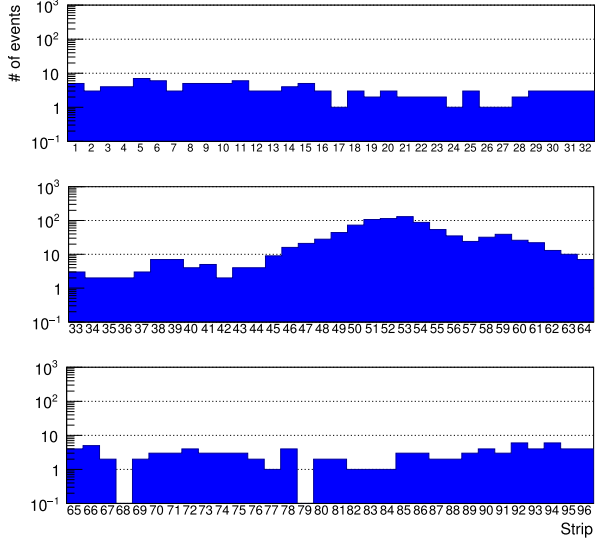


Figure 5.11: Hit distributions over all three partitions of RE-4-2-BARC-161 chamber is showed. Top, middle and bottom figures respectively correspond to partitions A, B, and C.

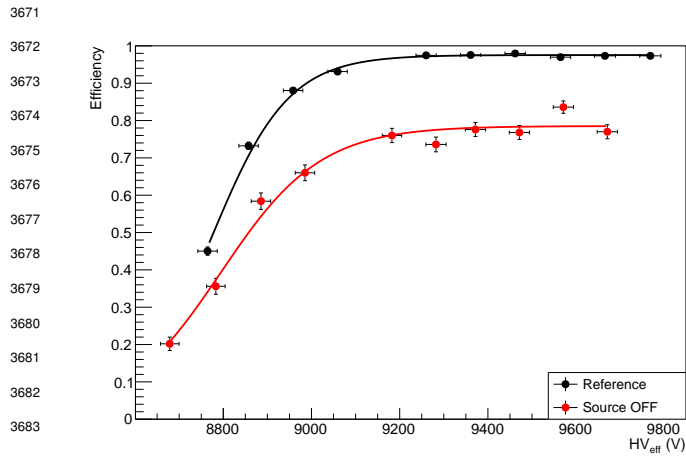


Figure 5.12: Comparison of the efficiency of chamber RE-4-2-BARC-161 with and without irradiation. Results are derived from data taken on half-partition B2 only.

by the red curve. The inefficiency too high compared to the 12.7% of data contained into the first 16 strips observed on Figure 5.11, to be explained only by the geometrical acceptance of the setup itself. Simulations have been conducted to quantify the inefficiency of the setup.

5.2.2.1 Geometrical acceptance simulation setup

The layout of the GIF setup has been reproduced¹ and incorporated into a C++ Monte Carlo (MC) simulation to study the geometrical acceptance of the telescope projected onto the readout strips [270]. A 3D view of the simulated layout is given into Figure 5.13. The RPC read-out plane is represented as a yellow trapezoid while the two scintillators as blue cuboids. The green plane corresponds to the $4 \times 4.5 \text{ m}^2$ muon generation plane centered on the experimental setup within the simulation. The goal of the simulation is to look at muons that pass through the telescope composed of the two scintillators and define their distribution onto the RPC read-out plane. During the reconstruction, the read-out plane is then divided into its read-out strips and each muon track is assigned to a strip.

$N_\mu = 10^8$ muons are generated at a random position in the horizontal generation plane. This position corresponds to the intersection of the muon track with the generaltion plane. The plane is located at a height corresponding to the lowest point of the scintillators in order to easily simulate muons coming at very large zenith angles (i.e. $\theta \approx \pi$). The position of the particle within the plane is associated with a random direction: an azimuth angle ϕ chosen between 0 and 2π and a zenith angle θ chosen between 0 and $\pi/2$ to follow a usual $\cos^2\theta$ distribution for cosmic particles. Then, using the position of the muon in the generation plane and its direction, the intersection of the track with the planes of the scintillator cuboids is computed. In the case the muon wasn't found within the surface of both the scintillators, the simulation restarts and generates a new muon. On the contrary, if the track passed through the telescope, the simulation goes on. The position of the muon hit within the RPC read-out plane is computed. The hits are saved into histograms, one per read-out partition,

As can be seen in Figure 5.12, a comparison of the performance of chamber RE-4-2-BARC-161 with and without irradiation suggests an inefficiency of approximately 20%. On the 18th of June 2014, data have been taken on the chamber at CERN building 904 (Prevessin Site) with cosmic muons providing us a reference efficiency plateau of $(97.54 \pm 0.15)\%$ represented by the black curve. A similar measurement has been done at GIF on the 21st of July with the same chamber giving a plateau of $(78.52 \pm 0.94)\%$ represented

¹Albeit only roughly using Figure 5.10 due to the lack of actual measurements of the respective positions of each parts of the experimental setup. Using reference dimensions such as the saize of the detector and the size of the photomultiplier, the positions could be deduced.

whose bins corresponds to the RPC copper strips. The strip in which the hit occured is determined by knowing precisely the geometry of the RPC. Muon hits are also filled in different histograms whether they are associated to forward coming ($\pi \leq \phi < 2\pi$) or backward going ($0 \leq \phi < \pi$) muons.

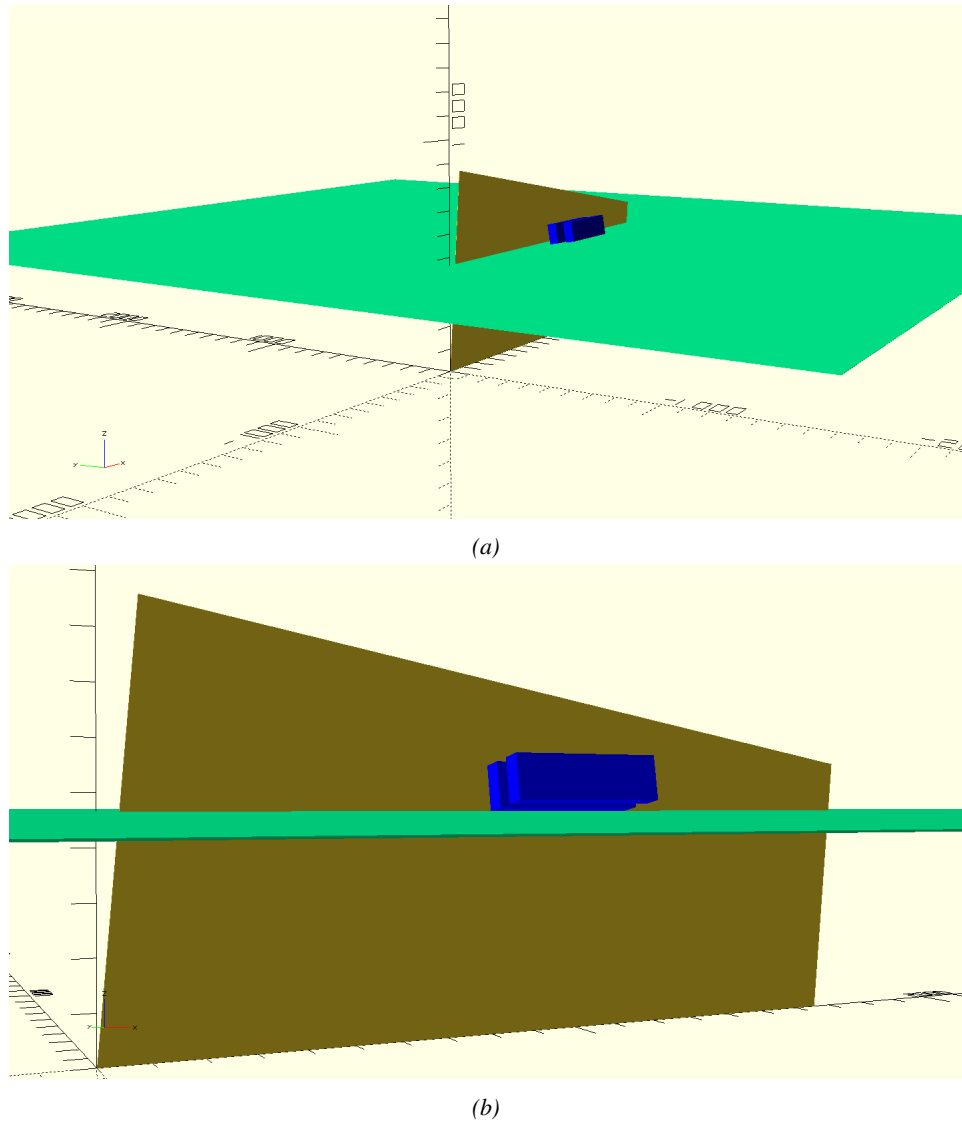


Figure 5.13: Representation of the layout used for the simulations of the test setup. (a) Global view of the simulated setup. (b) Zoomed view on the experimental setup.

5.2.2.2 Results and limitations

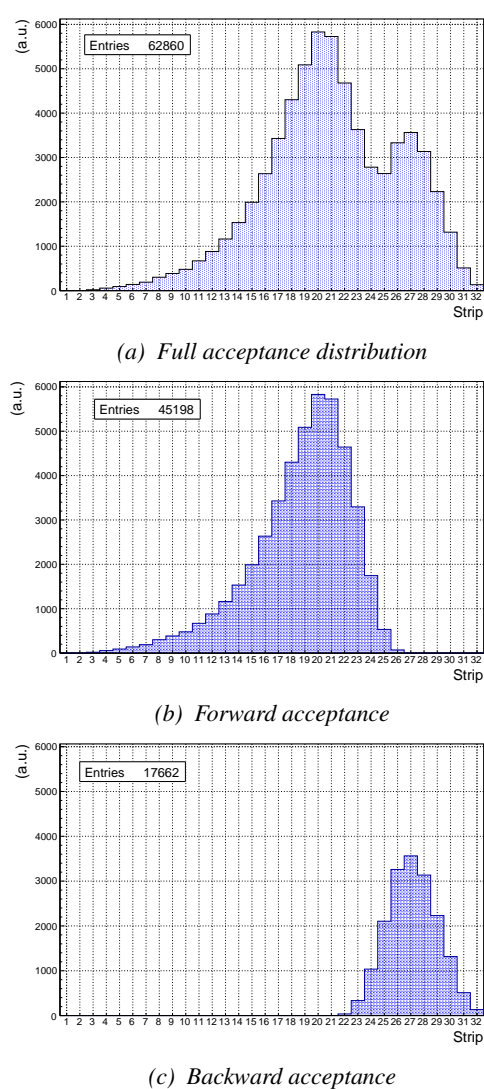


Figure 5.14: Geometrical acceptance distribution as provided by the Monte Carlo simulation.

affected by a variation of the inclination angle, as can be seen in Figure 5.16. Yet, the position of the acceptance peaks in the distribution would be in agreement with what is measured, and the contribution of farward and backward muons would never reach the observation. With an inclination of 10° , 28.1% of the total geometrical acceptance should contribute to detecting backward muons whereas it is measured that the hit profile contains 22.0% of backward data only. Introducing in the simulation an error of $\pm 2^\circ$ would lead to a correction factor $c_{geo} = 1.20^{+0.04}_{-0.03}$ allowing for a good improvement of the efficiency measured in GIF, as can be seen from Figure 5.17. GIF measurement is in agreement with the reference curve within statistical errors.

The output from the simulation is given in Figure 5.14 in which the geometrical acceptance distribution of the setup is shown. The distributions for the separate contributions of forward coming and backward going muons are all provided. The strip number is given in a range of 1 to 32 corresponding to the 32 strips contained in each RPC read-out partition even though partition B correponds, by convention, to strip numbers 33 to 64. It can be established than, out of the total amount of muons that have passed through the telescope and reached the RPC, 16.8% were hitting the 16 first strip of the read-out plane corresponding to half partition B1. This number corresponds to the inefficiency. It can be used then to correct the data by scaling up by a factor $c_{geo} = 1/(1 - 0.168)$ the efficiency measured during data taking.

Nevertheless, the distribution showed in Figure 5.14a differs from the measured hit profile showed in Figure 5.11 as can be seen in Figure 5.15. It is difficult to evaluate a systematic uncertainty on this geometrical correction for different reasons.

First of all, even though the dimensions of the scintillators and of the RPC are well known, the position of each element of the setup with respect to one another was not measured. The extraction of the position of each part of the setup from Figure 5.10 was a first large source of error.

The inclination is also roughly measured to be 10° bringing more uncertainty into the simulation. The acceptance distribution would be

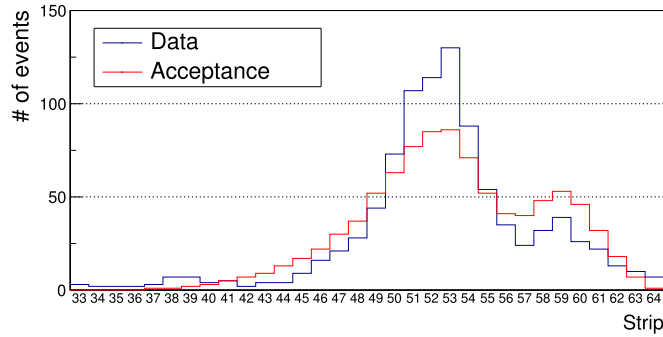


Figure 5.15: Comparison of the hit distribution recorded in the detector and of the normalised geometrical acceptance distribution.

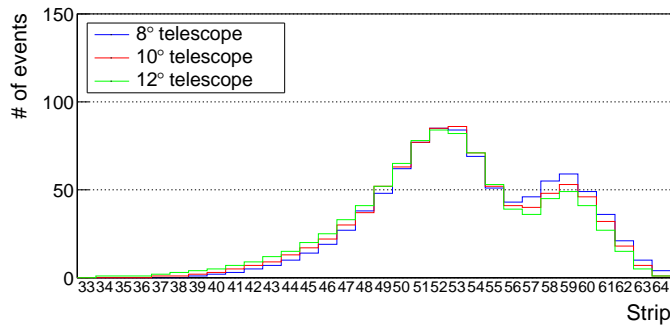


Figure 5.16: Effect of the variation of telescope inclination on the normalised geometrical acceptance distribution.

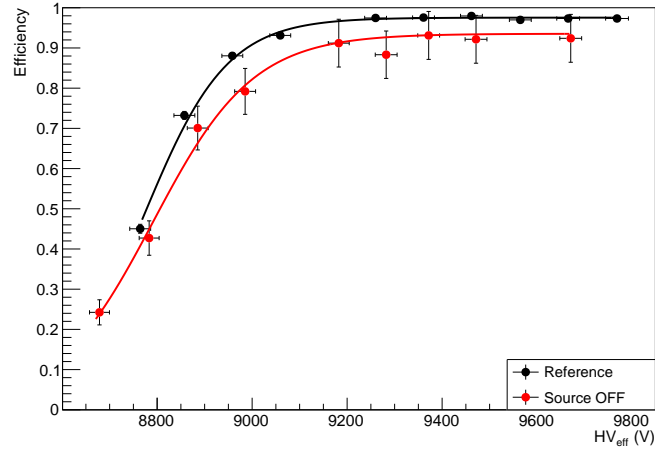


Figure 5.17: Correction of the efficiency without source. The efficiency after correction gets much closer to the Reference measurement performed before the study in GIF by reaching a plateau of $(93.52 \pm 2.64)\%$.

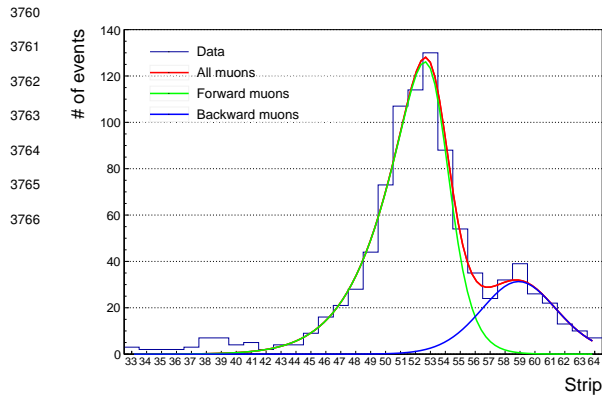


Figure 5.18: Hit distributions over read-out partition B of RE-4-2-BARC-161 chamber together with skew distribution fits corresponding to forward and backward coming muons.

Given the observed difference between the simulation and the measured data, one should realize that the geometrical acceptance and the hit profile are actually not directly comparable. The geometrical acceptance only provides with the information about what the detector can expect to see in a perfect world where all muons are detected in the exact same way. The detection would be independent from their energy or angle of incidence, and there would be no fluctuation of the detector gain due to complex avalanche development. No thresholds would be applied on the scintillators and on the RPC FEEs to reduce the noise, the cross-talk and the corresponding spread of the induced charge observed on the read-out strips. The hit profile provides the final product of all the previously mentioned contributions and can greatly differ from purely geometrical considerations. A full physics analysis involving softwares such as GEANT would be required to further refine the correction on the measured efficiency at GIF.

5.2.3 Photon flux at GIF

In order to understand and evaluate the γ flux in the GIF area, simulations have been conducted at the time GIF was opened for research purposes [264]. Table 5.2 gives the γ flux for different distances D to the source. The simulation was done using GEANT and a Monte Carlo N-Particle (MCNP) transport code, and the flux F is given with the estimated error from these packages expressed in %.

Nominal ABS	Photon flux F [$\text{cm}^{-2} \text{s}^{-1}$]			
	at $D = 50 \text{ cm}$	at $D = 155 \text{ cm}$	at $D = 300 \text{ cm}$	at $D = 400 \text{ cm}$
1	$0.12 \times 10^8 \pm 0.2\%$	$0.14 \times 10^7 \pm 0.5\%$	$0.45 \times 10^6 \pm 0.5\%$	$0.28 \times 10^6 \pm 0.5\%$
2	$0.68 \times 10^7 \pm 0.3\%$	$0.80 \times 10^6 \pm 0.8\%$	$0.25 \times 10^6 \pm 0.8\%$	$0.16 \times 10^6 \pm 0.6\%$
5	$0.31 \times 10^7 \pm 0.4\%$	$0.36 \times 10^6 \pm 1.2\%$	$0.11 \times 10^6 \pm 1.2\%$	$0.70 \times 10^5 \pm 0.9\%$

Table 5.2: Total photon flux ($E_\gamma \leq 662 \text{ keV}$) with statistical error predicted considering a ^{137}Cs activity of 740 GBq at different values of the distance D to the source along the x-axis of irradiation field [264].

This estimation of the backward versus forward content in the data was done through a fit using a sum of two skew distributions given in Equation 5.1. Although a skew distribution lacks physical interpretation, it allows fitting easily such kind of data, as showed in Figure 5.18.

$$(5.1) \quad \begin{aligned} g(x) &= A_g e^{-\frac{(x-\bar{x})^2}{2\sigma^2}} \\ s(x) &= \frac{A_s}{1 + e^{-\lambda(x-x_i)}} \\ sk(x) &= g(x) \times s(x) \\ &= A_{sk} \frac{e^{-\frac{(x-\bar{x})^2}{2\sigma^2}}}{1 + e^{-\lambda(x-x_i)}} \end{aligned}$$

3783 The table however does not
 3784 provide in a direct way the flux
 3785 at the level of the RPC under
 3786 test. First of all, it is nec-
 3787 essary to extract the value of
 3788 the flux from the available data
 3789 contained in the original paper
 3790 and then to estimate the flux in
 3791 2014 at the time the experimen-
 3792 tation took place. The extraction will be performed for the case of a pointlike source emitting
 3793 isotropic and homogeneous gamma radiations. The flux F_0 is known at a given reference point sit-
 3794 uated at D_0 from the source. The gamma flux F at a distance D from the source will be expressed
 3795 with Equation 5.2, assuming that the flux decreases as $1/D^2$ and where c is a fitting factor that can
 3796 be written as in Equation 5.3. Finally, using Equation 5.3 and the data of Table 5.2, with $D_0 =$
 3797 50 cm as reference point, Table 5.3 can be built. It is interesting to note that c for each value of D
 3798 does not depend on the absorption factor.

$$(5.2) \quad F^{ABS} = F_0^{ABS} \times \left(\frac{cD_0}{D} \right)^2$$

$$(5.3) \quad c = \frac{D}{D_0} \sqrt{\frac{F^{ABS}}{F_0^{ABS}}} \\ \Delta c = \frac{c}{2} \left(\frac{\Delta F^{ABS}}{F^{ABS}} + \frac{\Delta F_0^{ABS}}{F_0^{ABS}} \right)$$

3801 For the range of D/D_0 values available, it is possible to use a simple linear fit to get the evolution
 3802 of c that can be expressed as $c(D/D_0) = aD/D_0 + b$. Using Formula 5.4, but neglecting the
 3803 uncertainty on D that will only be used when extrapolating the values for the position of the RPC
 3804 under test whose position is not perfectly known, the results shown in Figure 5.19 is obtained.
 3805 Figure 5.19b confirms that using only a linear fit to extract c is enough as the evolution of the rate
 3806 that can be obtained superimposes well on the simulation points.

$$(5.4) \quad F^{ABS} = F_0^{ABS} \left(a + \frac{bD_0}{D} \right)^2, \quad \Delta F^{ABS} = F^{ABS} \left[\frac{\Delta F_0^{ABS}}{F_0^{ABS}} + 2 \frac{\Delta a + \Delta b \frac{D_0}{D} + \Delta D \frac{bD_0}{D^2}}{a + \frac{bD_0}{D}} \right]$$

3807 During the 2014 Gif tests, the RPC read-out plane was located at a distance $D = 206$ cm from
 3808 the source. Moreover, to estimate the strength of the flux in 2014, it is necessary to consider the
 3809 nuclear decay through time of the Cesium source whose half-life is well known ($t_{1/2} = (30.05 \pm$
 3810 0.08) y). The very first source activity measurement has been done on the 5th of March 1997 while
 3811 the Gif tests were done in between the 20th and the 31th of August 2014, i.e. at a time $t =$
 3812 (17.47 ± 0.02) y resulting in an attenuation of the activity from 740 GBq in 1997 to 494 GBq in
 3813 2014. All the needed information to extrapolate the expected flux through the detector at the moment
 3814 of the Gif preliminary tests has now been assembled, leading to Table 5.4. By assuming an average
 3815 sensitivity of the RPC to γ emitted by the ^{137}Cs source of $(2 \pm 0.2) \times 10^{-3}$ [271], the order of
 3816 magnitude of the expected hit rate per unit area would be of the order of kHz for a fully opened
 3817 source, as reported in the last column of the table. As photons are not charged particles, they mainly

³⁸¹⁸ interact with the electrodes where they are converted into electrons. The HPL electrodes are not very
³⁸¹⁹ sensitive to gamma photons, hence only a small fraction of the incoming flux is seen by the RPC.

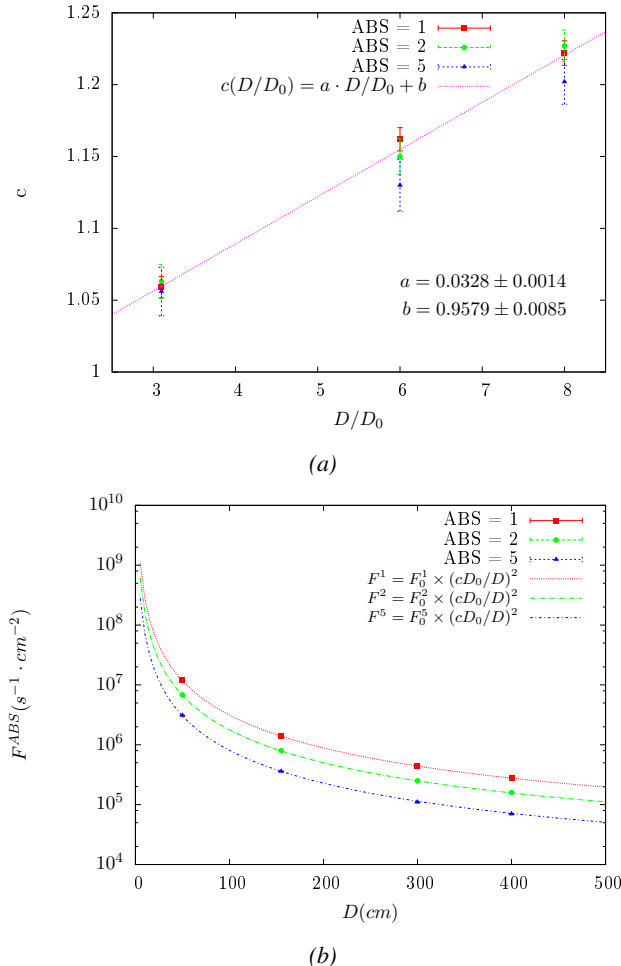


Figure 5.19: (a) Linear approximation fit performed on the data extracted from table 5.3. (b) Comparison of Equation 5.4 with the simulated flux using a and b given in figure 5.19a in Equation 5.2 and the reference $D_0 = 50$ cm and the associated flux for each absorption factor F_0^{ABS} from table 5.2.

Nominal ABS	Photon flux F [$cm^{-2} s^{-1}$]			Rate [Hz/cm ²] at $D^{2014} = 206$ cm
	at $D_0^{97} = 50$ cm	at $D^{97} = 206$ cm	at $D^{2014} = 206$ cm	
1	$0.12 \times 10^8 \pm 0.2\%$	$0.84 \times 10^6 \pm 1.2\%$	$0.56 \times 10^6 \pm 1.2\%$	1129 ± 14
2	$0.68 \times 10^7 \pm 0.3\%$	$0.48 \times 10^6 \pm 1.2\%$	$0.32 \times 10^6 \pm 1.2\%$	640 ± 8
5	$0.31 \times 10^7 \pm 0.4\%$	$0.22 \times 10^6 \pm 1.2\%$	$0.15 \times 10^6 \pm 1.2\%$	292 ± 4

Table 5.4: The data at D_0 in 1997 is taken from [264]. Using Formula 5.4, the flux at D , including an error of 1 cm, can be estimated in 1997. Then, taking into account the attenuation of the source activity, the flux at D can be estimated at the time of the tests in GIF in 2014. Assuming a sensitivity of the RPC to gammas, $s = (2 \pm 0.2) \times 10^{-3}$ [271], an estimation of the hit rate per unit area is obtained.

3820 The goal of the study was to have a good measurement of the intrinsic RPC performance without
 3821 source irradiation. Then, taking profit of the two working absorbers, at absorption factors 5 (300 Hz)
 3822 and 2 (~ 600 Hz) the goal was to show that the detectors fulfill the performance certification of CMS
 3823 RPCs. Finally, a first assessment of the performance of the detectors at higher backgrounds was
 3824 obtained with absorption factor 1 (no absorption and >1 kHz)).

3825 5.2.4 Results and discussions

3826 The data taking at GIF has been conducted between the 21st and the 31st of August, 2014. Data
 3827 have been collected with source both ON and OFF using three different absorber settings (ABS 5, 2
 3828 and 1) in order to vary the irradiation on the RPC. For each source setting, two HV scans have been
 3829 performed with two different trigger settings. During a first scan the trigger sent to the TDC module
 3830 was the coincidence of the two scintillators composing the telescope while during a second scan
 3831 the trigger was a pulse coming from a pulse generator in order to measure the noise or gamma rate
 3832 seen by the chamber. Indeed, using a pulse generator allows to trigger at moments not linked to any
 3833 physical event and, hence, to obtain a *RANDOM* trigger on noise and gamma events to measure the
 3834 associated rates, the probability to have a pulse in coincidence with a cosmic muon being negligible.

3835 From the cosmic trigger scans, a summary of the efficiencies and corresponding cluster sizes
 3836 is shown in Figure 5.20. The efficiency curves with Source ON show a shift with respect to the
 3837 case without irradiation. With ABS 5, the general shape of the efficiency curve stays unchanged
 3838 whereas a clear alteration of the performance is observed at ABS 2 and ABS 1. From the cluster
 3839 size results, a reduction of the mean cluster size under irradiation can be observed at equivalent
 3840 efficiency. This effect can be due to the perturbation of the electric field by the strong flux of gamma
 3841 particles interacting with the electrodes. With the increasing number of photons being converted
 3842 into electrons, an increasing number of charges need to be recombined all over the volume of the
 3843 electrodes that act as capacitors. A discharge of the electrodes reduces the effective field seen in the
 3844 gas volume by introducing a voltage drop across the electrodes thickness. The constant pressure put
 3845 on the detector by the converting photons can become strong enough to uniformly affect the gain of
 3846 the detector.

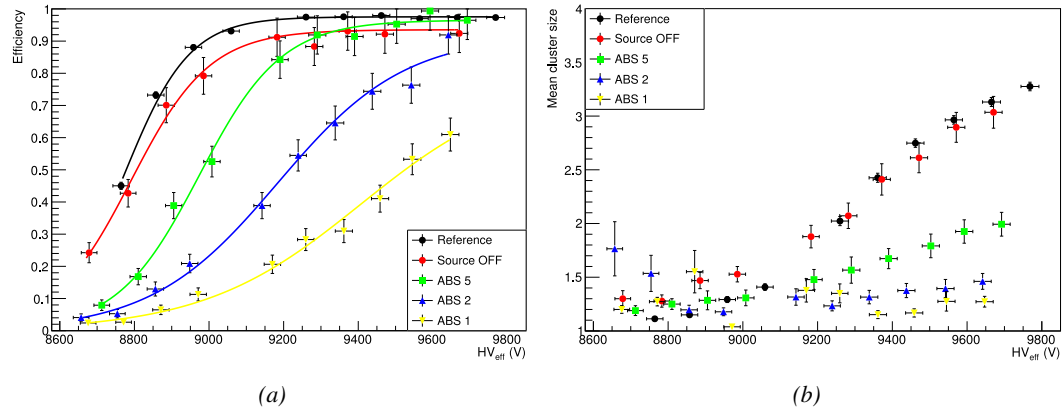


Figure 5.20: Efficiency (a) and cluster size (b) of chamber RE-4-2-BARC-161 measured at GIF with Source OFF (red) and Source ON using different absorber settings: ABS 5 (green), ABS 2 (blue) and ABS 1 (yellow). The results are compared to the Reference values obtained with cosmics.

3847 It is necessary to study the evolution of the performance of the chamber with the increasing rate
 3848 per unit area. The hit rate is measured as the number of hits detected in the RPC normalized to the
 3849 surface area of the read-out and to the total integrated time. The integrated time is linked to the time
 3850 window in which the TDC searches for data related to a trigger signal. Data is continuously kept in
 3851 the buffer of the TDCs but not all of these data is of interest. When a trigger signal is sent to the TDC
 3852 module, the TDC saves all of the data located in a certain time window set around the time stamp of
 3853 the signal. The total integrated time is then the total number of trigger signals times the width of a
 3854 search time window.

3855 In Figure 5.21a, the noise rate when the source is OFF remains low but increases at voltages above
 3856 9500 V. Aside of the natural increase of the noise with increasing voltage, the rise of the noise rate
 3857 in the detector can be related to the increased streamer probability observed with such a large electric
 3858 field. The rates measured at GIF with source ON all show a similar behaviour until a high voltage
 3859 of approximately 9400 V at which the rate of ABS 5 reaches a plateau, coinciding with the chamber
 3860 reaching full efficiency. It is important to note that, even though the rates look similar independently
 3861 from the gamma flux, relative to the efficiency of the chamber, the rate actually increases with
 3862 increasing flux at equivalent efficiency. A rough way to measure the rate effectively observed by
 3863 the detector for each source setting would be to normalize the measured rates to the efficiency of
 3864 the detector. This exercise was done with Figure 5.21b from which constant fits where done on
 3865 Source ON data in order to extract the rate the chamber was subjected to. This method leads to
 3866 rates of (164 ± 12) Hz/cm², (340 ± 26) Hz/cm² and (598 ± 50) Hz/cm² respectively for ABS
 3867 5, 2 and 1 which is consistent with the absorber values. Also, contrary to the case of the source
 3868 OFF measurement, no rise of the noise is observed at ABS 5. This difference could be explained
 3869 by the efficiency shift that is related to a decrease of the electric field across the gas volume. **[But,**
 3870 **as no data were taken at higher voltage values, this assumption can't be confirmed.] Could be**
 3871 **confirmed by a study of the streamer probability for each dataset.**

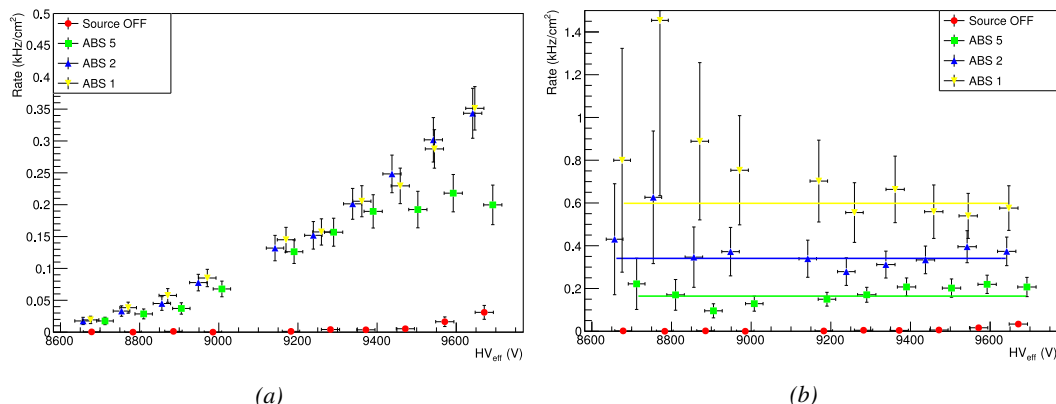


Figure 5.21: Rates in chamber RE-4-2-BARC-161 measured at GIF with Source OFF (red) and Source ON using different absorber settings: ABS 5 (green), ABS 2 (blue) and ABS 1 (yellow). On Figure (b), the rates of Figure (a) were normalized to the measured efficiency, and constant fits are performed on Source ON data showing the gamma rate in the chamber.

3872 The results need to be taken with care as a better estimation of the rate would have been to push
 3873 the detector towards higher voltages to reach the efficiency plateau for each absorber configuration
 3874 and only then extract the measured rate at working voltage, defined as in Formula 3.25. Nevertheless,

3875 using this method to estimate the rate to which the chamber is subjected, it is possible to look at the
 3876 evolution of the HV_{50} and HV_{knee} as a function of the increasing rate as showed in Figure 5.22.
 3877 The results from GIF suggest that at a rate of 600 Hz/cm^2 the working voltage of the chamber is
 3878 increased by a thousand V while the efficiency is reduced to approximately 80%, although the result
 3879 still is consistent with an efficiency better than 90% due to the large error on the measurement.

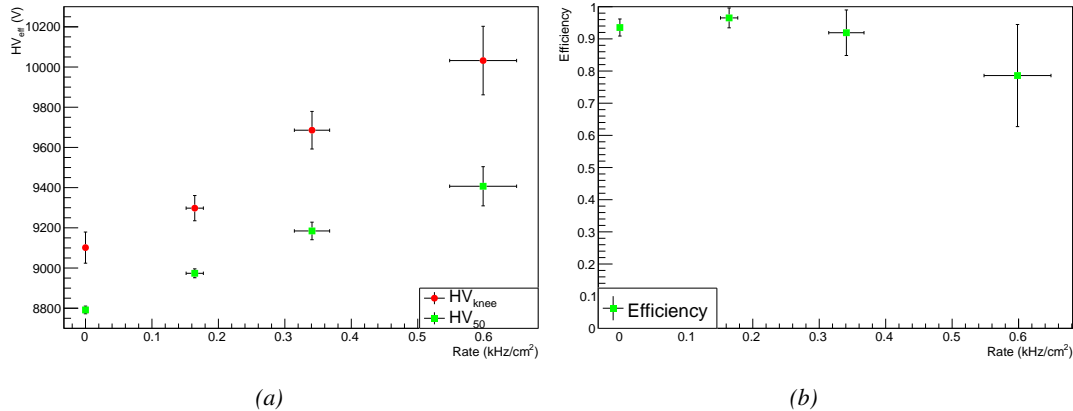


Figure 5.22: Evolution of the voltages at half maximum and at 95% of the maximum efficiency (Figure 5.22a), and of the maximum efficiency (Figure 5.22b) as a function of the rate in chamber RE-4-2-BARC-161. The data is extracted from the fits in Figures 5.20a and 5.21b.

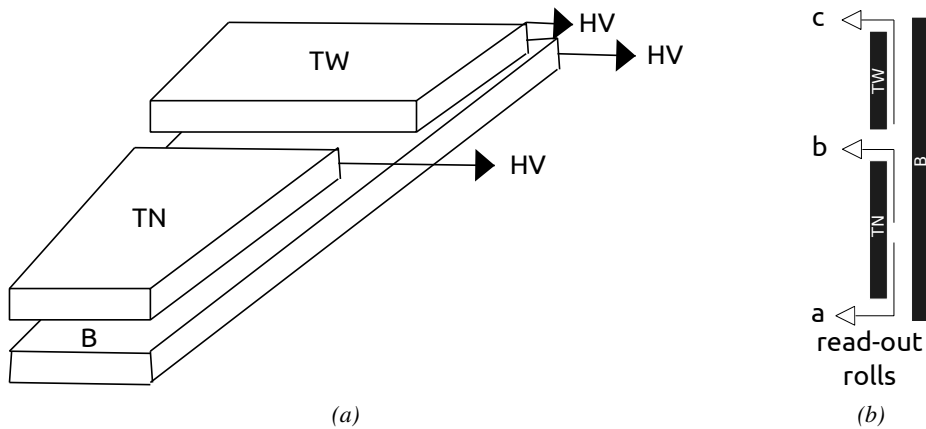


Figure 5.23: Presentation of a double-gap endcap RPC with its three RPC gaps. Due to the partitioning of the read-out strips into three rolls, the TOP layer of gap is divided into two gaps: TOP NARROW (TN) and TOP WIDE (TW). The BOTTOM (B) only consists in one gap.

3880 It is likely that the rates obtained through fitting on normalized values is underestimated. Indeed,
 3881 monitoring the current in the three gaps composing a CMS endcap RPC (Figure 5.23) while knowing
 3882 the rate, the charge deposition per avalanche q_γ can be computed. A current density, expressed in
 3883 A/cm^2 , divided by a rate per unit area, expressed in Hz/cm^2 yields a charge expressed in C. The
 3884 current driven by the RPC is assumed to be due to the irradiation, hence, to the avalanches developing

in the gas volume due to the photons of the Cesium source. On the other hand, the rate is supposed to be a measure of the number of photons interacting with the detector. This way, it comes that the charge deposition per avalanche is expressed like $q_\gamma = J_{mon}/R_\gamma$, with J_{mon} being the monitored current density and R_γ the measured γ rate. The current density is computed as the sum of the current density measured in the top and bottom gap layers, $J_{mon} = (I_{mon}^{TW} + I_{mon}^{TN})/(A_{TW} + A_{TN}) + I_{mon}^B/A_B$, with $A_{B,TN,TW}$ being the active area and $I_{mon}^{B,TN,TW}$ the monitored currents of the gaps. According to Figure 5.24, the charge deposition per avalanche consistently converges to a value of the order of 50 pC for each absorber setting which corresponds to a value more than twice larger than what reported in literature for CMS detectors [271, 272] indicating that the rates could have been wrongly evaluated during the short study performed at GIF. An increase of the γ rate by a factor 2 would actually be consistent with the expected rates calculated in Table 5.4, assuming the sensitivity to γ to be of the order of $(2 \pm 0.2) \times 10^{-3}$.

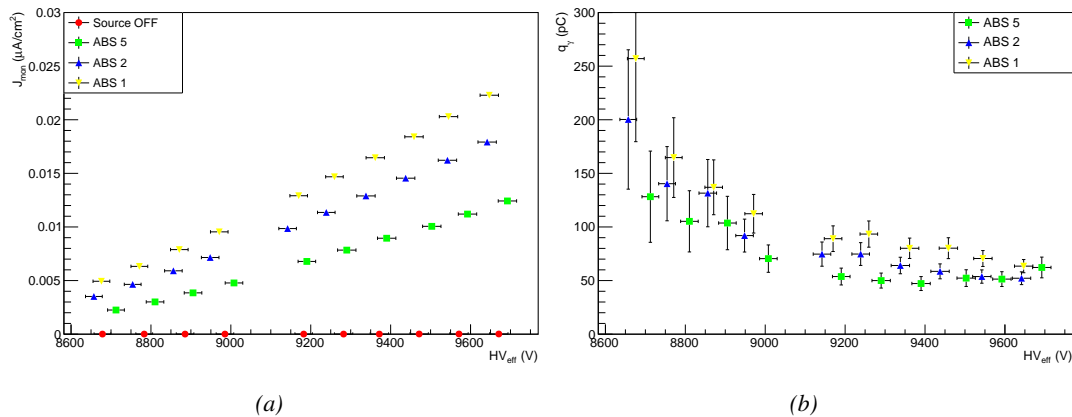


Figure 5.24: Current density (a) and charge deposition per gamma avalanche (a), defined as the current density normalized to the measured rate taken from Figure 5.21a as a function of the effective high voltage in chamber RE-4-2-BARC-161 measured at GIF with Source ON using different absorber settings: ABS 5 (green), ABS 2 (blue) and ABS 1 (yellow).

Overall, working at GIF has been a rewarding experience as it offered CMS RPC R&D team the possibility to start developing the necessary skills and tools that would become the core of GIF++ experiment. The quality of the results can be argued both due to the little robustness of the experimental setup and the lack of available statistics to draw conclusions from, bringing large errors on the final result. The confrontation of the data to known results pointed to a failure in correctly measuring the γ rate at working voltage and, hence, to an overestimation of the charge per avalanche and of the drift of working voltage with increasing rate. Nevertheless, the prototypes of DAQ and offline analysis tools proved to be reliable.

5.3 Longevity tests at GIF++

5.3.1 Selection and characterization of CMS RPCs for longevity at GIF++

In the perspective of future upgrades of LHC that would bring detectors to be operated in a high irradiation environment, the new Gamma Irradiation Facility of CERN was first proposed in 2009 [273].

3909 The Gif++ would thus provide all LHC R&D teams working on behalf of the different LHC exper-
 3910 iment with a facility to perform longevity studies using a very intense Cesium gamma source.

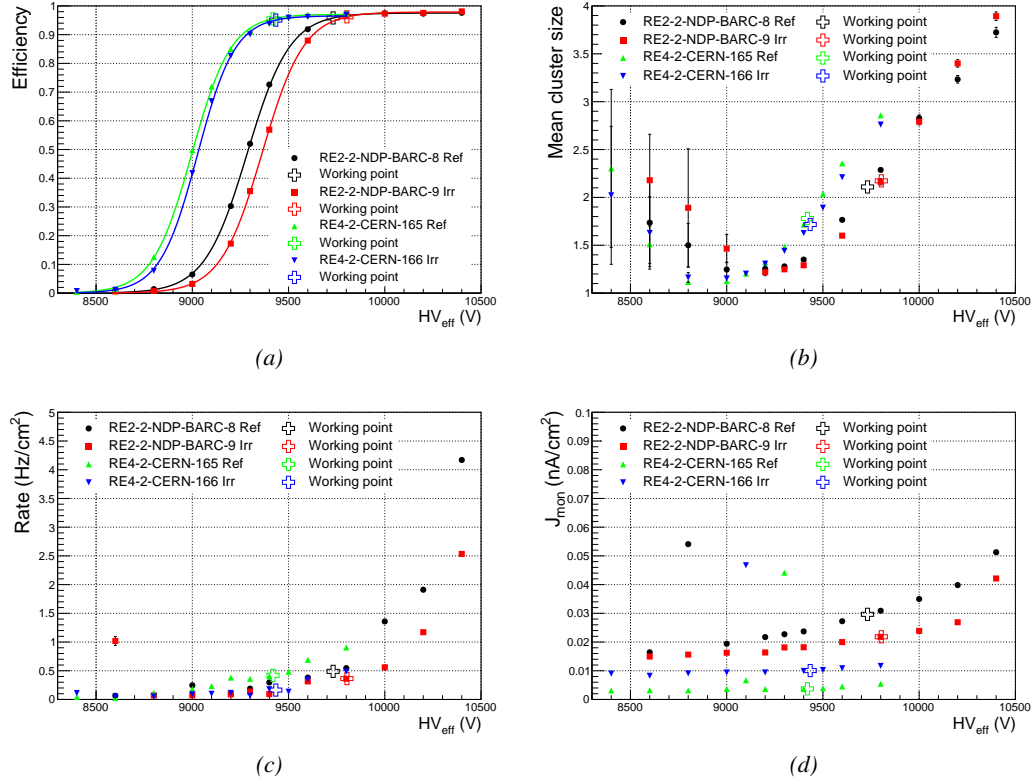


Figure 5.25: Characterization of CMS RPC detectors foreseen to be used at Gif++ for longevity studies of the present system. Using cosmic muons, efficiency (a) and cluster size (b) were measured as well as noise rate (c) and current density (d). For each detector, the working voltage, defined as in Formula 3.25 after LS1, was extracted from sigmoid fits performed in Figure (a) and the values of efficiency, cluster size, noise rate and current density at this voltage are reported using open crosses.

3911 In the specific case of CMS RPC, the longevity studies imply a constant irradiation of selected
 3912 detectors in order to accumulate a charge equivalent to what is expected during HL-LHC, i.e. a
 3913 charge of $0.8 \text{ C}/\text{cm}^2$ according to Figure 5.2 including a safety factor 3. Other detectors are left
 3914 non-irradiated to be used as references. Throughout the irradiation campaign, the performance of
 3915 the irradiated and reference detectors will be periodically probed using the high intensity H4 muon
 3916 beam. Dedicated test beam periods will be used to measure the efficiency and gamma rate at the
 3917 level of the detectors. Different source absorber settings will test the rate capability of CMS RPCs,
 3918 that needs to be certified above $600 \text{ Hz}/\text{cm}^2$. Using a muon beam will also help identifying signs of
 3919 ageing in the case the performance of the irradiated detectors diverges from those of the reference
 3920 detectors with increasing accumulated charge. Other than the performance of the detectors, signs of
 3921 ageing could come from increasing dark current that would be related to local ageing of the elec-
 3922 trodes triggered by the increased hydrofluoric acid (HF) production in an irradiated environment.
 3923 HF is produced by the decomposition of $C_2H_2F_4$ molecules during the charge multiplication pro-

cess and leads to increased dark current and noise in Bakelite RPCs treated with linseed oil. This effect is strongly reinforced by the presence of UV photons [274, 275]. A close monitoring of the current driven by the detectors will then be necessary as well as dedicated periodical electrode resistivity measurements and chromatography analyses on the gas exhaust.

As the maximum background in CMS is found in the endcap disks, the choice was made to focus the GIF++ longevity studies on endcap chambers. Most of the RPC system was installed in 2007. Nevertheless, the large chambers in the fourth endcap (RE4/2 and RE4/3) have been installed during LS1 in 2014. The HPL of these two different productions possibly having slightly different properties, four spare chambers of the present system were selected. From the original CMS RPC system, two RE2/2 spares were selected along two RE4/2 spares from the newest detectors. Having two chambers of each type allowed to always keep one of them non-irradiated as reference. Due to the limited gas flow in GIF++, the RE4 chamber remained non-irradiated until end of November 2016 when the longevity studies could finally be started on those chambers.

The performance of the chambers prior to the start of the longevity campaign was characterized in Ghent before their transportation to CERN for installation in the GIF++. The results of the characterization are showed in Figure 5.25 and summarized in Table 5.5. A clear difference in performance for both types of chambers is observed as the working voltages of the newest chambers, of type RE4, are 300 to 400 V lower to the older chambers indicating that the gap thickness of RE4 detectors could be thinner. This conclusion could as well be supported by the lower cluster size at working voltages that are also smaller in RE4 chambers. Even though the measured currents are low, RE4 detectors draw less current without irradiation than RE2 detectors pointing to a difference in electrode resistivity that were produced at different moments. Efficiency and noise rate levels are of the same order of magnitude for both type of RPCs.

RPC	RE2-2-BARC-08	RE2-2-BARC-09	RE4-2-CERN-165	RE4-2-CERN-166
Used as	Reference	Irradiation	Reference	Irradiation
HV_{WP} (V)	9732 ± 6	9803 ± 6	9419 ± 5	9434 ± 5
Efficiency at WP	96.2 ± 0.3	96.6 ± 0.3	95.9 ± 0.3	95.5 ± 0.3
Cluster size at WP	2.19 ± 0.04	2.27 ± 0.05	1.88 ± 0.04	1.80 ± 0.04
Noise at WP (Hz/cm ²)	0.51 ± 0.01	0.39 ± 0.01	0.44 ± 0.00	0.15 ± 0.01
J^{WP} (pA/cm ²)	30.1 ± 0.1	22.2 ± 0.1	3.8 ± 0.0	10.2 ± 0.0

Table 5.5: Summary of the characterization measurement performed in Ghent on CMS RPC detectors foreseen to be used at GIF++ for longevity studies of the present system. For each detector, the working voltage, defined as in Formula 3.25, was extracted from sigmoid fits performed in Figure 5.25a. The values of efficiency, cluster size, noise rate and current density at this voltage are reported.

5.3.2 RPC test setup

For an easy manipulation of the detectors, a trolley with a structure containing slots in which the RPCs can be slid vertically was used and is referred to as T1. When in position, each chamber is in a plane perpendicular to the beam line and the source flux as can be seen through Figure 5.26, and receives a uniform irradiation. Moreover the trolley allows for easy movement of the system. Indeed, the position of the trolley varies according to the specific measurements that are being done.

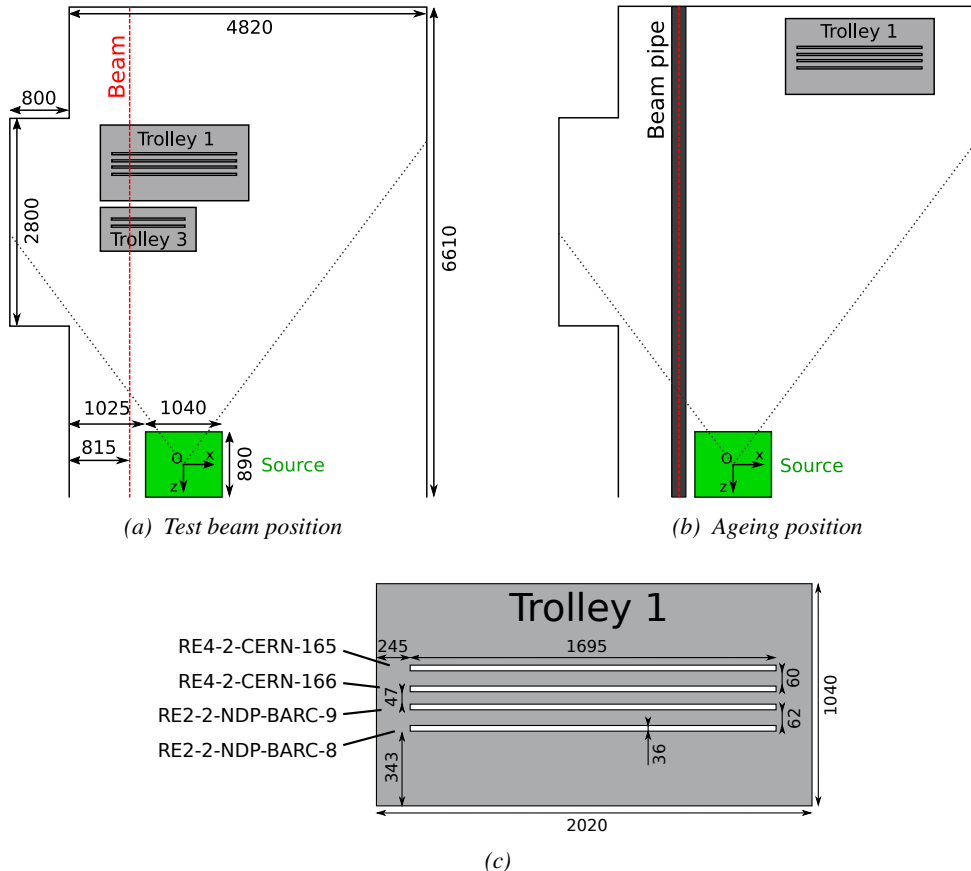


Figure 5.26: CMS RPC setup inside the GIF++ bunker during test beam (a) and ageing periods (b). The space in between the RPCs and the source is usually used by other detectors while the space in between T1 and the upstream wall is not filled. Due to the presence of the beam pipe, the trolley is moved away from the beam line during irradiation periods and placed further away from the source for less intense irradiation. The position of the trolley can vary due to the use of the space by other setups and is then not exact. Nonetheless, the position of the chambers in the trolley is fixed and given in Figure (c).

During the dedicated test beam periods, the GIF++ experiments are in control of the muon beam. The trolley is placed in the upstream region of the bunker, in the beam line at a distance of generally 3.4 m from the source, as described through Figure 5.26a. At this distance, the simulated gamma current is the order of $5 \times 10^6 \text{ cm}^{-2} \text{ s}^{-1}$. The CMS RPC detectors are the furthest away from the source as other detectors need to be certified at higher background rates. Depending on the needs of the other experiments at the GIF++, the trolley position of the trolley can be pushed as far as 4.1 m from the source. An additional trolley, referred to as T3, contains iRPCs and is placed between the source and the T1 trolley. Indeed, iRPCs need to be certified at higher rates and thus need to be placed closer to the source to receive a stronger irradiation using the same absorber settings. The space on T1 being limited, the tracking RPCs used for extra offline information during the analysis are placed on the same trolley as the iRPCs. They are kept at full efficiency at all time to reconstruct muon tracks and to correlate them with hits recorded in T1 chambers. The beam trigger system is composed of three scintillators. Two are placed outside on each side of the bunker and of the third scintillator is placed in the beam line in between T1 and the wall.

3967 Most of the year, outside of these test beam periods, T1 is placed in the so called *ageing position*
 3968 corresponding to the furthest position at approximately 4.7 m from the source outside of the beam
 3969 line before August 2019. At such a distance, the simulated gamma current is the order of 3×10^6
 3970 $\text{cm}^{-2} \text{s}^{-1}$. Following the extension of the upstream area in August 2019, the trolley was pushed
 3971 approximately 1 m away at a distance of 5.7 m to the source, corresponding to a simulated gamma
 3972 current of the order of $2 \times 10^6 \text{ cm}^{-2} \text{s}^{-1}$. During periods where GIF++ doesn't have the control of
 3973 the beam, the beam line needs to stay clear so that a beam tube can be installed through the bunker,
 3974 as can be seen in Figure 5.26b. The reason for placing the chambers as far as possible from the
 3975 source comes from the too high irradiation delivered by the source during the irradiation periods
 3976 where all the other groups having placed detectors in the bunker require as much charge integration
 3977 as possible. Hence, the source is operated without any absorbers. On the contrary, during the test
 3978 beam periods, all the groups working in GIF++ are interested in operating the source using various
 3979 absorber settings to study the performance of their detectors under different irradiation conditions.
 3980 T1 RPCs are kept at a stanby voltage of 6500 V when the other groups need to work with ABS 1
 3981 due to the proximity of the trolley to the source compared to ageing periods.

3982 From the bunker area, long cables and pipes running through the wooden floor connect the de-
 3983 tectors to the service area, visible in Figure 5.6. The service area hosts all the high and low voltage
 3984 power supplies, the TDCs and computers used for data acquisition and preliminary offline analysis.
 3985 The gas system required for the gaseous detectors installed in GIF++ can also be found in the service
 3986 area [276].

3987 The detectors read-out is, as in the case of GIF, connected to V1190A VME TDCs communicating
 3988 with the DAQ computer via a V1718 VME bridge manufactured by CAEN. At the end of each data
 3989 tacking, the preliminary analysis is run to fill the Detector Control Software webpage, referred to as
 3990 WebDCS, with Data Quality Monitoring (DQM) histograms. The WebDCS is a custom made DCS
 3991 application for the specific case of GIF++ RPCs. It provides online information about the environ-
 3992 mental parameters in the bunker as well as the state of each detector. A constant monitoring of
 3993 all the environmental parameters, in different points of the bunker area, gas parameters, to control its
 3994 composition, temperature and pressure, and of the voltages and currents delivered by the power sup-
 3995 plies is performed and displayed on the homepage of the WebDCS interface. Moreover, it contains
 3996 the database with all the RPC data in the form of ROOT files and of summary hisograms. Hence, it
 3997 is a useful tool for the shifters on duty in the control room located farther in the building, away from
 3998 the beam lines.

3999 5.3.3 GIF++ data flow

4000 At GIF++, the CMS RPC R&D setup collects different types of data from the detector monitoring
 4001 parameters, such as voltage and currents, the gas, source, and environmental parameters, and, of
 4002 course, the TDC data related to the actual muon and gamma measurements. These different data
 4003 sources correspond to three different data flows as presented in Figure 5.27.

4004 The *Data Interchange Protocol (DIP)* flow, DIP being a communication system allowing for
 4005 exchange of real-time information between systems [277], concerns all the data coming from the
 4006 gas composition, temperature and humidity, the environmental temperature and pressure, the source
 4007 settings and the radiation monitoring sensors. At the experimental area, all data of interest for all of
 4008 the users of the facility (source settings, radiation monitoring, gas composition at the exit of the gas
 4009 mixer and general environmental information) are measured, distributed and also stored in the data
 4010 of the experimental hall where is located the GIF++. Access to the database is done through DIP

4011 communication. The measurement of more specific data such as gas flow, temperature and humidity
 4012 at the level of the detectors (upstream and downstream of the detectors) as well as environmental
 4013 parameters has to be arranged by the users themselves. For this reason, several pressure, tempera-
 4014 ture and humidity sensors were installed on the gas distribution system of the RPC trolleys. The
 4015 corresponding data flow, although not related to DIP itself, is saved together with the DIP data into
 4016 the local CMS RPC database and displayed on the front page of the WebDCS. In the case any of
 4017 the measured values go out of their optimal range, the WebDCS will produce corresponding alerts.
 4018 The data are particularly important to perform the PT correction described in Section 3.4 of Chap-
 4019 ter 3 and to stabilize the effective voltage of the detectors. Monitoring history plots are made using
 4020 JavaScript are also displayed for easy access to past information, as shown in Figure 5.28.

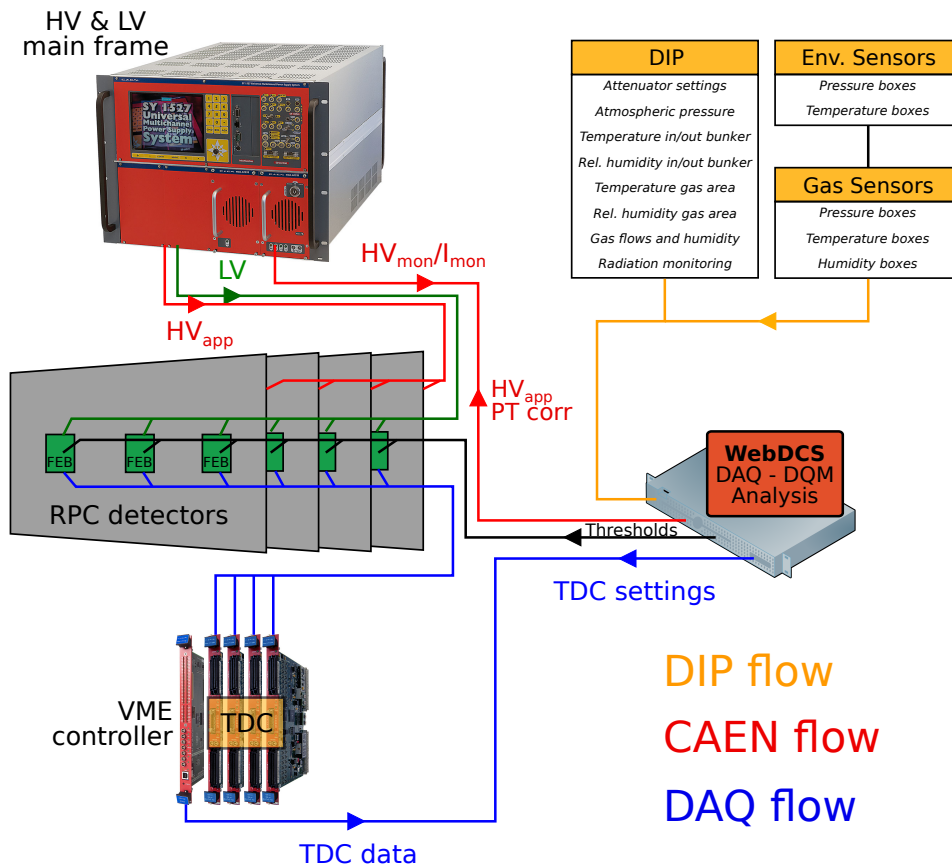


Figure 5.27: Visualisation of the main data flows in the CMS RPC setup at the Gif++. The yellow flow lines correspond to the DIP flow used for source, environmental and gas information. The red flow lines are for the CAEN flow through which the WebDCS communicates the voltages to be applied on the detectors using pressure and temperature information and retrieves the monitored voltages and currents. Finally, the blue flow lines correspond to the DAQ flow through which the RPC data is collected from the TDCs by the computer.

4021 The data flow related to the monitoring of the detector high voltages and currents, referred to
 4022 as *CAEN flow* as a reference to the manufacturer of power supplies, is handled through direct com-
 4023 munication between the DAQ computer and the power supply main frames. Finally, the DAQ flow
 4024 concerns all data acquired through the use of the TDCs, i.e. all the muon or gamma event data

4025 recorded by the detectors under test at GIF++. It was already discussed that when a trigger signal is
 4026 sent to a TDC module, the TDC saves all of the data located in a certain time window set around the
 4027 time stamp of the signal. The trigger signal in the case of GIF++ can be a coincidence of the trigger
 4028 scintillators or a signal from a pulse generator. The DAQ computer extracts from the TDC buffers the
 4029 list of fired channels and of associated time stamps for each trigger signal. The data is then used to
 4030 reconstruct muon tracks along the CMS RPC setup at the GIF++ or to compute the noise and gamma
 4031 rates associated to a certain source setting.

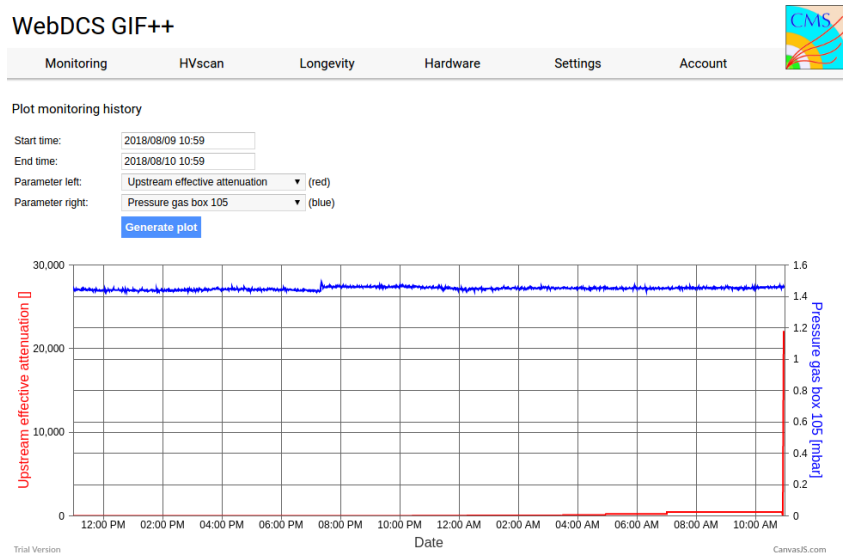


Figure 5.28: DIP monitoring history accessed through the GIF++ WebDCS interface.

4032 5.3.4 Measurements performed during beam periods

4033 As previously described, two types of measurements are performed on the chambers during beam
 4034 periods. On the one hand, it is interesting to measure the efficiency of the RPCs with increasing
 4035 voltage with different source absorber settings but on the other hand, it is important to correlate the
 4036 efficiency information to the gamma rate seen by the chambers at the different voltages. The choice
 4037 was made to separate efficiency measurements from rate measurements to better manage time and
 4038 data volume. In both cases, TDC data recorded during so called *HV scans* is divided into *runs*, one
 4039 for each high voltage point, whose data is stored into ROOT files. The TDC settings used during
 4040 both these scans as well as the ROOT data structure are detailed in Section A.4.2 of Appendix A.

4041 The goal of both efficiency and rate scans is to measure the rate capability of the detectors but
 4042 also to monitor any degradation of the performance due to ageing. This way, during test beam
 4043 periods the efficiency and corresponding gamma background are measured to correlate the evolution
 4044 of rate capability at different stages of irradiation. In the absence of other signs of ageing, a reduction
 4045 of the rate capability could be related to an increase of the electrodes resistivity.

5.3.4.1 Efficiency scans

The HV scans performed to specifically measure the muon detection efficiency under different irradiation conditions follow a standardized procedure. Data using the DAQ is taken at the same 12 HV points for all chambers, ranging from 9 kV to 10.1 kV in steps of 100 V. For each HV run, a minimum of 5000 muon beam triggers, provided by the coincidence of the three scintillators, is required in order to accumulate enough statistics for a reliable computation of the efficiency of the detectors. In addition to the four RPCs held on T1, two tracking RPCs installed on T3 are kept at a fixed voltage of 9.7 kV to provide the analysis software [278] with beam position information to exclude off-track signals. The tracking RPCs are double gap detectors featuring 2 mm HPL electrodes and 2 mm gas gaps. They are prototypes built by the italian company *General Tecnica* using a different production of HPL. Finally, the monitored currents and voltages are recorded in histograms along with the TDC data in a different ROOT file for each run.

HV scans are taken for different source settings as the goal is to irradiate all the detectors with a minimal rate of 600 Hz/cm². Usually, a full study of the performance of the detectors is performed with Source OFF, and then with nine absorber settings that attenuate the nominal gamma flux by factors from more than 200 to only 3, where settings with fully opened source are avoided with RPCs in test beam position. During the efficiency scans, the cluster size is also measured and the currents are monitored as can be seen in Figure 5.29.

5.3.4.2 Rate scans

The background measurements are performed using a similar HV scan procedure as for the efficiency measurements. The HV scan in test beam periods is taken at fewer HV points compared to the efficiency scans as the region of interest is located around the knee and efficiency plateau of the detectors, i.e. these scans are performed only on six HV points ranging from 9.5 kV to 10 kV. The value of the rate at the operating voltage is then deduced from the efficiency scan through linear

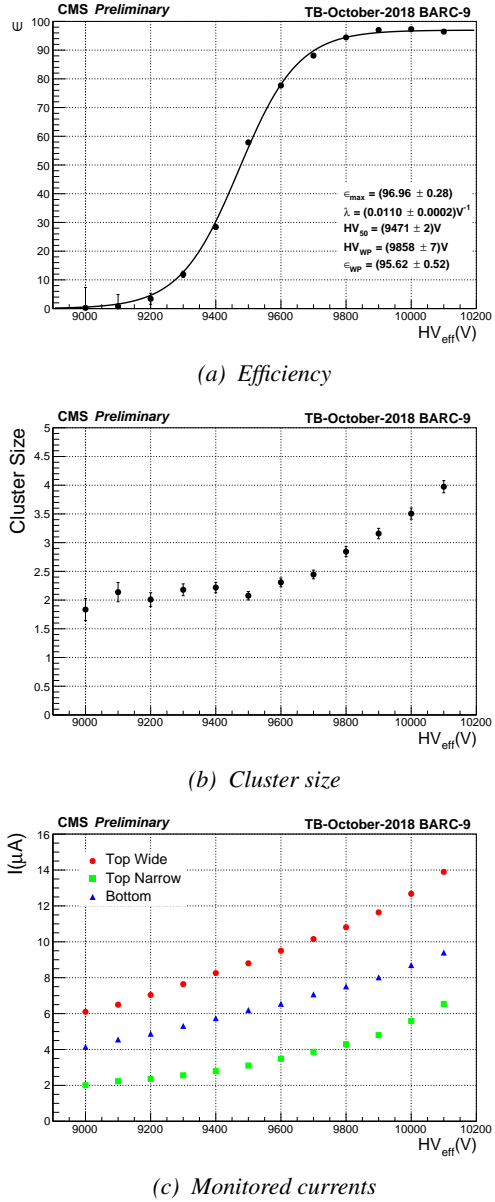


Figure 5.29: Example of results obtained during an efficiency scan performed with ABS 113 (4.6) during October 2018 testbeam period.

4090 interpolation. A good estimation of the rate requires a long enough integrated time of the TDC data.
 4091 The way data is collected, detailed in Appendix A, makes the DAQ search for data stored in the TDC
 4092 buffers prior to the trigger signal. The time window from which the data can be collected ranges from
 4093 25 ns to more than 50 μ s. With the Cesium source delivering a constant gamma flux, it was decided
 4094 that a total integrated time of 0.2 s would be enough to have a reliable calculation of the gamma
 4095 rate. This is achieved by taking 20,000 random trigger pulses delivered by a pulse generator at a
 4096 frequency of 300 Hz while extracting 10 μ s of data from the buffers for each trigger. An example
 4097 of the data obtained during rate scans is showed in Figure 5.30 in which the hit multiplicity at a
 4098 single HV step of a scan, used to compute the rate per unit area, is showed together with the rates as
 4099 computed at every HV steps.

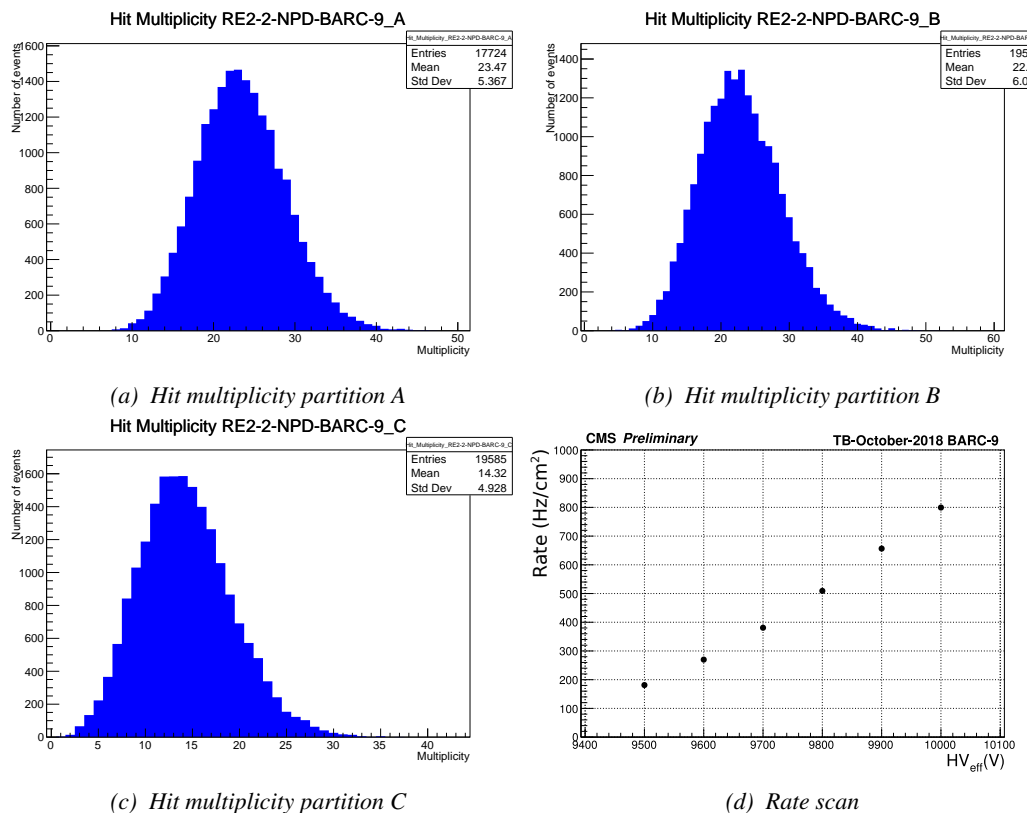


Figure 5.30: Example of results obtained during an efficiency scan performed with ABS 113 (4.6) during October 2018 testbeam period. The hit multiplicity histograms (a), (b) and (c) correspond to the fourth HV point of the scan at 9800 V.

4100 Separating the rate and efficiency measurements was motivated by the inconsistency of the muon
 4101 beam provided in Gif++². Using periods without beam to measure rates with a good statistics allows
 4102 for faster study programs. Moreover, the number of muons per beam spill depends strongly on the
 4103 user setups placed upstream of the Gif++ and on the specific beam optic magnet settings. Collecting

²During test beam periods, the delivery of the muon beam at the SPS North Area depends on the LHC program. As the SPS is used to feed the LHC with accelerated protons, the priority is given to the LHC. Other than the LHC, the delivery of muon beams can also be stopped due to maintenance or breakdown on the acceleration lane. This may translate into long periods with low intensity beams or even without any beam at all.

4104 20,000 events could then take too long for the other users at the Gif++. Hence, efficiency scans are
 4105 performed with lower statistics, and the time window from which the TDC data are extracted is
 4106 strongly reduced (400ns for efficiency scans versus 10 μ s for rate scans) to keep the data size to its
 4107 bare minimum.

4108 **5.3.4.3 Offline analysis and Data Quality Monitoring**

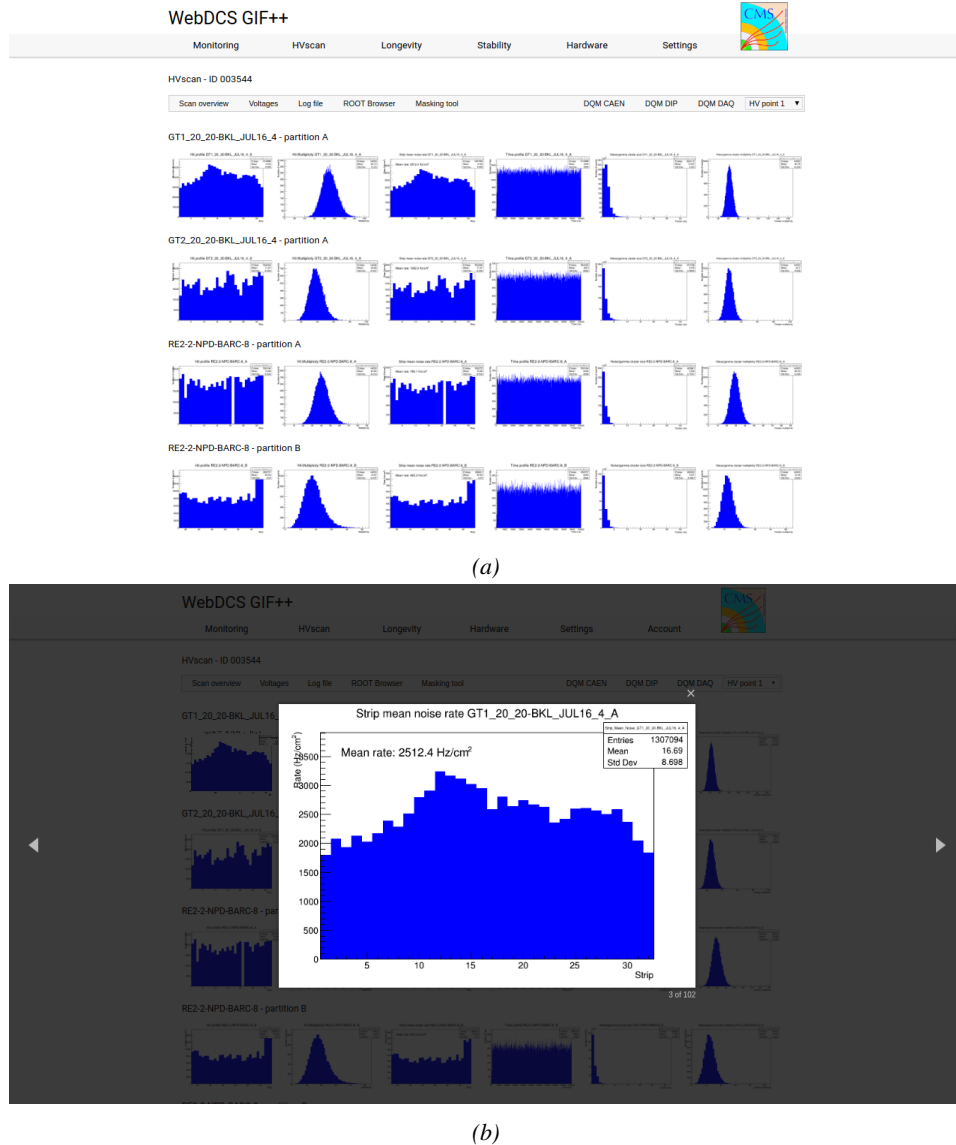


Figure 5.31: Example of DQM page available on CMS WebDCS at the Gif++: the histogram of the rate measured in one of the tracking chambers is selected and displayed above the page.

4109 The data recorded during efficiency and rate scans always consists of two ROOT files per run, where
 4110 each run corresponds to a certain HV point. One of the files contains the TDC data, a collection

of hits and time stamps per active channel on the read-out of the RPCs, while the second is the CAEN main frame data, i.e. the detector currents and high voltages. The data are systematically analysed at the end of each scan using the Offline Analysis tool of Gif++, detailed in Appendix B, that produces histograms such as hit, rate and time profiles, hit multiplicities, gamma cluster sizes or multiplicities for the DQM display of the WebDCS, as shown in Figure 5.31. More histograms can be accessed through the ROOT browser included in the WebDCS, as shown in Figure 5.32. Moreover, the analysis performed with the Offline tool provides final results for the rate scans. On the contrary, the algorithm for efficiency calculation is kept simple and approximative in the tool. Including tracking into the analysis requires manual adjustment for each individual scan as the positions of the trolleys with respect to each other may vary.

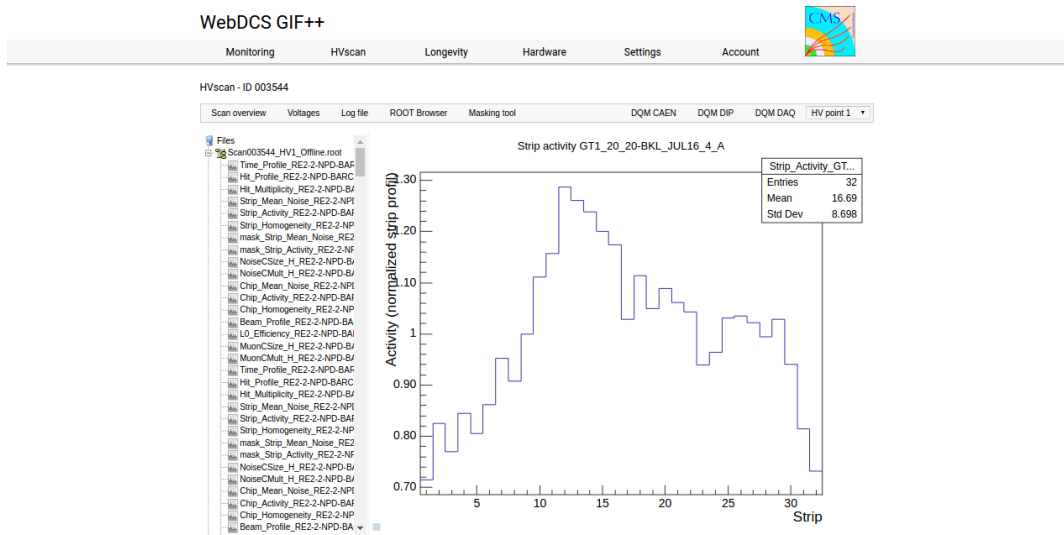


Figure 5.32: Example of DQM ROOT Browser page available on CMS RPC WebDCS at the Gif++: the strip activity profile, defined as the rate profile normalized to the mean rate, in one of the tracking chambers. Available ROOT files and histograms can be browsed thanks to the left panel showing the directory and files structures.

5.3.5 Measurements performed during irradiation periods

Even though test beam periods are stressful times as an extensive data taking program needs to be finalized in a short amount of time, the biggest amount of data actually comes from irradiation periods. Indeed, when T1 is moved back to its ageing position in between each test beam periods, data is recorded at any time the source can be switched ON for irradiation. Other experiments in the area might prevent the source from staying open continuously. As an example, the time efficiency of irradiation of CMS RPC detectors in Gif++ is presented in Figure 5.33.

Several types of measurement are performed throughout the irradiation period. As long as the detectors are being irradiated, a monitoring of the currents is performed to evaluate the corresponding integrated charge over the total irradiation time. Moreover, in order to spot any signs of ageing, the gamma rates seen by the chambers at the chosen source absorber setting as well as the noise rates and dark currents are periodically measured. During irradiation periods this is looked at every week

4133 via HV scans performed at various source settings. The weekly scans involve both the irradiated but
 4134 also the reference chambers, providing with a weekly monitoring of the evolution of the irradiated
 4135 chambers noise, gamma rate and dark current. Measuring with all detectors at the same time also
 4136 allows getting rid of potential systematics that might make the rates (noise or gamma) vary from one
 4137 measurement to another. If such systematic effects occur, they will be observed in all detectors.

4138 Finally, the resistivity is measured periodically during the year, generally before or after test
 4139 beam periods, by the use of Argon breakdown technique. The method consists in filling the detector
 4140 volume with Argon instead of the CMS standard gas mixture and to increase the voltage while
 4141 monitoring the current. Beyond an electric field of about 1 kV mm^{-1} at the Gif++ environmental
 4142 conditions, Argon turns into a conductive plasma and does not offer electric resistance anymore. The
 4143 monitoring of the currents beyond the breakdown voltage can then be used to calculate the resistivity
 4144 of the electrode material.

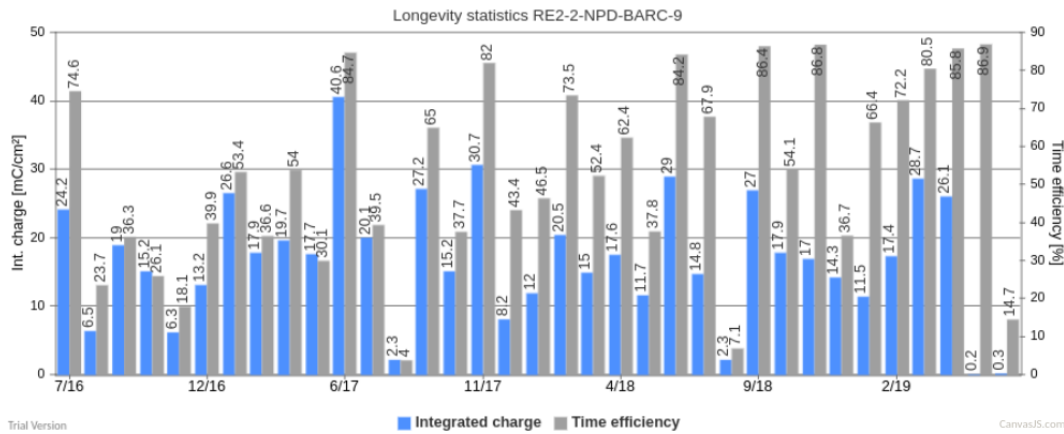


Figure 5.33: Longevity data for the irradiated RE2 chamber in Gif++. For each month since July 2017, the integrated charge (in blue) as well as the time efficiency of irradiation (in gray) is reported.

4145 5.3.5.1 Longevity scans

4146 The main activity of irradiation periods consists of the *longevity scans* during which the currents of
 4147 the irradiated chambers are continuously monitored. The two irradiated chambers are both brought
 4148 to a voltage of 9.8 kV while the source flux can vary depending on the needs of the groups using the
 4149 facility. The currents are monitored for each active gas volume as can be seen in Figure 5.34. The
 4150 integrated charge for each individual gas volume is computed by integrating through time the current
 4151 density, current normalised to the surface area, flowing through each gap, as shown in Figure 5.35.

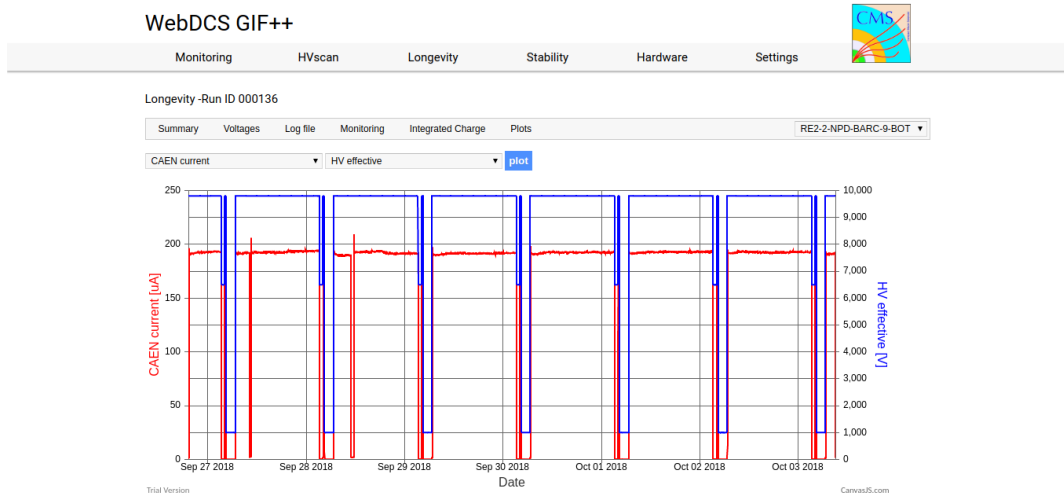


Figure 5.34: Example of a longevity scan monitoring page available on CMS RPC WebDCS at the GIF++: the current and effective voltage, as well as environmental parameters, are monitored for the bottom gap of the irradiated RE2 chamber. The decrease of current is related to a decrease of the voltage due to the daily rate scan procedure or to periods during which the source was turned OFF.

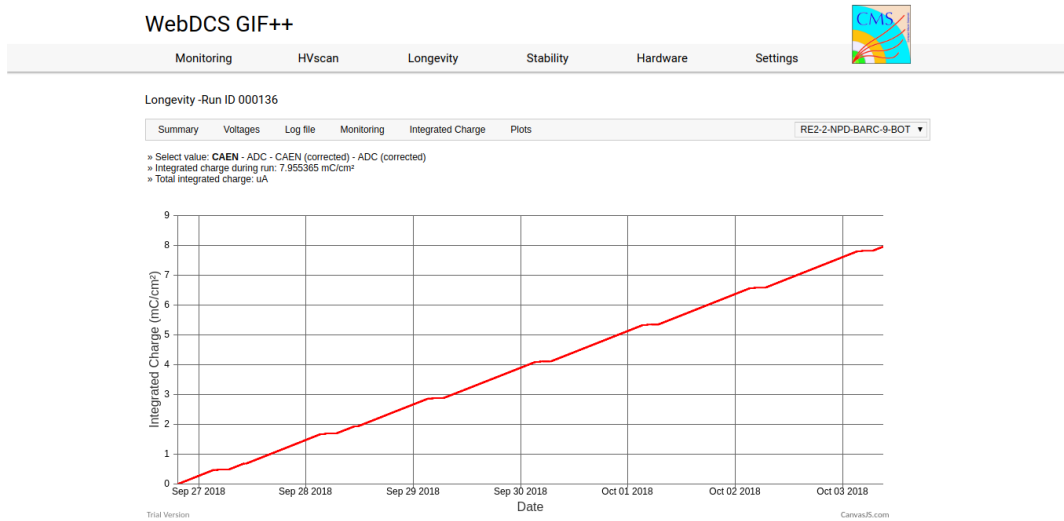


Figure 5.35: Example of a longevity scan summary page available on CMS RPC WebDCS at the GIF++: the integrated charge is computed for the bottom gap of the irradiated RE2 chamber.

Finally, at the end of each longevity scan each gap contribution is translated into the mean chamber integrated charge. The integrated charge accumulated in each chamber is used to update the

4152
4153

4154 summary plots providing the collaboration with official results to be spread as can be seen from
 4155 Figure 5.36. The translation from individual gap currents to total integrated charge in the chamber
 4156 is done using Equation 5.5, where the equation to compute the monitored current density already
 4157 mentioned in Section 5.2.4 is recalled.

$$(5.5) \quad J_{mon} = \frac{I_{mon}^{TW} + I_{mon}^{TN}}{A_{TW} + A_{TN}} + \frac{I_{mon}^B}{A_B}$$

$$Q_{int} = \int_{t_i}^{t_f} J_{mon} dt$$

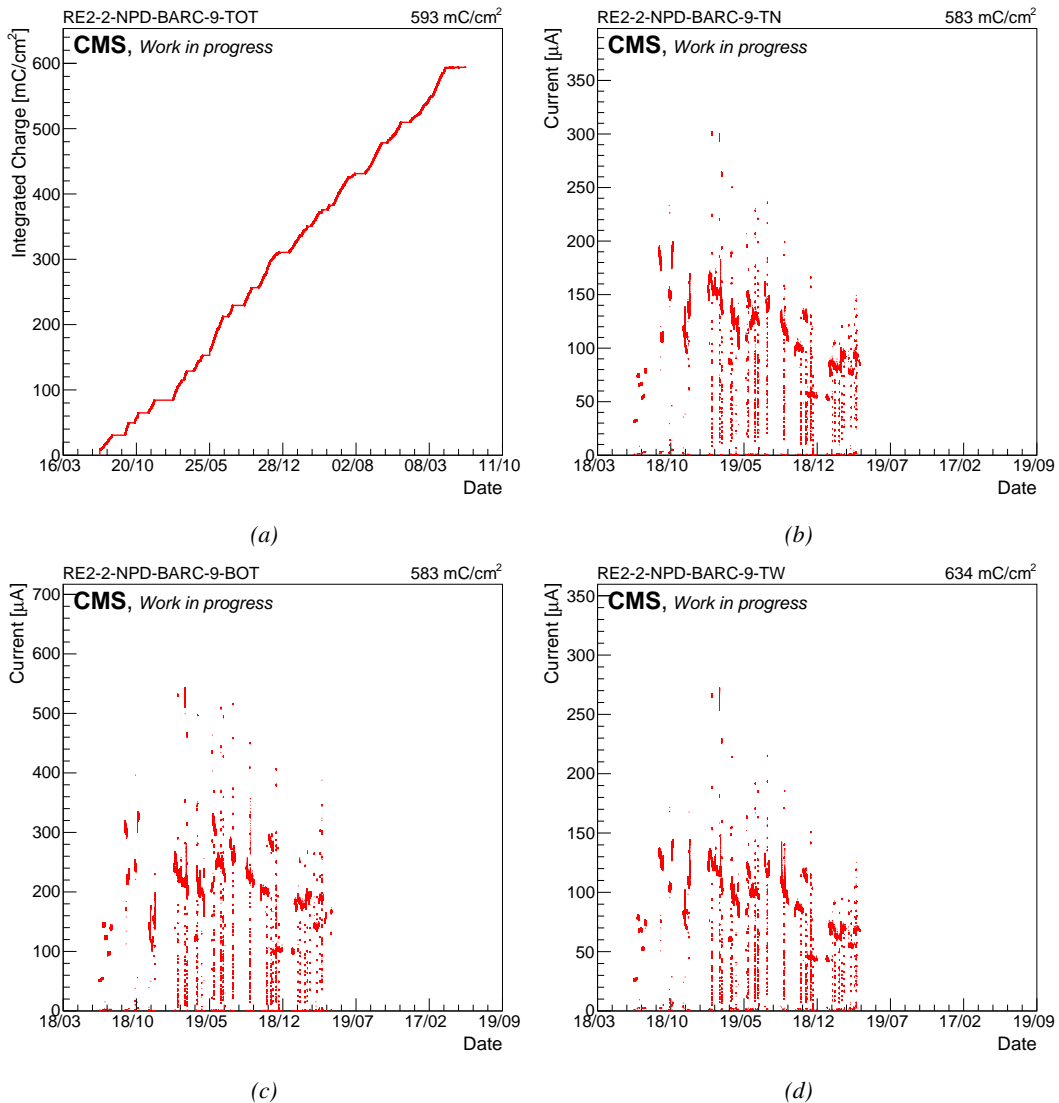


Figure 5.36: Example of current monitoring summary (top wide (a), top narrow (b) and bottom (c) gap currents) and of corresponding integrated charge (d) of the irradiated RE2 chamber.

4158 5.3.5.2 Daily rate monitoring scans

4159 Every night during longevity scans, the setup performs *daily rate scans*. These scans aim at keeping
4160 track of the gamma rate measured in the irradiated RPCs during longevity scans, but are also used
4161 to measure the noise rate at standby voltage for each gap. The procedure for these HV scans consist
4162 of nine runs for which 50,000 random triggers are accumulated, corresponding to 0.5 s of total
4163 integrated time.

4164 1- All gaps are first left at the irradiation voltage of 9.8 kV to measure the gamma rate.

4165 2- Then all gaps are brought to the standby voltage of 6.5 kV to measure the noise rate of the full
4166 detectors.

4167 3- Both top gaps (TW and TN) are brought to a voltage equivalent to an OFF status, i.e. 1 kV so
4168 that the noise contribution of only the bottom gap at standby voltage can be measured.

4169 4- The bottom gaps are ramped up toward the working voltage of 9.8 kV to measure their contri-
4170 bution to the gamma rate estimation.

4171 5-8 The steps 3 and 4 are repeated on TN and then on TW, keeping the bottom and the top gap
4172 which is not of interest at a voltage of 1 kV. This way, the individual contribution to the noise
4173 and gamma rates are known.

4174 9- Both TW and TN are brought to working voltage while the bottom gap is left at 1 kV to
4175 measure the gamma rate for the full top layer at once.

4176 Finally, the voltages of all gaps are brought back to working voltage for the longevity program to
4177 continue until the next daily scan. These scans are responsible for the drop of voltages and currents
4178 observed in Figure 5.34. The procedure previously described is highlighted in Figure 5.37.

4179 Similarly to the efficiency and rate scans taken during test beam periods, the data is here stored
4180 in two separate ROOT files for the TDC and CAEN data for each run. At the same time, the currents
4181 are still monitored by the longevity scan and saved into the GIF++ database for an easy evaluation
4182 of the currents to the integrated charge. The Offline Analysis tool then provides the DQM page with
4183 histograms, and daily values can be compiled into long term monitoring plots to study the variations
4184 of rate and current with increasing integrated charge, as presented in Figure 5.38. The variations
4185 of the rate and current are correlated and correspond mainly to change of source irradiation, gas
4186 flow, gas humidity, or environmental conditions. The rates on every single read-out channel are
4187 also tracked to control their activity with increasing integrated charge and, this way, understand
4188 the appearance of hot spots through noisy channels, as shown in Figure 5.39. The activity of a
4189 strip is defined as the rate of the individual channel normalized to the mean rate measured in the
4190 corresponding read-out partition.

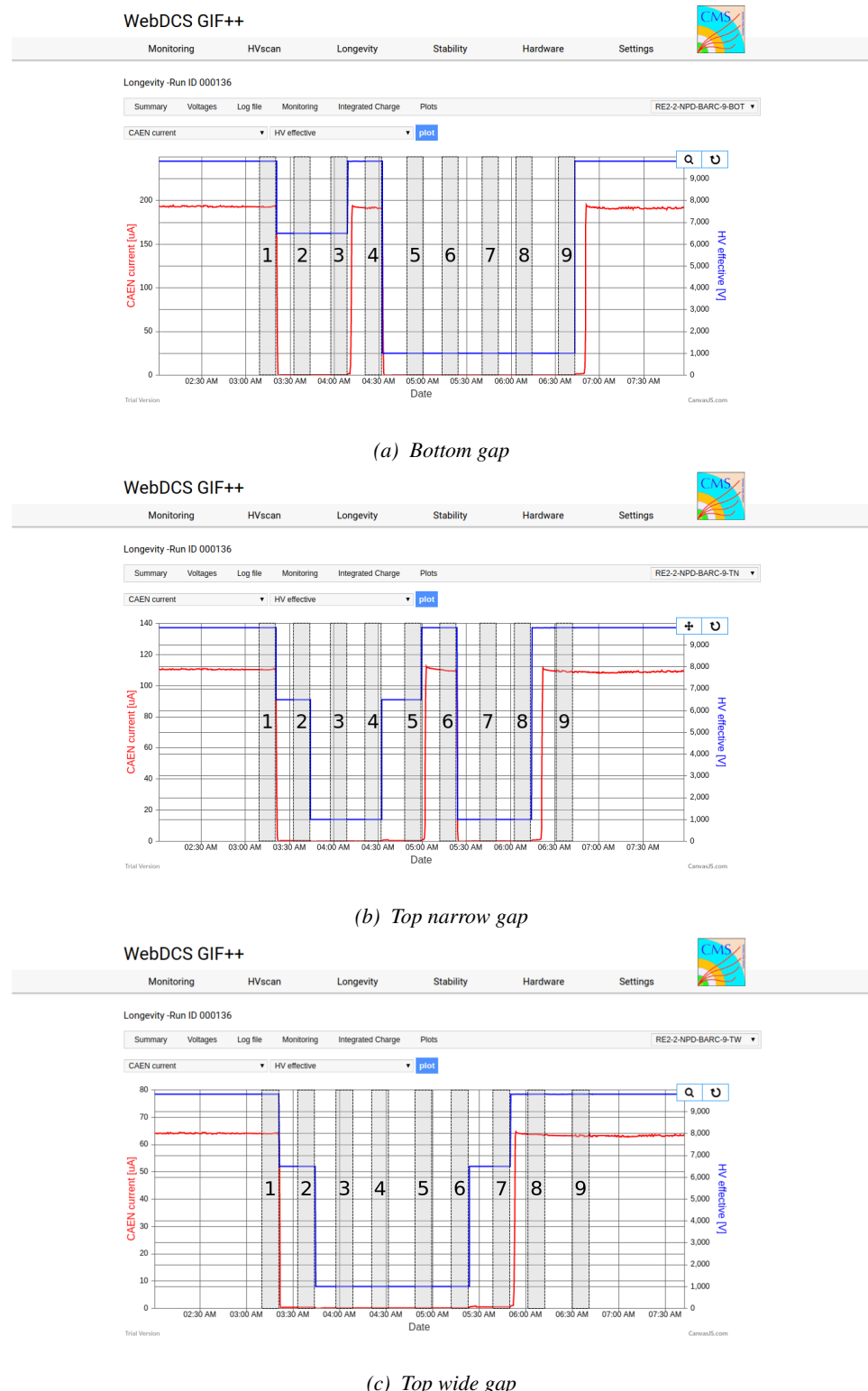


Figure 5.37: Example of daily scan procedure of the irradiated RE2 chamber with highlighted runs on the CMS RPC WebDCS at the Gif++.

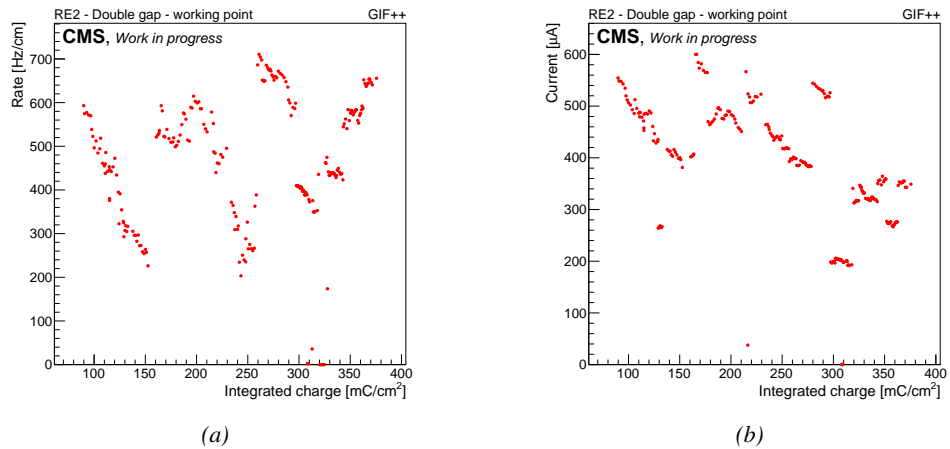


Figure 5.38: Example of rate (a) and current (b) monitoring of the irradiated RE2 chamber at working voltage in double gap mode (step 1) with increasing integrated charge.

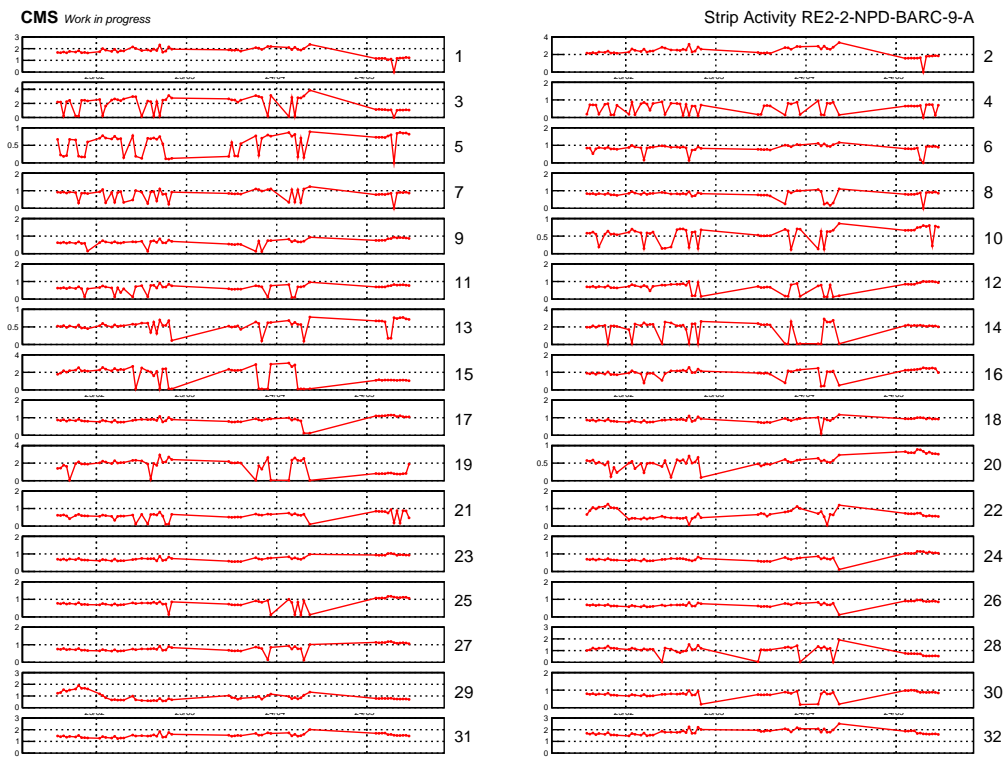


Figure 5.39: Example of strip activity of the irradiated RE2 chamber monitored over time.

4191 5.3.5.3 Weekly noise monitoring scans

4192 Once a week, the source is turned OFF to make a noise scan for the CMS RPC. This HV scan is
 4193 composed of six runs for which 25,000 random triggers are accumulated. The first run is taken at

standby voltage and the second one at 8 kV. The next five runs are taken at voltages ranging from 9.4 to 9.8 kV in order to access for both type of chambers, RE2 and RE4, in the voltage region where the efficiency rises and reaches its plateau. The whole procedure is shown in Figure 5.40. On the occasion of this scan, the ongoing longevity scan is stopped. A new one will be started once the weekly scans are over.

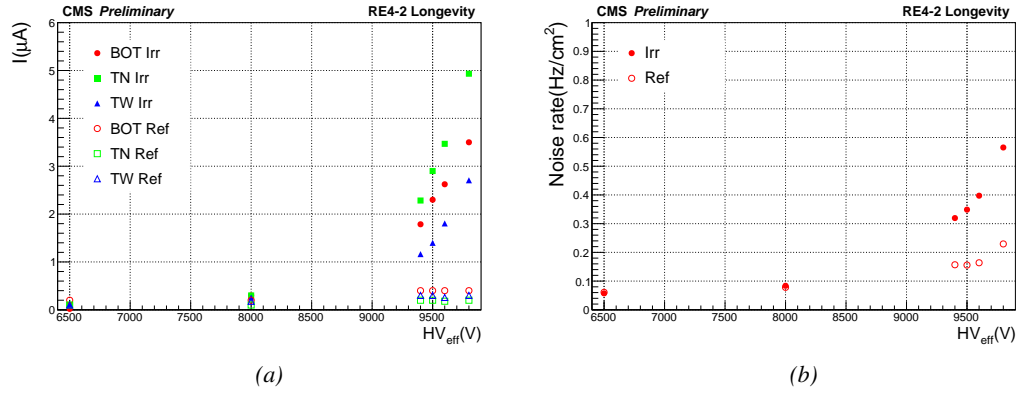


Figure 5.40: Example of rates (a) and currents (b) of the irradiated and reference RE4 chambers measured during a weekly noise scan.

5.3.5.4 Weekly source scans

Directly following the weekly noise scans, HV rate scans are organised at different source settings (usually ABS 6.8, 4.6 and 3.3). The procedure of these HV scans consists of nine runs for which 25,000 random triggers are accumulated. The first run is taken at standby voltage while the next eight runs are taken at voltages ranging from 9.4 to 10.1 kV. They aim at measuring the gamma rate to which the chambers are subjected and the related currents. The whole procedure is shown in Figure 5.41.

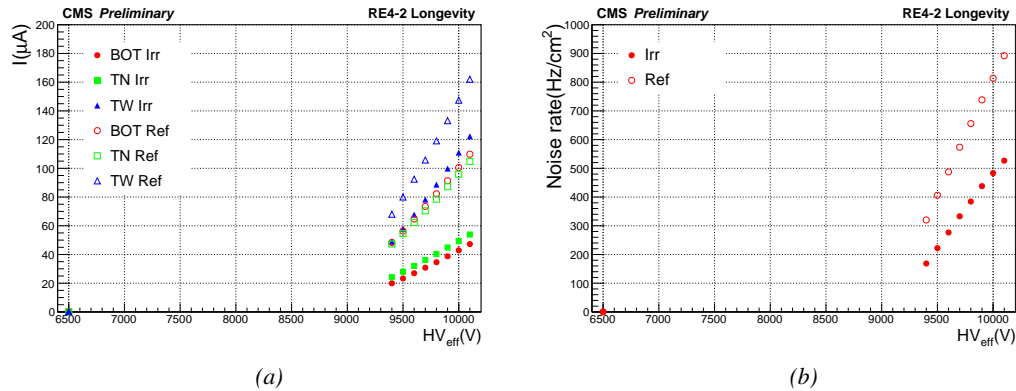


Figure 5.41: Example of rates (a) and currents (b) of irradiated and reference RE4 chambers measured during a weekly source scan. The data were measured with ABS 123 (6.9).

5.3.5.5 Weekly current scans

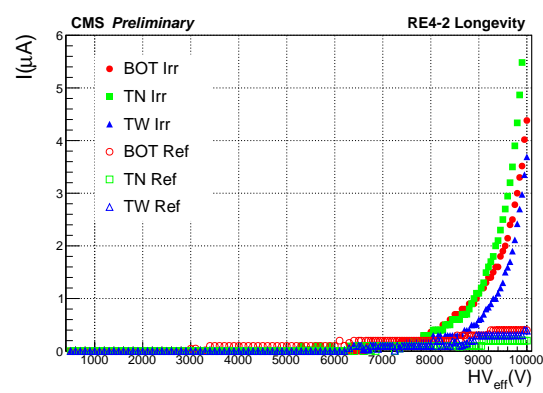


Figure 5.42: Example of currents of irradiated and reference RE4 chambers measured during a weekly current scan.

current driven through the four detectors, are performed at 131 high voltage points in between 500 V and 10 kV, in steps of 100 V until the standby voltage of 6.5 kV is reached and then in steps of 50 V. At low voltage, the current rise is slow and is only driven by the resistance of the detector electrode and thus increases linearly. It is referred to as the *ohmic current* as opposed to the *physics current* corresponding to the voltage region where charge multiplication starts to occur. A fit on the ohmic current range gives access to the resistance of the 'electrodes/gas' system. If any variation of the electrode resistance occurs, the global resistance will increase and so will the current. Technically, these scans will record a ROOT file per HV step that will have the same format as the CAEN ROOT file saved during other HV scans. The data is also analysed using the Offline Analysis tool to provide with DQM histograms as well as standardized I/V tables.

5.3.6 Extraction and monitoring of the resistivity

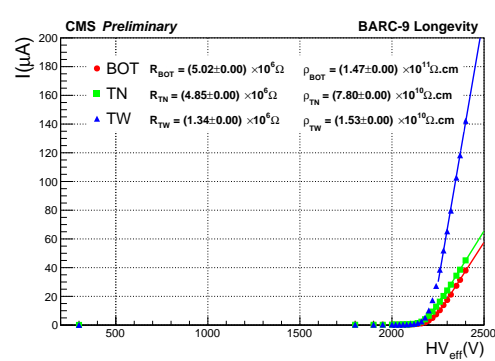


Figure 5.43: Example of currents of the irradiated RE2 chamber measured during an argon scan. The resistance is extracted from the linear fit and the resistivity is computed using Equation 5.6.

the couple of electrodes R_{elec} is extracted as can be seen from Figure 5.43. The resistivity is then deduced by using Formula 5.6 where S is the surface area of the gap and l the thickness of a single

The previously detailed daily rate scans, but also the weekly noise and source scans are interesting tools to look at an increase of noise rates and dark currents or at a loss of rate capability. They could point to an increase of surface resistivity of the electrodes through the absorption of hydrofluoric acid. Nevertheless, periodically measuring the currents on wider high voltage ranges allows to have access to the ohmic part of the current driven by the detectors related to the electrodes resistance. This is why precise current scans, consisting only in measuring the each week. The scan procedure includes

A critical parameter to monitor is the resistivity of the electrodes. Its variation would impact the rate capability of the RPC. An increase of the resistivity with increased irradiation is expected. In the first place, the measurement of the resistivity of the electrodes is done using the so called *Argon scans*. Such tests are performed regularly before or after test beam periods through high voltage scans of the detectors operated with pure Argon. The electric field strength at which Argon breaks down being well known, the current beyond the breakdown voltage is monitored. Assuming a relation $I_{mon} = HV_{eff}/R_{elec}$ beyond the breakdown voltage, the resistance of

4250 electrode.

$$(5.6) \quad \rho = R \times \frac{S}{2 \times l}$$

4251 There exist other ways to access a quantity directly related to the resistivity. During the testbeam
 4252 periods, the efficiency of the detectors is measured with both source OFF and source ON with high
 4253 irradiation. The shift of voltage introduced by an irradiation is directly linked to the rate capability
 4254 of the detector and hence to the resistivity of the electrodes. By comparing the efficiency curves
 4255 observed with source ON and OFF during a single testbeam, it is possible to access the local mean
 4256 resistance of the detector during a testbeam period. Knowing the dimensions of the electrodes, this
 4257 value can be compared to the resistivity directly measured using the argon scans. It also provides a
 4258 tool to compare different testbeam results by getting rid of the bias introduced by the fluctuation of
 4259 the resistivity through time. The mean resistance is computed as in Formula 5.7.

$$(5.7) \quad R = \frac{\Delta HV}{\Delta I} = \frac{HV^{ON} - HV^{OFF}}{I^{ON} - I^{OFF}}$$

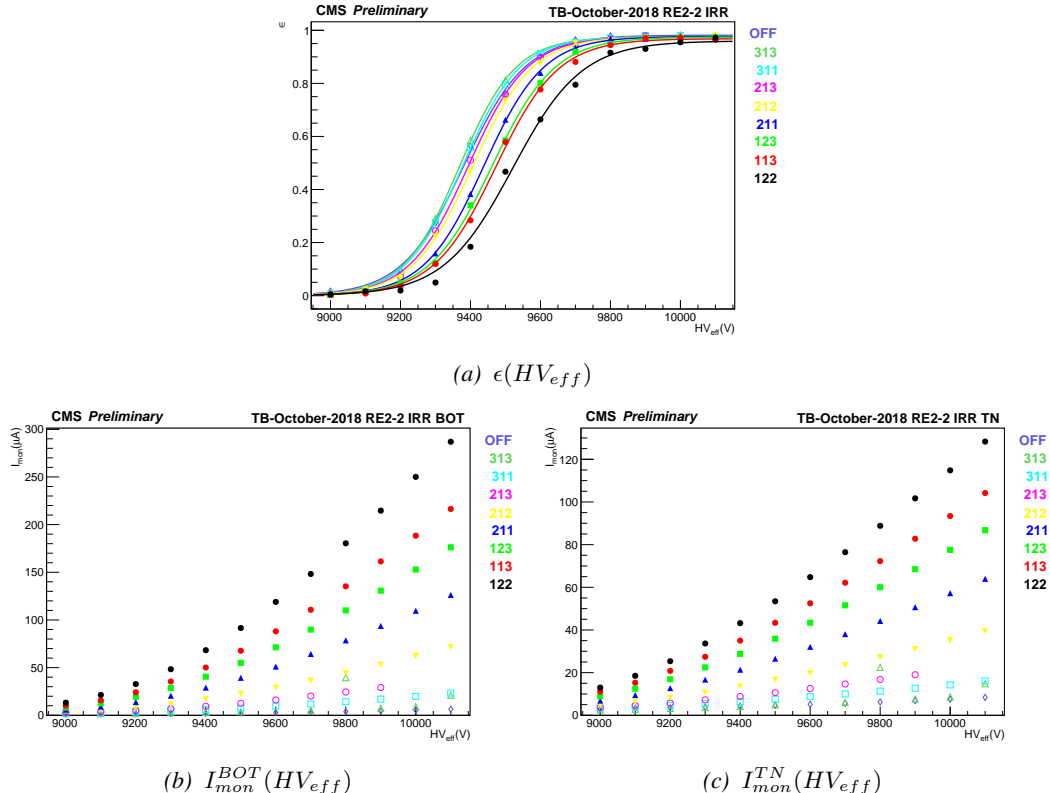


Figure 5.44: Efficiency (a) and monitored currents of the bottom (b) and top narrow (c) gaps as a function of the effective voltage of the irradiated RE2 chamber during October 2018 testbeam period.

4260 It is important to note that the result provided by using this method will only concern the re-
 4261 sistance of the detector under the beam, including the little contribution of the resistance of the gas
 4262 volume itself. The translation to the resistivity of the electrodes is not straight forward even though
 4263 the result falls in the same order of magnitude. Also, the quality of the resistance extraction depends
 4264 on which level of irradiation is available in the data. During October 2018 testbeam period, HV
 4265 scans were done on partition C of the RPCs (bottom and top narrow gas gaps) with source OFF and
 4266 with eight diffent ABS values: ABS 313 (464), ABS 311 (100), ABS 213 (46.4), ABS 212 (21.5),
 4267 ABS 211 (10), ABS 123 (6.9), ABS 113 (4.6) and ABS 122 (3.2). T1 was placed close to the bunker
 4268 upstream wall at a distace of 5.6 m from the source. This position corresponds to a gamma current
 4269 of the order of $5 \times 10^5 \text{ cm}^{-2} \text{ s}^{-1}$ with source fully open.

4270 In a first step, the efficiency sigmoids as well as the bottom and top narrow gaps' monitored
 4271 current as a function of the effective voltage were retrieved as can be seen from Figure 5.44. The
 4272 goal is to compute the value of the effective voltage at the knee HV_{knee} of the sigmoids. The knee
 4273 where $\epsilon = 0.95 \times \epsilon_{max}$ would be the best location to extract the value of the resistivity. At this point,
 4274 the performance of the detectors is stable and a little variation of voltage does not have a large effect
 4275 on the efficiency. The effective voltage at the knee is given by Formula 5.8.

$$(5.8) \quad HV_{knee} = HV_{50} + \frac{\ln(19)}{\lambda}$$

4276 The monitored current at the knee I_{knee}^G for each gap G is then computed by extrapolating from
 4277 the monitored currents value located around HV_{knee} as in Formula 5.9 where I_{\downarrow}^G and HV_{\downarrow}^G are the
 4278 monitored current and the effective voltage at the voltage point bellow the knee and I_{\uparrow}^G and HV_{\uparrow}^G
 4279 are the monitored current and the effective voltage above the knee.

$$(5.9) \quad I_{knee}^G = I_{\downarrow}^G + (I_{\uparrow}^G + I_{\downarrow}^G) \times \frac{HV_{knee} - HV_{\downarrow}^G}{HV_{\uparrow}^G - HV_{\downarrow}^G}$$

4280 Once the values of the monitored currents are known at the knee, the mean current flowing
 4281 through the gaps at the level of the studied partition P can be computed. First of all, the currents at
 4282 knee of the gaps in the beam line is normalised to the area of the gap active area seen by the local
 4283 read-out partition $S^{G,P}$. Then the mean current at knee \bar{I}_{knee}^P is computed by ponderating the local
 4284 currents $I_{knee}^{G,P}$ of each gap by their respective active area in the partition.

$$(5.10) \quad \begin{aligned} I_{knee}^{G,P} &= \frac{I_{knee}^G \times S^{G,P}}{S^G} \\ \bar{I}_{knee}^P &= \frac{I_{knee}^{1,P} \times S^{1,P} + I_{knee}^{2,P} \times S^{2,P}}{S^{1,P} + S^{2,P}} \end{aligned}$$

4285 The variation of effective voltage and mean monitored current at the knee in between the Source
 4286 OFF and ON scans can then be obtained. The local resistivity of the detector can finally be calculated
 4287 combining Formula 5.6 and Formula 5.7. This process is performed for every scan of each approved
 4288 test beam period as can be seen in Figure 5.45. Finally, the most probable resistivity during the test
 4289 beam period is obtained thanks to a constant fit. The value of the mean partition resistivity displayed
 4290 in Figure 5.45 is of the same order than what would be expected for CMS RPCs.

Later, the value extracted from this method will be used to compare the efficiency sigmoids of the different testbeam periods. During the operation of the detector without irradiation, the voltage drop across the detector almost only consists in a voltage drop across the gas volume. As the electrodes behave approximately as charged capacitors, there is only a negligible voltage drop across their volume. The charge of the electrodes is only affected locally by the charge carriers freed by avalanches in the gas volume. Nevertheless, under irradiation, the conversion of photons is uniform throughout the electrodes' volume and charge recombination happens everywhere at the same time making it impossible for the electrodes to stay charged. Hence, a significant part of the voltage drop appears across the electrodes, explaining the usual voltage shift observed in the performance of irradiated RPCs. The data comparison will then be done using the gas voltage drop HV_{gas} obtained by correcting the effective voltage HV_{eff} thanks to Formula 5.11 in which R is the resistance computed at the knee using Formula 5.7 in the RPC partition of interest and \bar{I} is the mean current in this partition at each voltage step.

$$(5.11) \quad HV_{gas} = HV_{eff} - R \times \bar{I}$$

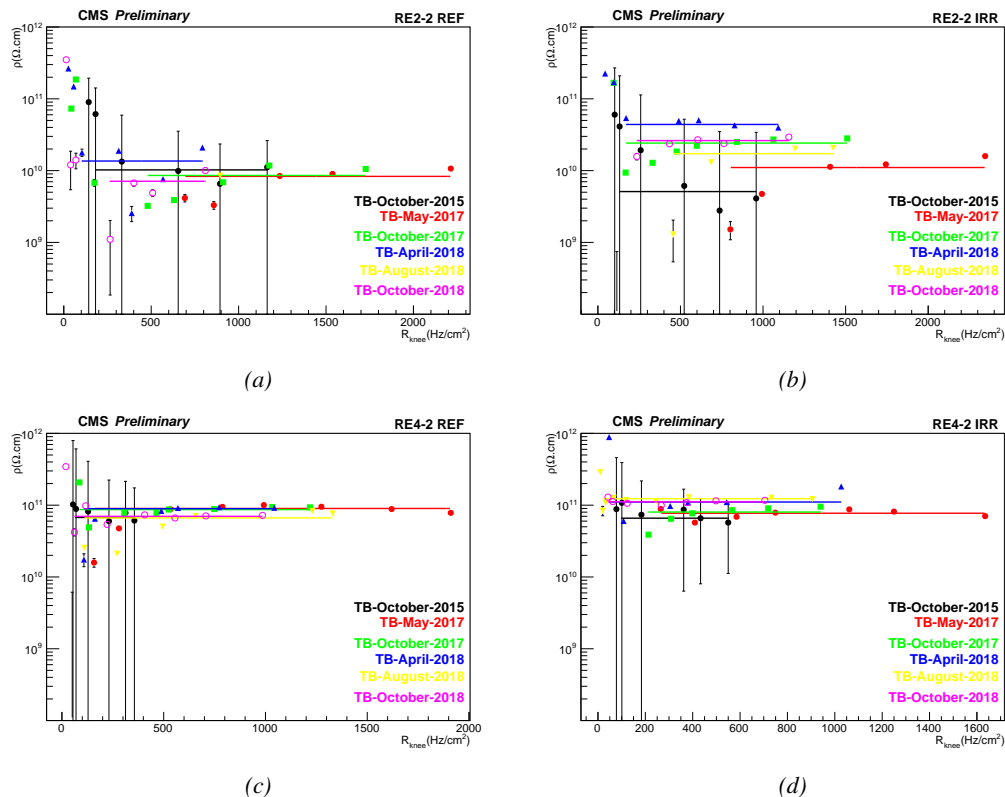
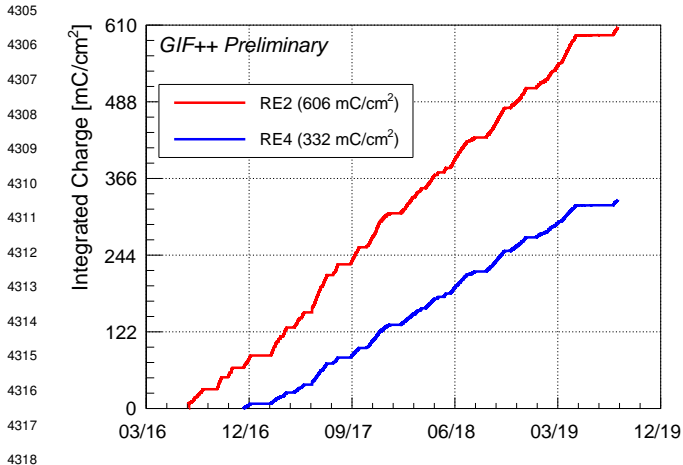


Figure 5.45: Resistivity extraction for all approved test beam periods for the reference RE2/2 (a) and RE4/2 (c) chambers and the irradiated RE2/2 (b) and RE4/2 (d) chambers.

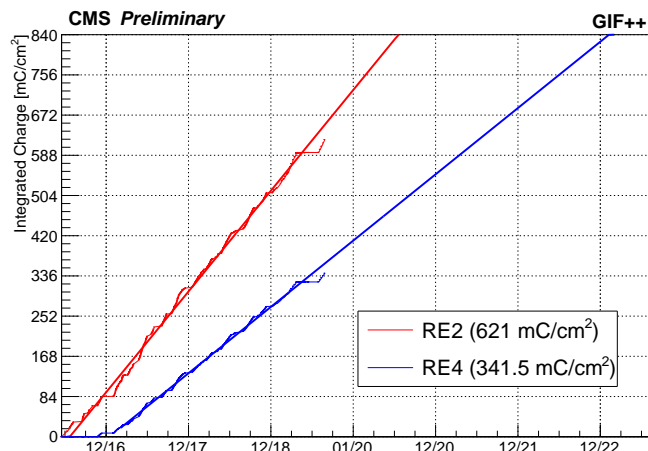
4304 **5.3.7 Results and discussions**



4319 *Figure 5.46: Total integrated charge in both the irradiated RPCs*
4320 *in July 2019. The irradiation of the RE2 chamber started early July*
4321 *2016 while the RE4 chamber couldn't be irradiated before end of*
4322 *November 2016.*

4323 live through HL-LHC or not. The charge accumulation of the RE2 detector is faster than which
4324 of the RE4 and is expected to end within a year. In the case of the RE4 RPC, the irradiation would
4325 go on for more than two years at the current charge accumulation rate. This time would be reduced
4326 after the end of the longevity study of the RE2 by placing the trolley hosting the detectors closer to
4327 the source.

Since 2015, CMS RPCs have been irradiated at the GIF++ with the goal to reach a total integrated charge per irradiated detector of $0.84 \text{ C}/\text{cm}^2$ while certifying the detectors to a single hit rate capability of $600 \text{ Hz}/\text{cm}^2$. At the time of writing, the RE2 and RE4 chambers were exposed to 74 and 40% of their total irradiation program respectively, as shown in Figure 5.46. According to Figure 5.47, a few years of irradiation are expected before reaching the end of the longevity study for both types of detectors and before reaching a final answer on whether the present CMS RPC system will be able to



4328 *Figure 5.47: Linear projection of the time necessary to finish the longevity program on the RE2 and RE4*
4329 *detectors at the GIF++.*

4328 5.3.7.1 Long term monitoring of the RPC parameters

4329 Throughout the longevity program, great care was put into monitoring the detector characteristics.
 4330 While presenting the results, current densities expressed in $\mu\text{A}/\text{cm}^2$ will be showed in the place of
 4331 currents. In the first part of the discussion the current densities will be referred to as "dark current".
 4332 Also, the data of the reference detectors will be displayed with increasing integrated charge. This
 4333 integrated charge will always refer to the integrated charge of the irradiated detectors.

4334 Using the data collected during the weekly noise scans performed on all four RPCs, the dark
 4335 currents are monitored. Two voltage of interest are being compared through time. The first value
 4336 of interest was chosen at a *STANDBY* voltage of 6500 V where no multiplication process happens.
 4337 This is done to follow the variations of the ohmic component of the current. The monitored dark
 4338 current in *STANDBY* are shown in Figure 5.48. At the time of writing, the ohmic currents for all
 4339 detectors are stable. Both RE4 detectors appear to follow the same trend while the ohmic current
 4340 of the irradiated RE2 detector has increased a little. Nevertheless, this increase is only of 10 to
 4341 20 pA/cm^2 and a similar behaviour can be observed for both RE4 detectors. There is no reason to
 4342 associate the increase in ohmic current with the irradiation.

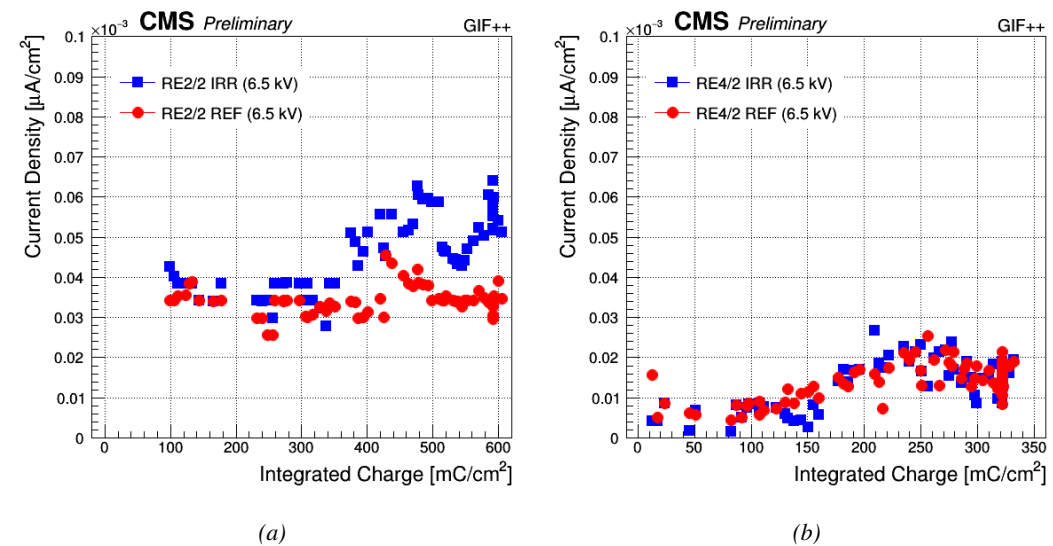


Figure 5.48: Monitoring of the ohmic component of the dark current with increasing integrated charge at a voltage of 6500 V of the RE2 (a) and RE4 (b) detectors installed at the GIF++.

4343 The second value of interest is located in the gain region near the working point at a voltage
 4344 of 9600 V for the RE2 detectors and of 9500 V for the RE4 ones. Monitoring the multiplication
 4345 region allows to spot the appearance of hot spots across the detectors' areas. A local damage to the
 4346 electrode could result in an increase of local discharges and an overall increase of the current drawn
 4347 by the detector which would show in the monitored values. Near the working voltage, in addition to
 4348 the current densities, the noise rate per unit area are monitored as can be seen in Figure 5.49. In the case
 4349 of the RE2 detectors, the dark currents and noise rate stay stable since the beginning of the irradiation
 4350 program. The variability of the dark current of the irradiated chamber is higher than the one of the
 4351 reference chamber but seem to always come back between 0.1 and 0.15 nA/cm^2 . Concerning the
 4352 RE4 detectors, both chambers are very stable up to an irradiation of 150 mC/cm^2 .

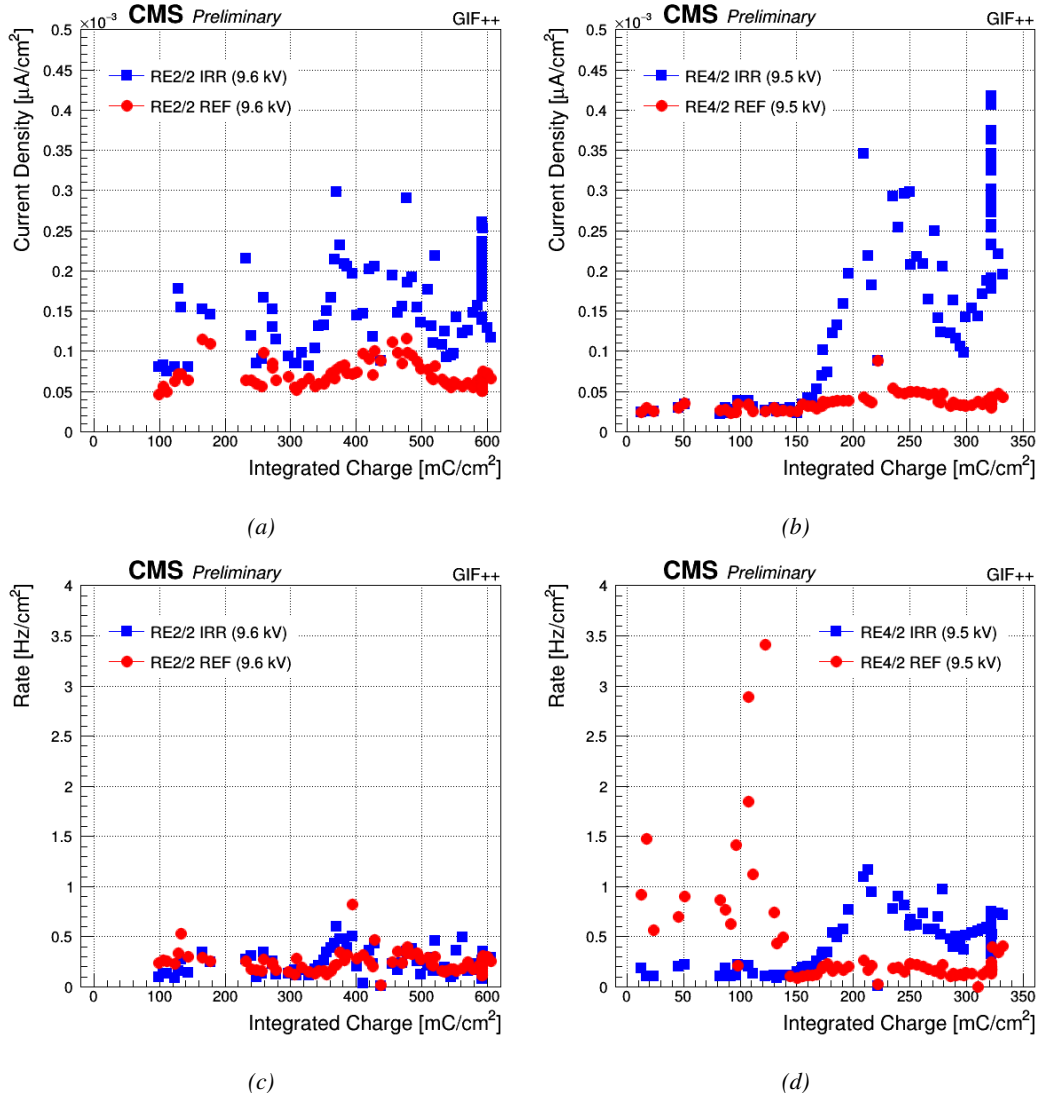


Figure 5.49: Monitoring of the physics component of the dark current and of the noise rate per unit area with increasing integrated charge at a voltage of 9600 V for the RE2 detectors (a) and (c) and at a voltage of 9500 V for the RE4 detectors (b) and (d) installed at the GIF++.

Even though the noise rate of the reference chamber seem to fluctuate a lot between 0.5 and 3.5 Hz/cm^2 before this value, the monitoring of the noise rate per unit area following this early range as well as the very stable dark current would suggest that the chamber was in fact suffering from a bad grounding. Indeed, beyond $150 \text{ mC}/\text{cm}^2$, the noise rate suddenly stabilizes between 0.1 and 0.2 Hz/cm^2 while the dark current increases very slightly to $50 \text{ pA}/\text{cm}^2$. On the contrary, the irradiated chamber which was very stable under $150 \text{ mC}/\text{cm}^2$, sees its dark current and its noise rate increase and fluctuate with a similar shape. The noise rate is still within the requirements of CMS. Indeed, an upper threshold of $1 \text{ Hz}/\text{cm}^2$ was considered to be good enough to prevent fake events due to noise. Regarding the dark current, so far the highest peak, reached a little higher

than 0.4 nA/cm^2 and have since dropped to 0.2 nA/cm^2 . During *source scans* at gamma rates per unit area usually above 400 Hz/cm^2 , the current densities are of the order of 10 nA/cm^2 , almost two orders of magnitude larger than the dark current. Nevertheless, both the noise rate and dark current have almost gained an order of magnitude at their highest monitored values and will need to be carefully followed at higher values of integrated charge.

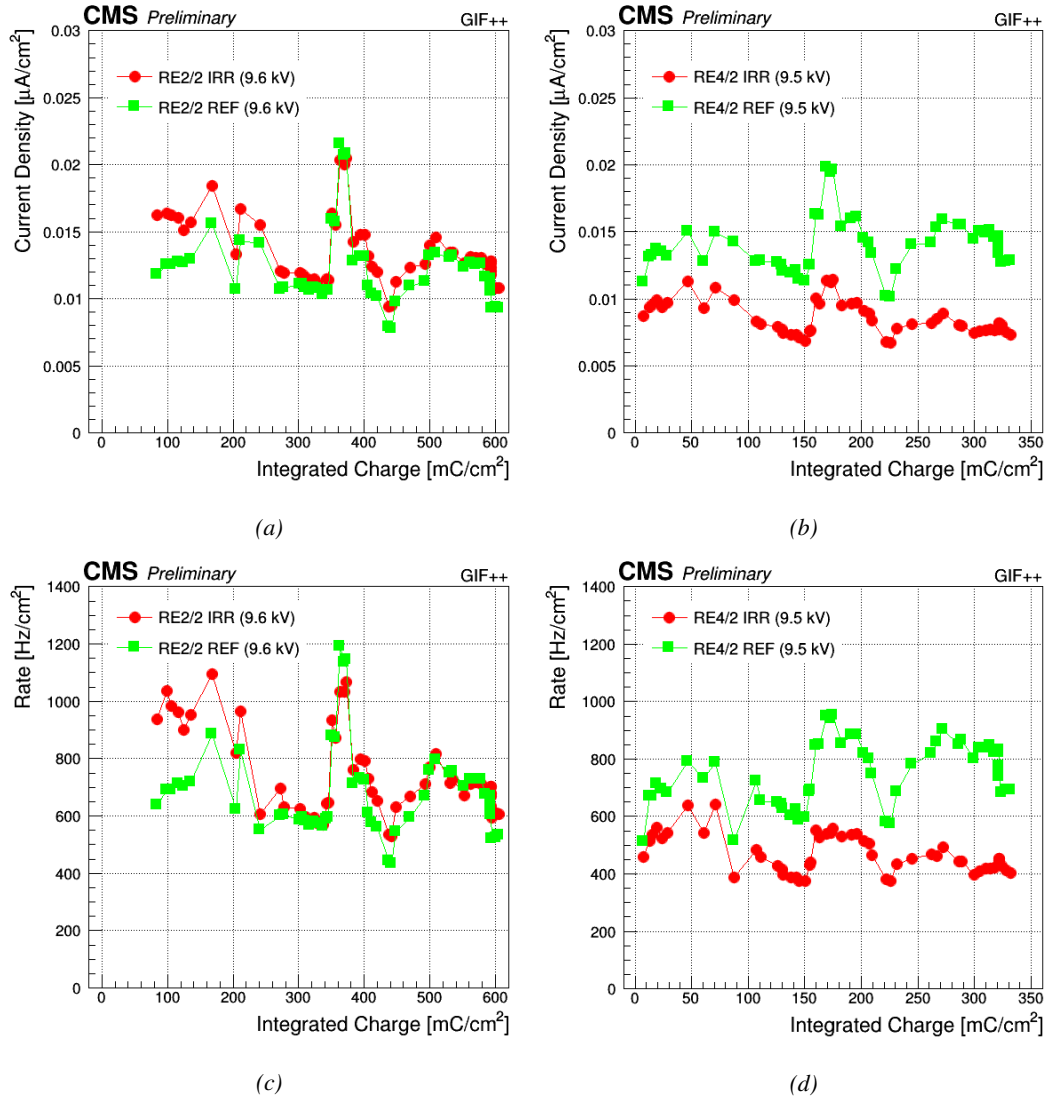


Figure 5.50: Monitoring of the current density and of the gamma rate per unit area under irradiation with increasing integrated charge at a voltage of 9600 V for the RE2 detectors (a) and (c) and at a voltage of 9500 V for the RE4 detectors (b) and (d) installed at the GIF++. The source irradiation is attenuated by a factor 6.9.

The same exercise is done using the data collected during the weekly source scans. The monitoring of the current densities and of the gamma rate per unit area is showed in Figure 5.50. The reported measurements are always performed with the same source conditions corresponding to an

4370 irradiation attenuated by a factor 6.9. The increase in dark current of the irradiated RE4 chamber
 4371 don't have any visible effect when the source irradiates the detectors. No signs of ageing due to
 4372 irradiation is yet to be seen for both the RE2 and RE4 detectors. The current densities and gamma
 4373 rates of all four detectors evolve following the same phases of increase and decrease, as confirmed
 4374 by Figure 5.51.

4375 The use of Principal Component Analysis (PCA) [279] reveals that the study of the correlations
 4376 between the current densities and the gamma rates can be reduced to a single dimension. To perform
 4377 the PCA, the algorithm used normalises each variable to get a mean value of 0 and a variance of
 4378 1 resulting in the study of the variance. The associated *Scree* plot [280] showed in Figure 5.51b
 4379 indicates for each of the components of the PCA, the eigenvalues of the covariance matrix. In this
 4380 case, the eigenvalues have been normalised to express the percentage of variance explained by each
 4381 component. More than 93% of the data variation can be explained using a simple linear composition
 4382 of the current density and of the gamma rate. It is expected as the current density and gamma rate
 4383 are two side of the same physical process. Any deviation would mean that other processes than the
 4384 conversion of photons in the electrode material take place.

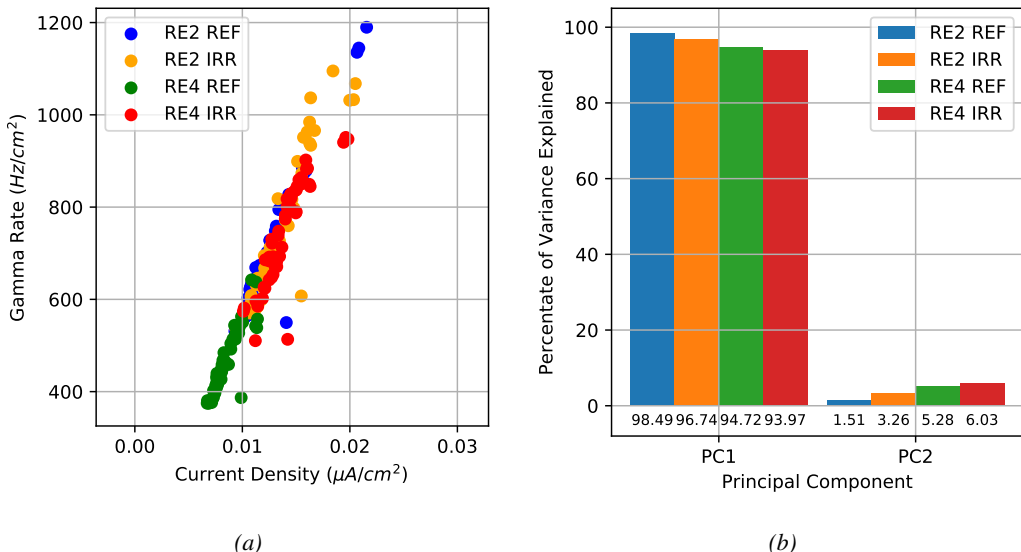


Figure 5.51: (a) Gamma rates as a function of the corresponding current densities. (b) Scree plot obtained at the output of PCAs performed on each set of current densities and corresponding gamma rates.

4385 The fluctuations observed on Figure 5.50 may arise due to different factors such as the environmental
 4386 conditions (gas temperature, gas relative humidity, environmental pressure) or the presence
 4387 of other experiments between the source. The distance from the source and the trolley, and the
 4388 gamma current at which the detectors are irradiated during the ageing procedure are kept as consistent
 4389 as possible and should not contribute to the fluctuations in current density and gamma rate. In
 4390 order to have a better understanding, the monitoring of the environmental parameters, i.e. the gas
 4391 relative humidity and temperature both at the supply and at the exhaust of the trolley together with the
 4392 humidity and temperature inside of the bunker and the environmental pressure, is showed in Figures
 4393 5.52, 5.53 and 5.54. In these Figures, the data are displayed with increasing integrated charge
 4394 in the case of the RE2 and of the RE4 detectors for comparison purposes. Each value of integrated

4395 charge corresponds to a unique date.

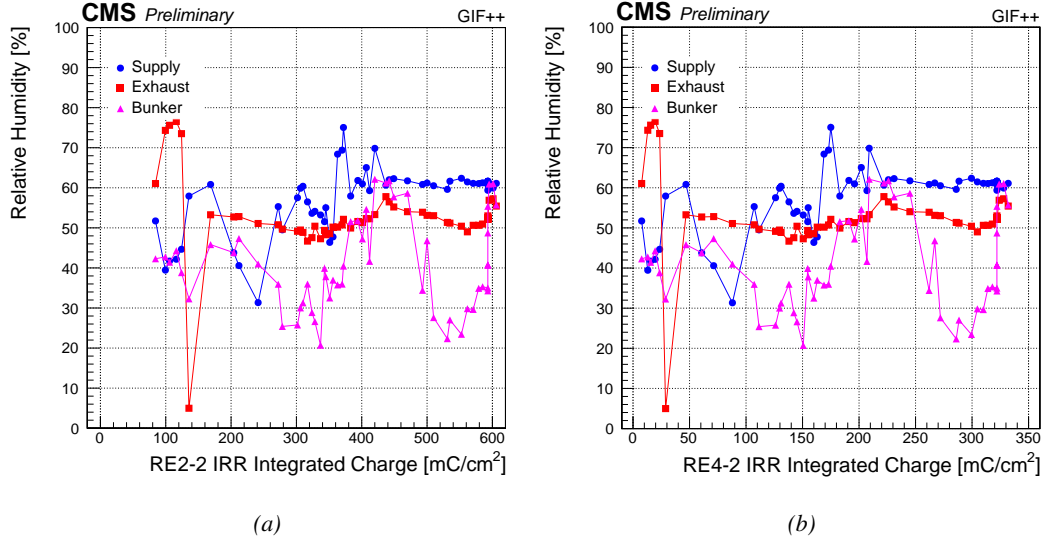


Figure 5.52: Monitoring of the gas relative humidity at the level of the supply and of the exhaust of T1 and ambiant relative humidity at the GIF++ during the source scans.

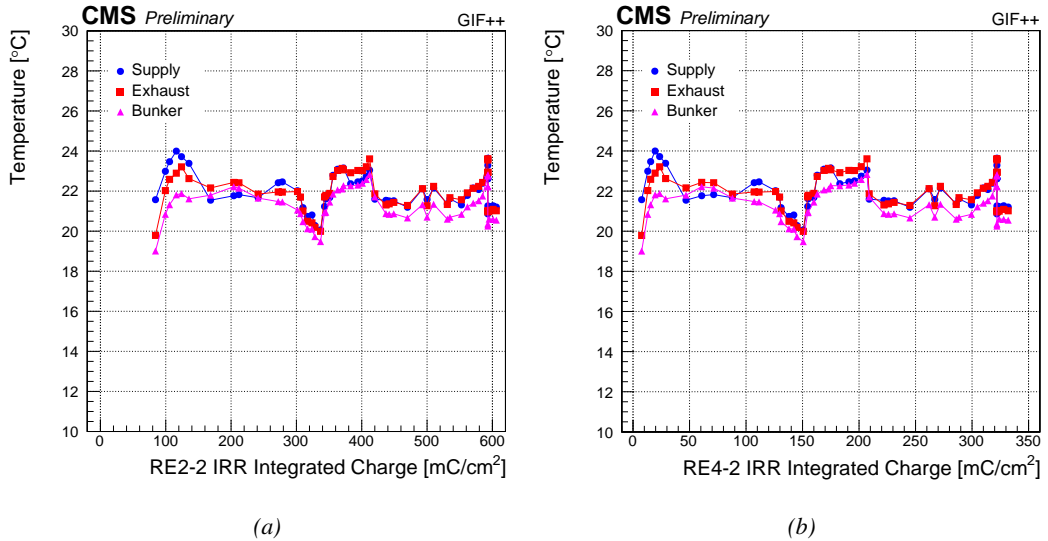


Figure 5.53: Monitoring of the gas temperature at the level of the supply and of the exhaust of T1 and ambiant temperature at the GIF++ during the source scans.

4396 Comparing the trends visible in Figure 5.50 to the monitoring of the different environmental
 4397 parameters, it would seem that the temperature variations may be able to explain most of the fluctuations.
 4398 This assumption is confirmed by a PCA performed on data sets composed for each detector
 4399 of the monitored environmental parameters and of the its current density and gamma rate data. The

4400 corresponding Scree plot is showed in Figure 5.55. The dimension reduction for this data set is less
 4401 trivial as expected.

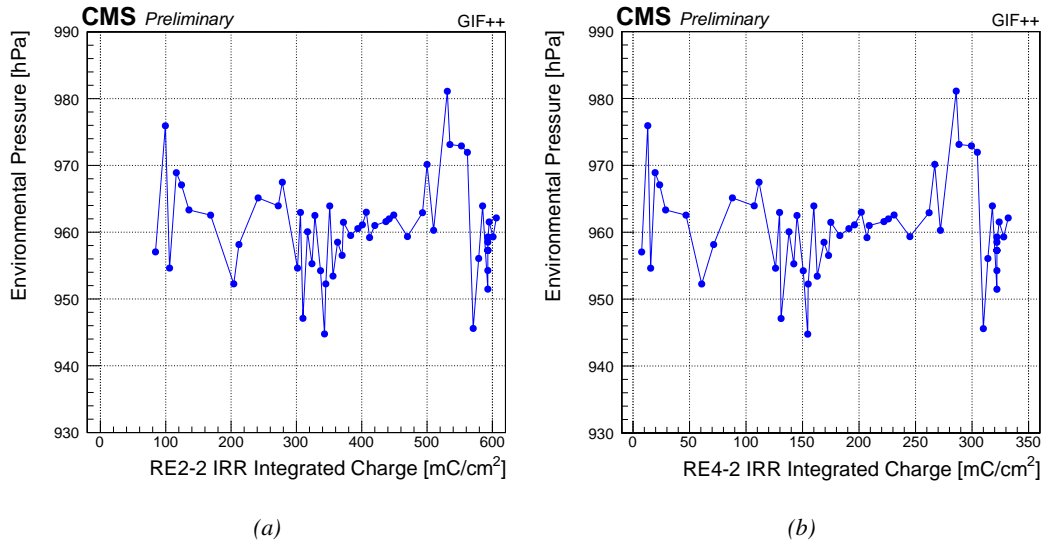
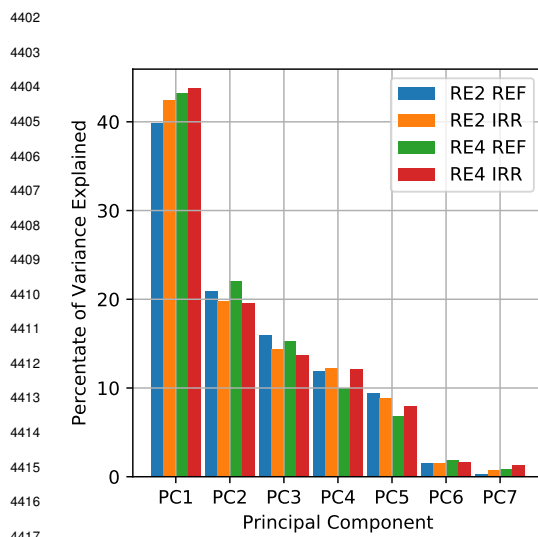


Figure 5.54: Monitoring of the environmental pressure at the GIF++ during the source scans.



4418 Figure 5.55: Scree plot corresponding to the PCAs per-
 4419 formed on each RPC data set to study the influence of the
 4420 environmental parameters in the fluctuation of the cur-
 4421 rent densities and gamma rates.

4422 density and gamma rate vectors in the principal component eigenvector space with the environmental
 4423 parameters vectors are summarized. The linearity between current density and gamma rate is again
 4424 visible. Moreover, the temperature seems to always be a positive source of variation for the current
 4425 density and the gamma rate.

Nevertheless, most of the variation in current densities and gamma rates is held by the first principal component of the PCA basis for all four detectors, as can be understood from the Score plots presented in Figure 5.56. The Score plots show for each principal component the decomposition of its corresponding eigenvector in terms of the variables of the original data set normalised to the eigenvalue associated to the eigenvector. The eigenvectors represent the directions of maximum variance. Hence, the *strength* of each original variable leads to its variability along this direction.

Based on the information of Figure 5.56, the first principal component can be interpreted as the variations directly linked to the fluctuations in current density and gamma rate. This statement is supported by Table 5.6 in which the values of the scalar products of the current

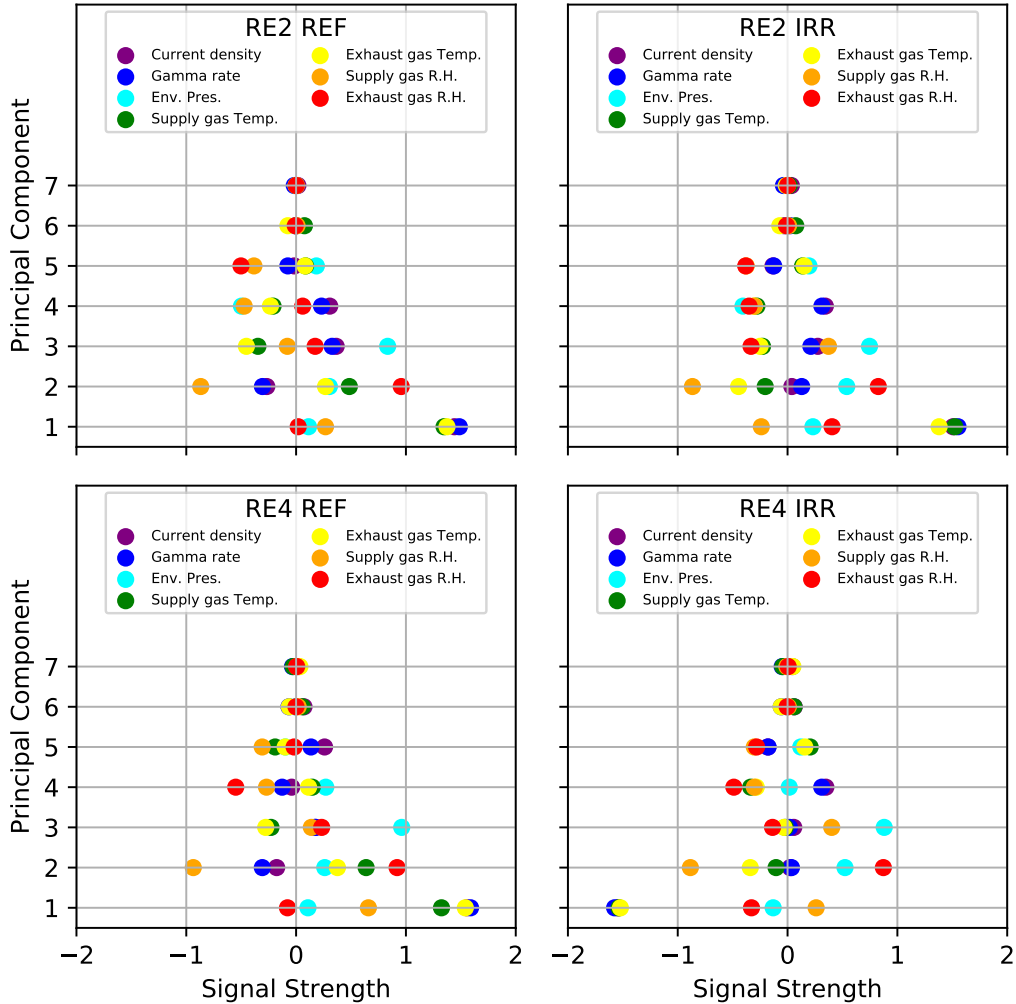


Figure 5.56: Score plots corresponding to the PCAs performed on each RPC data set to study the variations in current density and gamma rate.

Variables	Current density				Gamma rate			
	RE2 REF	RE2 IRR	RE4 REF	RE4 IRR	RE2 REF	RE2 IRR	RE4 REF	RE4 IRR
Env. Pres.	0.21	0.38	0.21	0.19	0.20	0.40	0.16	0.16
Bunker Temp.	1.83	2.01	2.69	2.66	1.93	2.03	2.76	2.75
Bunker air R.H.	-0.83	-0.31	-0.38	0.26	-0.82	-0.23	-0.26	0.35
Supply gas Temp.	1.91	2.42	2.31	2.64	2.00	2.48	2.30	2.73
Exhaust gas Temp.	2.03	2.26	2.81	2.76	2.13	2.28	2.86	2.85
Supply gas R.H.	0.45	-0.33	1.18	-0.39	0.56	-0.42	1.40	-0.40
Exhaust gas R.H.	-0.23	0.43	-0.29	0.40	-0.25	0.57	-0.34	0.46

Table 5.6: Summary of the scalar product between the current density and gamma rate vectors, and the environmental parameters vectors in the principal component eigen vector space.

The contribution of the atmospheric pressure is always significantly smaller but consistent and could be a source of positive feedback. The relative humidity of the gas and of the air in the bunker

on the other hand doesn't provide a consistent feedback but it can be noted that the role of the supply and exhaust humidity seem to have an opposite effect in the case of the reference detectors than in the case of the irradiated detectors.

It is safe to conclude that the voltage correction performed at the GIF++ is not able to account for the high variability of the temperature in the bunker and, hence, of the gas mixture the detectors are operated with. The pressure on the other hand does not play a great role in affecting the RPC operation as the voltage correction was improved to efficiently take into account this parameter [234]. The environmental conditions in the CMS cavern are much more stable in terms of temperature providing an explanation for the less refined temperature correction on the applied voltage as discussed in Section 3.4 of this document.

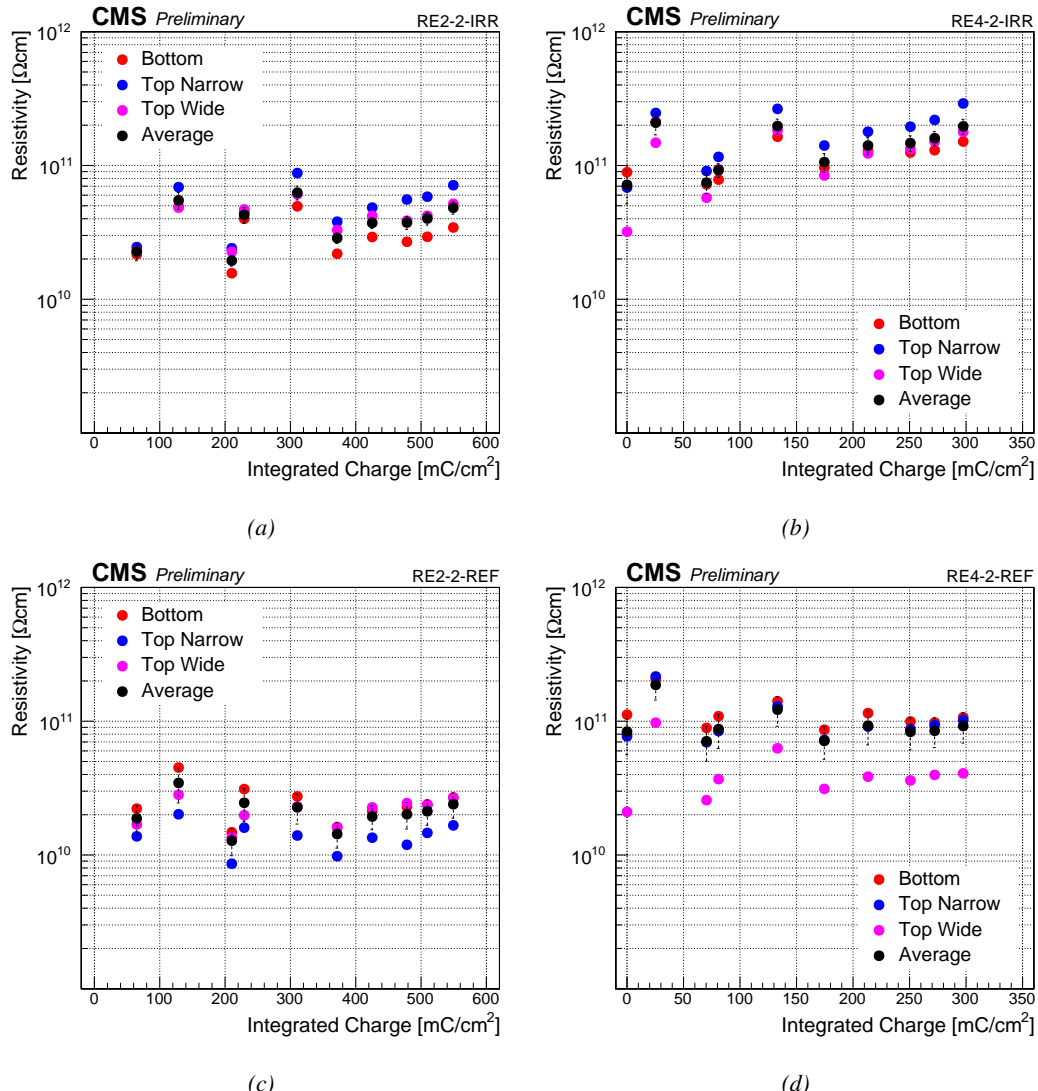


Figure 5.57: Monitoring through argon scans of the resistivity with increasing integrated charge for the RE2 detectors (a) and (c) and the RE4 detectors (b) and (d) installed at the GIF++.

4438 Aside of the fluctuations due to the insufficient temperature correction, it seems that both the
 4439 current densities and gamma rate of the irradiated detectors tend to decrease with time. The reference
 4440 detectors features a more stable operation through time. Comparing the evolution of the current
 4441 densities and of the gamma rates to the monitored resistivity showed in Figure 5.57 may explain the
 4442 decrease observed for the irradiated chambers and the more stable behaviour of the reference ones.
 4443 An increase of resistivity is observed for both the irradiated detectors whose average resistivity went
 4444 from $2.27 \times 10^{10} \Omega \text{ cm}$ for the RE2 and from $7.17 \times 10^{10} \Omega \text{ cm}$ to $1.96 \times 10^{11} \Omega \text{ cm}$ for the
 4445 RE4. The average resistivity of the reference RE2 chamber from $1.88 \times 10^{10} \Omega \text{ cm}$ but is still
 4446 compatible with a stable resistivity due to the wide error bars. On the contrary, the average resistivity
 4447 of the reference RE4 is more or less at the same level at the time of writing ($9.22 \times 10^{10} \Omega \text{ cm}$) than
 4448 it was at the start of the longevity program ($8.36 \times 10^{10} \Omega \text{ cm}$). The differences in increase rate of
 4449 the irradiated chambers with respect to the reference ones can be seen in Figure 5.58. It is clear that
 4450 both the current density and the gamma rate of the irradiated detectors decreases relatively to the
 4451 reference ones. This is consistent with the relative increase in average resistivity of the irradiated
 4452 chambers with respect to the reference ones.

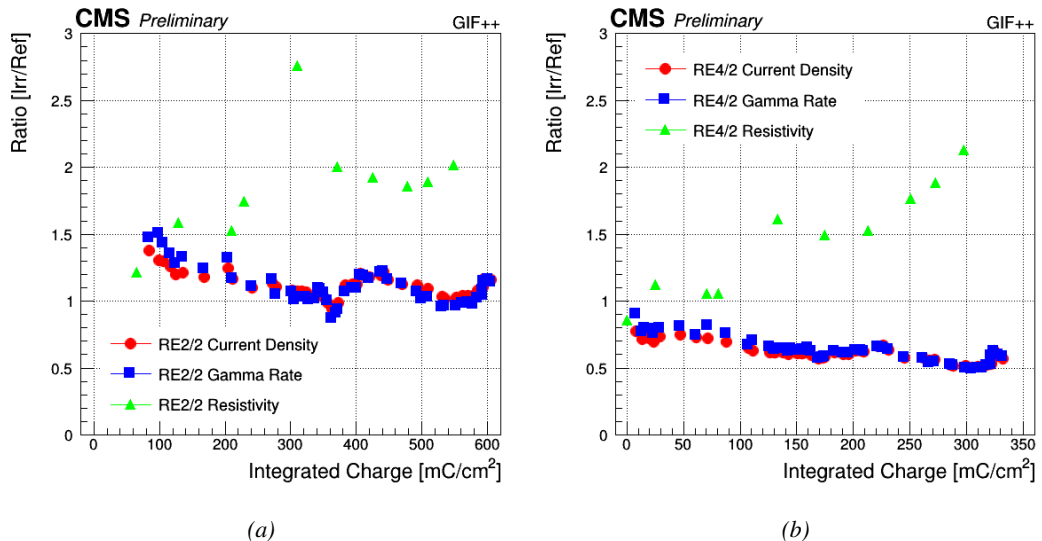


Figure 5.58: "Irradiated over Reference" parameter ratios (current densities, gamma rates and resistivities) as a function of the integrated charge for the RE2 5.58a and the RE4 5.58b detectors installed at the GIF++.

4453 In addition to the decrease of the irradiated detectors current densities and gamma rates with
 4454 respect to the reference RPCs, the fluctuation that can be observed in the ratios could be related to
 4455 the fluctuations of gas humidity observed in Figure 5.52. The effect is seems clearer in the case of
 4456 the RE2 detectors than in the case of the RE4. A PCA is once again performed on updated RPC
 4457 data sets. The single current densities and gamma rates are this time replaced by the "Irradiated over
 4458 Reference" current density and gamma rate ratios. The Scree plot in Figure 5.59 shows a slightly
 4459 different distribution of the variability along the principal components in both cases.
 4460 The Score plots in Figure 5.60 confirms the difference noticed in the Scree plot. Indeed, for the RE2,
 4461 the first principal component mainly shows variability of the temperatures and of the supply relative
 4462 humidity but there is no correlation with the current density or the gamma rate ratios. In fact, their
 4463 variability seems mainly contained in the second principal component together with the variability
 4464 of the bunker and of the exhaust relative humidity. The interpretation of the Score plot in the case of
 4465 the RE4 is much more complex and could be due to the much smaller amplitude of the fluctuation

of the ratios with respect to the RE2. When the environment relative humidity was playing a great role for the RE2, it seems that most parameters have a non negligible effect on the RE4.

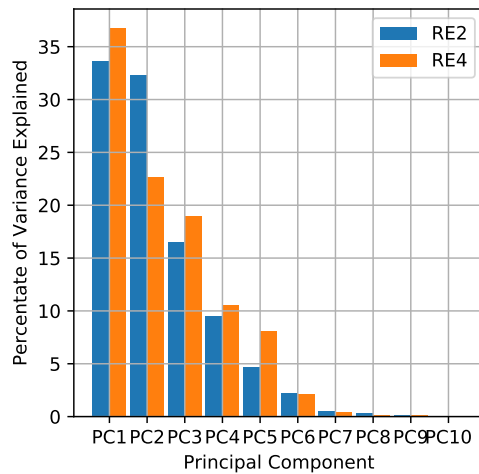


Figure 5.59: Scree plot corresponding to the PCAs performed on each RPC data set to study the influence of the environmental parameters in the fluctuation of the current densities and gamma rates.

end gas connectors are different. The plastic material of the gas connectors at the level of the gas gaps could for example have a different porosity in between both detector types. Or the tightness of the gas connections is simply of better quality for the RE4 than for the RE2. As a matter of fact, it is known at CMS that the RE4 detectors have a significantly lower gas leak rate as a whole than the rest of the CMS RPC sub-system. Based on this information, the RE2 detectors placed at the GIF++ could have a higher chance of having a gas leak. In the case there are gas leaks, the gas leak of the RE2 detectors could also be bigger than the gas leak of the RE4. Such gas leaks would result in a possible humidity exchange between the air inside of the bunker and the gas mixture inside of the detector as well as a contamination of the mixture by with air.

In conclusion, once the fluctuations of the current densities and gamma rate have been understood as a consequence of the imperfect temperature correction, it remains that the resistivity of the irradiated detectors is decreasing with respect to the reference ones. A better control of the relative humidity in the bunker or an investigation for gas leaks on the detectors could help to mitigate the observed decrease of resistivity of the irradiated electrodes.

The information provided by Table 5.7 which summarizes the scalar products between the current density and the gamma rate ratios vectors, and the environmental parameters vectors, reaches a similar conclusion. The effect of the bunker and of the exhaust relative humidity is clear for the RE2 where the fluctuation is the strongest. But no similar conclusion can be made for the RE4 in which all parameters provide a signal. The PCA has failed to reveal an effect of the humidity for the RE4 even though the fluctuation is likely to have the same origin than the one observed for the RE2 as the dates coincide.

The difference between the RE2 and the RE4 detectors is their manufacturing dates. As was already said, the RE2 detectors were manufactured prior to the start of the LHC while the RE4 were manufactured and installed in CMS during LS1. It is not impossible that the providers of the different parts such as the gas connectors of the gas gaps and the on front-

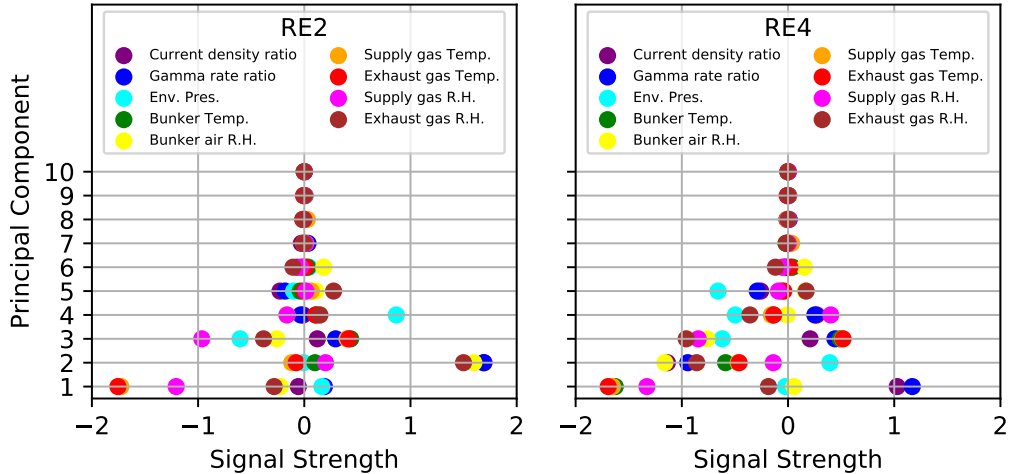


Figure 5.60: Score plots corresponding to the PCAs performed on each RPC data set to study the variations in current density and gamma rate ratios of the irradiated chambers with respect to the reference ones.

Variables	Current density ratio		Gamma rate ratio	
	RE2	RE4	RE2	RE4
Env. Pres.	-0.09	-0.57	-0.17	-0.61
Bunker Temp.	0.33	-0.93	-0.03	-1.15
Bunker air R.H.	2.65	1.17	2.56	0.77
Supply gas Temp.	-0.07	-1.08	-0.42	-1.28
Exhaust gas Temp.	0.02	-1.14	-0.34	-1.34
Supply gas R.H.	0.29	-1.25	-0.17	-1.67
Exhaust gas R.H.	2.45	0.45	2.31	0.04

Table 5.7: Summary of the scalar product between the current density ratio and gamma rate ratio vectors, and the environmental parameters vectors in the principal component eigen vector space.

5.3.7.2 Evolution of the detectors performance

Throughout the longevity study performed at the GIF++, the muon beam has been used eight times to measure the detector performances. The first test beam period happened before the start of the irradiation program in October 2015. The remaining test beam period all happened at different until end of 2018 and the start of LS2. Due to the fact that no irradiation was possible on the RE4 detector before end of 2016, the data of the two test beam periods of 2016 will not be showed nor discussed along the following paragraphs. The discussion will revolve around the data taken during the five remaining test beam periods at which the RE2 and RE4 detectors had respectively reached 18, 31, 45, 51, and 57%, and 5, 11, 21, 26 and 30% of the required 0.84 C/cm^2 .

The test beam periods are the occasion to monitor the efficiency, mean muon cluster size and gamma rate at working voltage. This way, the evolution of the efficiency and of the mean muon cluster size at working voltage as a function of the gamma hit rate can be studied with increasing integrated charge. Ageing effects will be expected to bring changes in the behaviour of the detector such as higher working voltage, lower efficiency at working voltage, lower rate capability or lower mean muon cluster size at working voltage.

From the efficiency scans, the first parameter to be extracted from the sigmoid fits is the working

voltage. Then only the efficiency is computed using the sigmoid fit and the mean muon cluster size is interpolated from the closest voltage values. The working voltage is also used as a reference to interpolate the gamma rate, gamma cluster size, gamma multiplicity and charge deposition per gamma with better accuracy from the rate scans. The choice for the interpolation method is mainly motivated by the fact that these quantities have a close to linear behaviour with increasing voltage in the region of interest, as can for example be seen in Figures 5.29b and 5.30d.

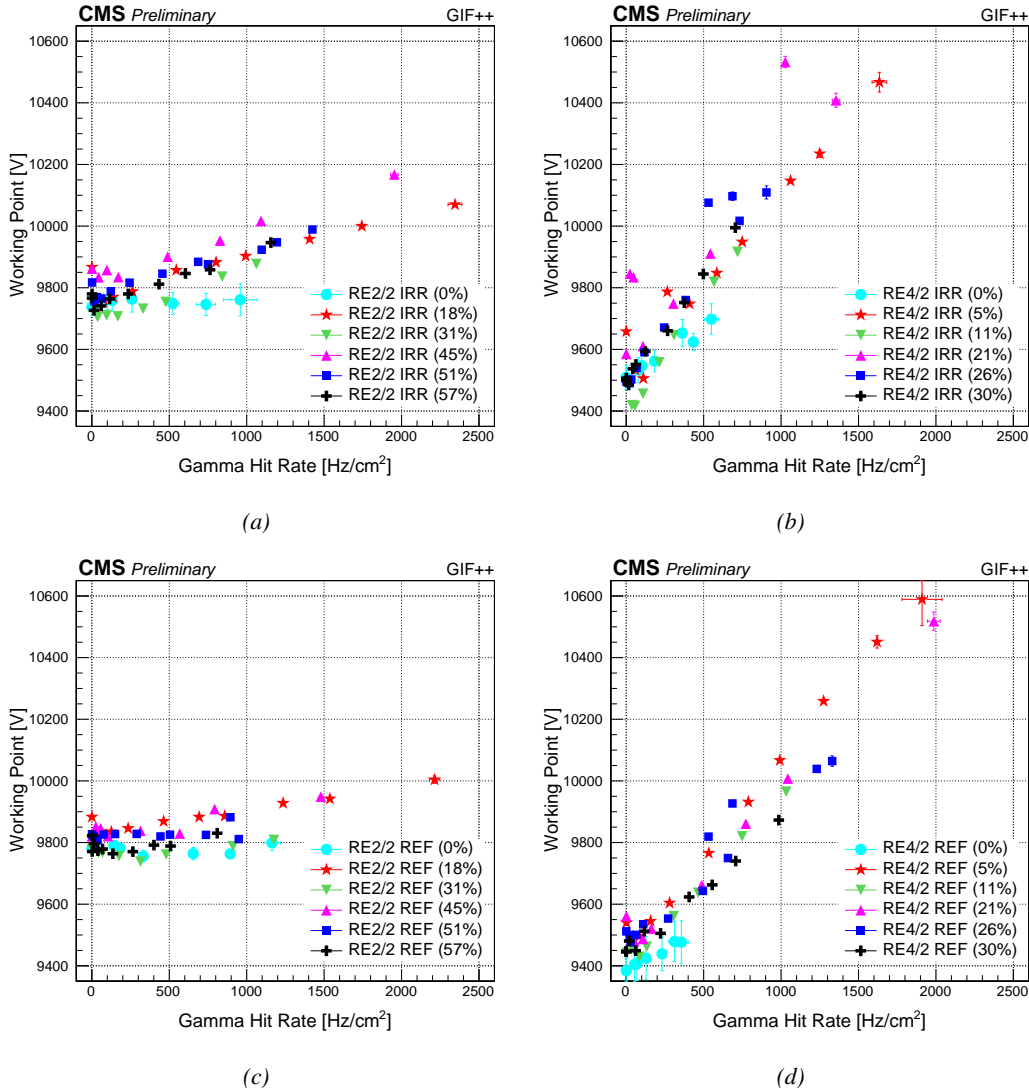


Figure 5.61: Superposition of the working voltage as a function of the gamma rate measured in each of the CMS RPCs installed at the GIF++ during the six test beam periods.

The values of working voltage as a function of the gamma rate in the different testbeam periods are showed in Figure 5.61. It is important to note that the working voltage shift of the RE4 with increasing gamma rate (400 V to 600 V per 1 kHz/cm²) is bigger than in the case of the RE2 detectors (150 V to 250 V per 1 kHz/cm²). Depending on the testbeam, the working voltage can vary

4531 up to approximately 100 V. Both the difference in behaviour of the RE2 and RE4, and the working
 4532 voltage variation from one period to another could be related to the RPC resistivity. Indeed, as al-
 4533 ready showed in Figure 5.57, the resistivity of the RE4 detectors is several times higher than that of
 4534 the RE2. It is then likely that the rate capability of the RE4 chambers is lower than that of the RE2
 4535 causing a stronger voltage shift with increasing background rate. The difference in effective voltage
 4536 shift between the RE2 and RE4 chambers is showed in Figure 5.62. For each testbeam period, the
 4537 sigmoid obtained without irradiation is compared with the sigmoid at a gamma rate as close as pos-
 4538 sible from the certification value of 600 Hz/cm^2 . The shift is clearly bigger in the case of RE4 RPCs.
 4539

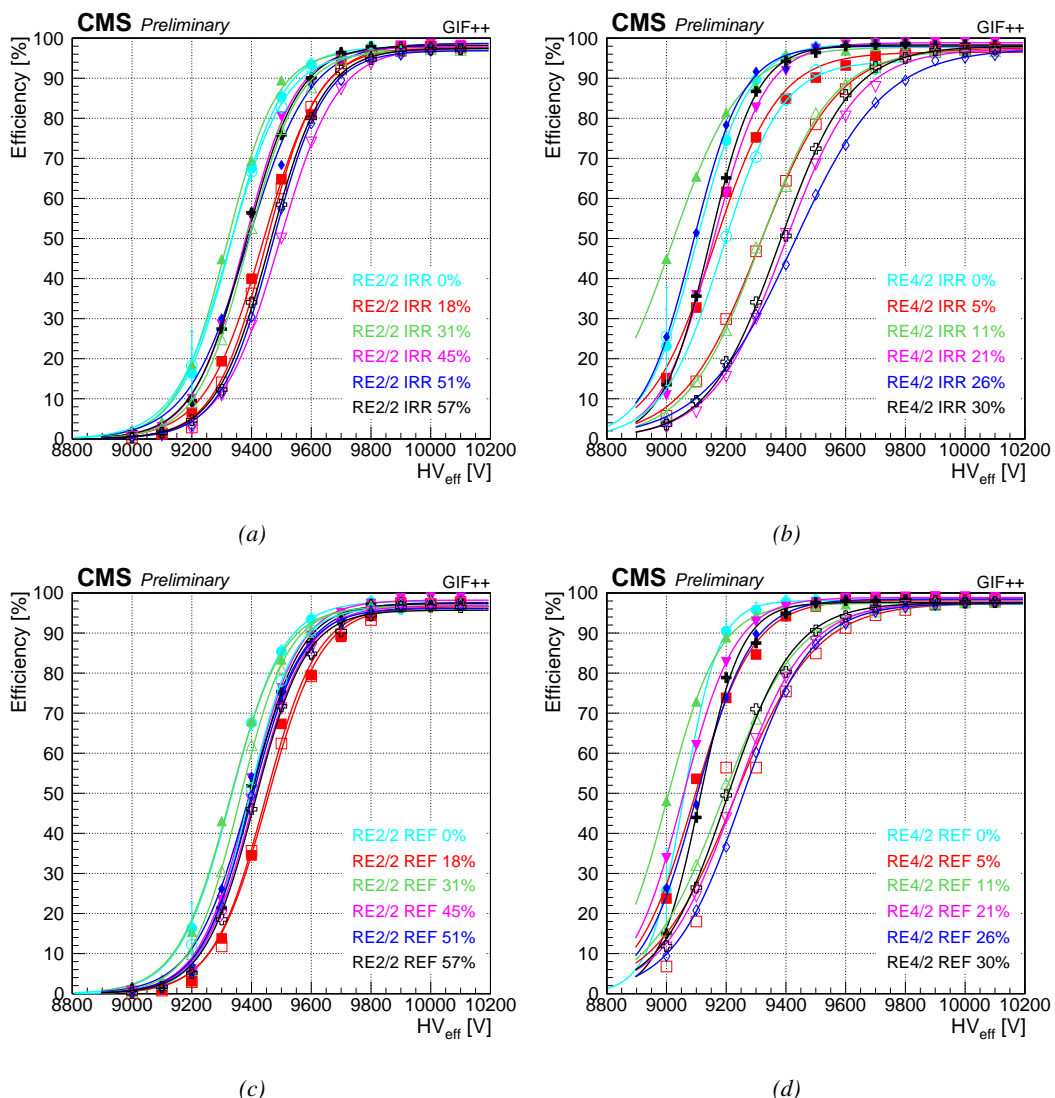


Figure 5.62: Superposition of the efficiency sigmoids as a function of the effective voltage measured with the CMS RPCs installed at the GIFF++ during the six test beam periods with and without irradiation. The data without irradiation is showed with full symbols whereas the data with irradiation is showed with open symbols.

The approximate resistivity of the electrodes, presented in Figure 5.63, has been extracted from the efficiency scans using the procedure described in Section 5.3.6 of this chapter. The extracted value is compared to the mean resistivity of the partition C of the detectors installed at the GIF++, where the beam passes. Except for the reference RE2 chamber for which the results are a factor 2 bellow what would be expected, the extraction indeed provides a value comparable to the mean value obtained in this partition using the argon scans.

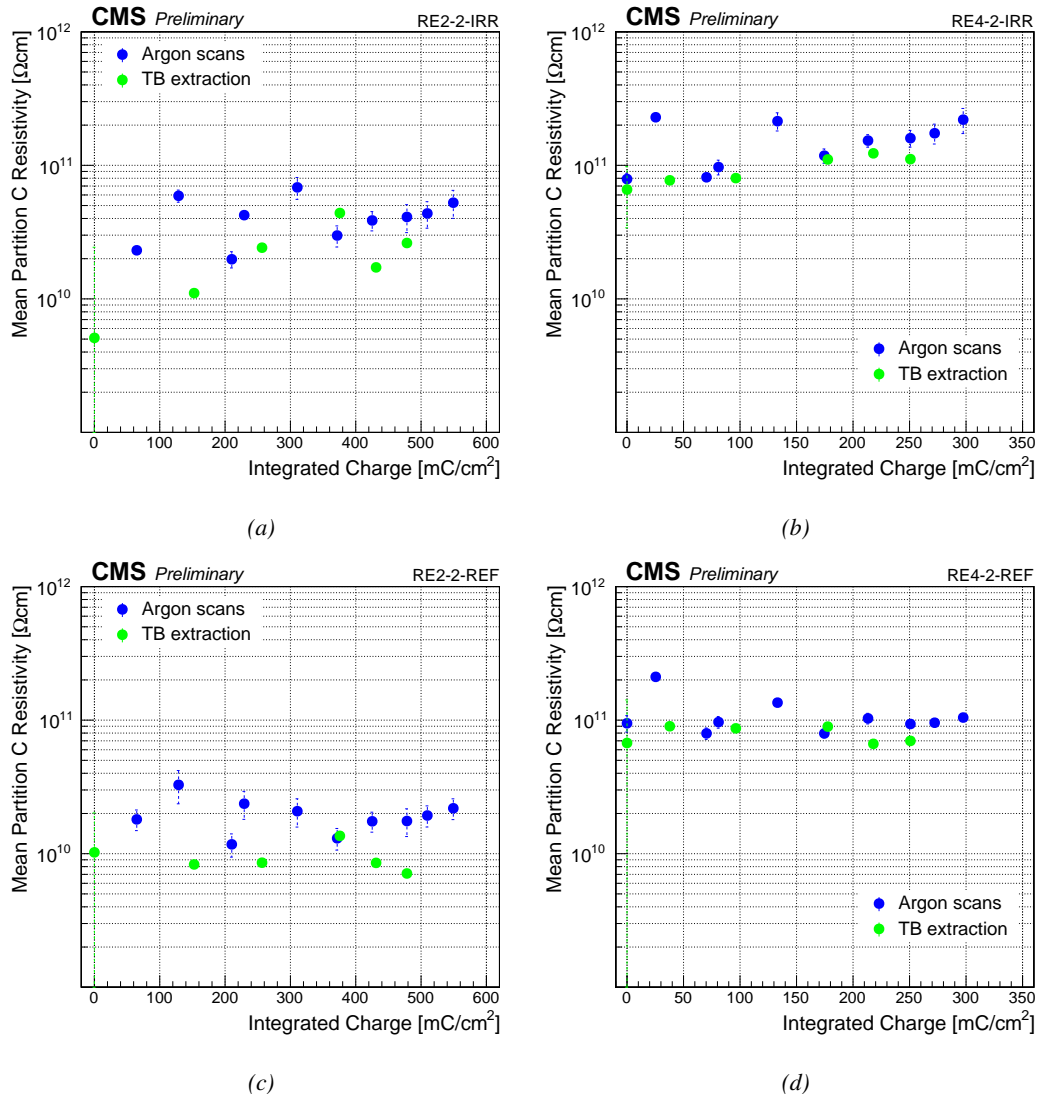


Figure 5.63: Comparison of the mean resistivity of measured in partition C with Argon Scans (blue) and of the values extracted from the efficiency sigmoids taken during the test beam periods (green).

The resistance of the detectors obtained with this method are used as in Equation 5.11 to compare the behaviour of the RPCs without the bias brought by the resistivity variation. The results are showed in Figure 5.64. Comparing the results using the voltage drop over the gas volume only, the detectors so far seem not to display any loss of performance with increasing integrated charge at a

background rate near the certification value of 600 Hz/cm^2 .

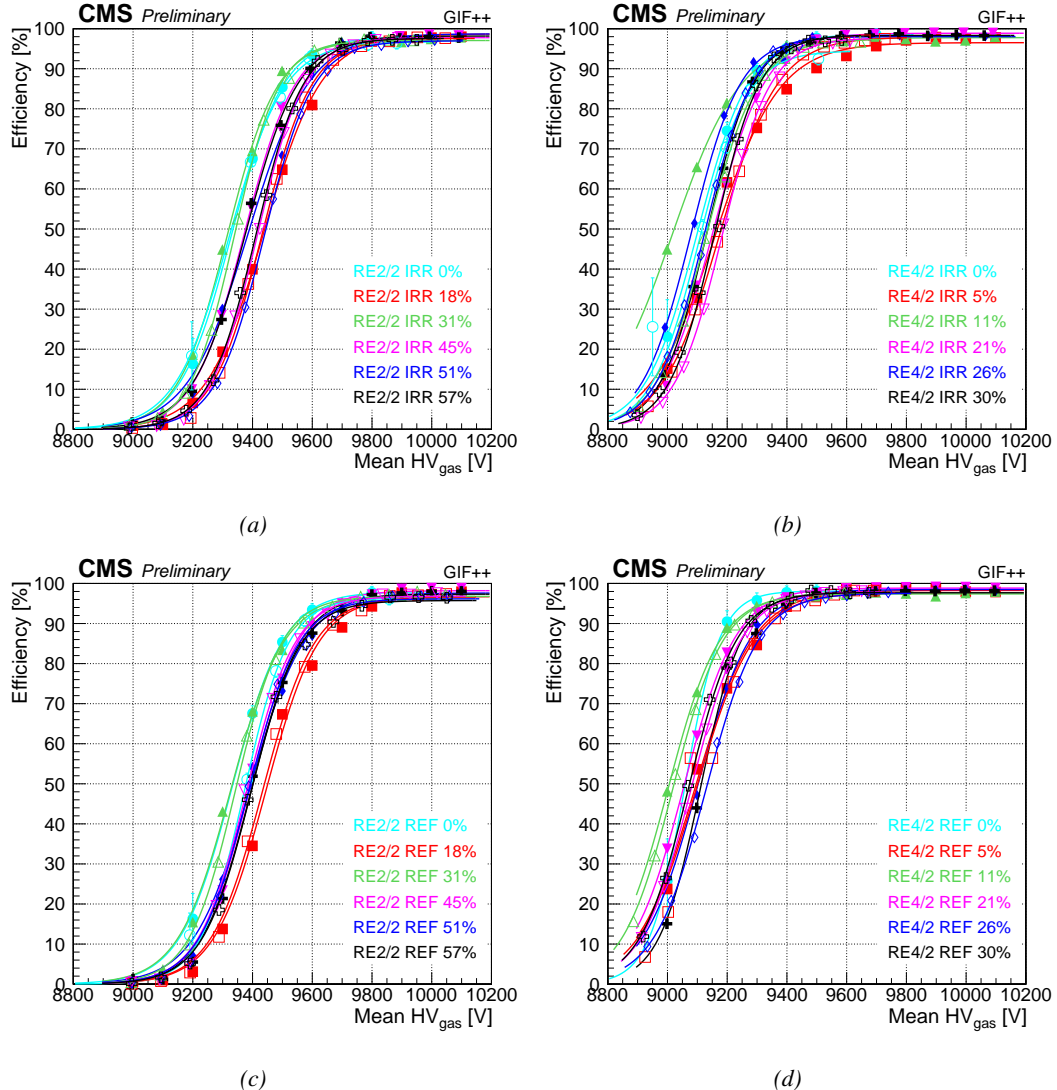


Figure 5.64: Superposition of the efficiency sigmoids as a function of the voltage drop over the gas volume measured with the CMS RPCs installed at the GIF++ during the six test beam periods. The data without irradiation is showed with full symbols whereas the data with irradiation is showed with open symbols.

Nevertheless, extracting the resistivity by the means of the estimated voltage shift due to the loss of charge in the electrode is not a robust enough method as it tends to overcorrect the voltage drop in the gas as can be seen from Figure 5.65. The Figure, together with Figure 5.61, still suggests that the behaviour of the detectors didn't evolve yet due to irradiation. The overcorrection is mainly visible for the RE4 detectors and can be due to an overestimation of the detectors resistance though Figure 5.63 does not support this interpretation. Other than an overestimated resistance, it is possible that the current in the detectors is larger than what would be expected from simply using Ohm's law.

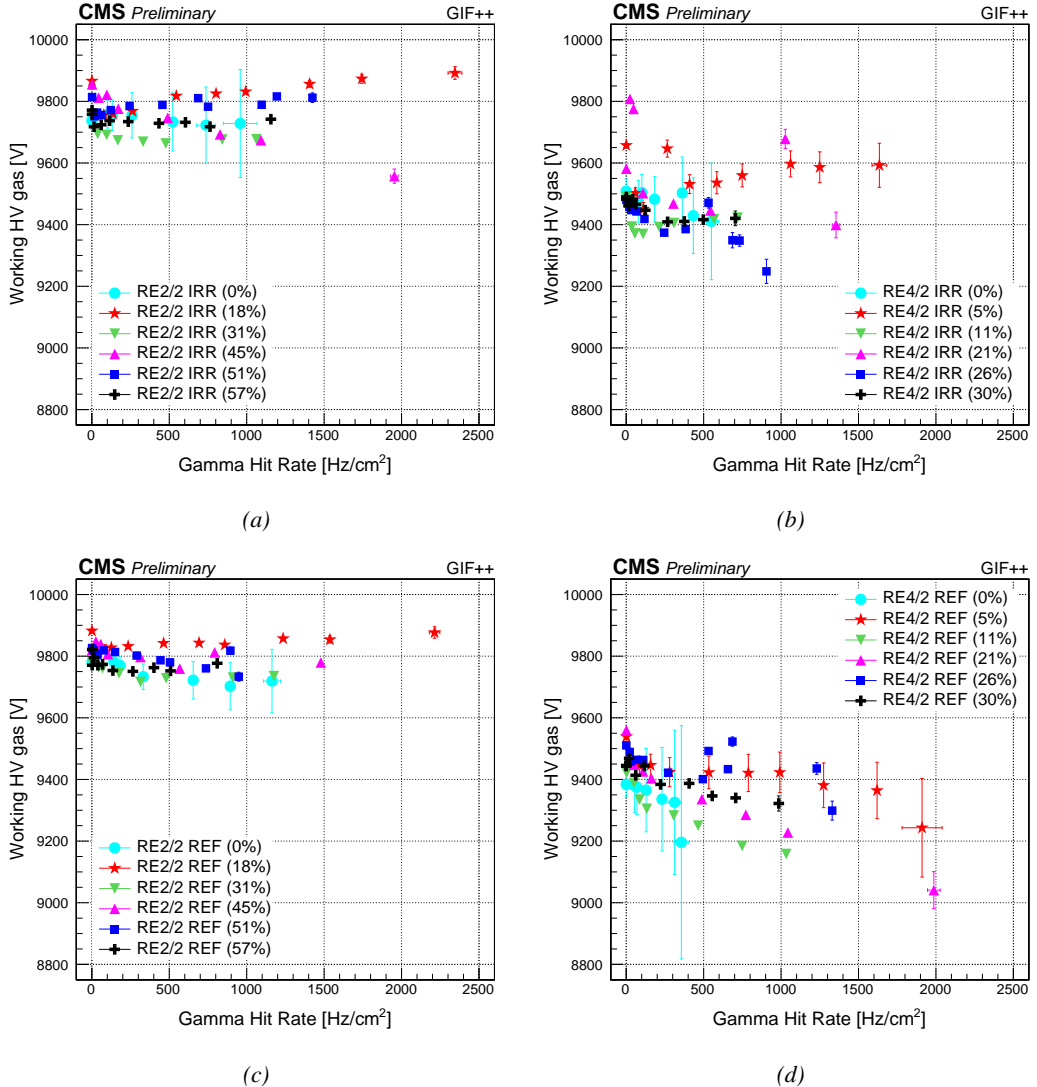


Figure 5.65: Superposition of the gas voltage drop corresponding to the computed working voltage as a function of the gamma rate measured in each of the CMS RPCs installed at the GIFF++ during the six test beam periods.

4558 Figures 5.66 and 5.67 show the evolution of the efficiency and of the mean muon cluster size
 4559 at working voltage with increasing background hit rate. There is no loss of rate capability to be
 4560 observed. The efficiencies at working voltage show the same behaviour during the last testbeam
 4561 period than during the previous ones as long as the background rate is below 1000 Hz/cm². The
 4562 efficiency of all four detectors does not decrease beneath 95%. Beyond this value, too few points
 4563 were taken to be able to discuss the data. **Should I even show the data beyond 1000 Hz/cm²? I**
 4564 **could simply stop all the plots at 1000 Hz/cm² as this is the only range that was consistently**
 4565 **measured.**

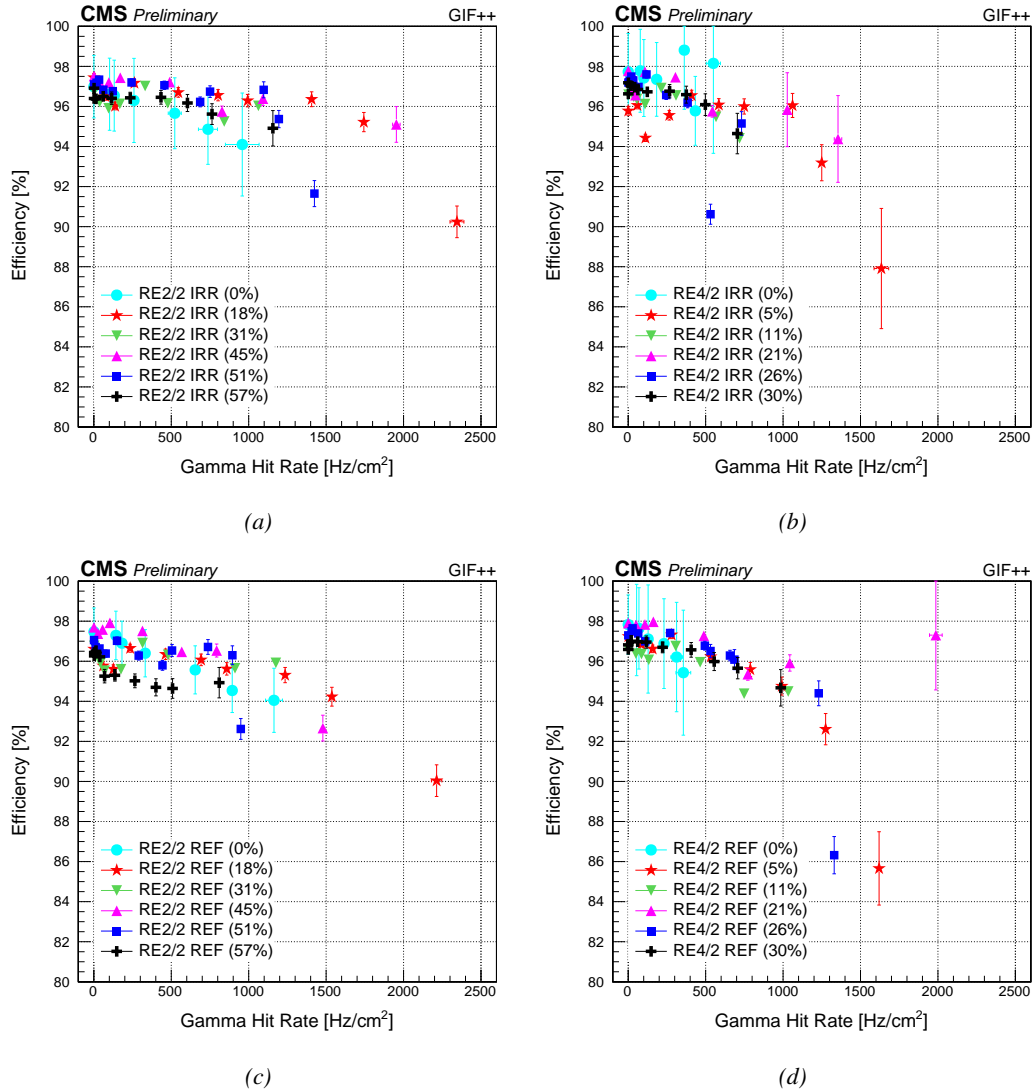


Figure 5.66: Superposition of the efficiency at working voltage as a function of the gamma rate measured in each of the CMS RPCs installed at the GIF++ during the six test beam periods.

4566 The same conclusion can be made looking at the mean muon cluster size. There is no difference
 4567 between the irradiated detectors and the reference ones for these parameters. The mean cluster size
 4568 is consistent from one testbeam period to the other except for the data gathered in October 2018
 4569 corresponding to 57% of integrated charge for the RE2 detector and 30% for the RE4. The mean
 4570 muon cluster size is consistently bigger during this period for all four detectors. To understand the
 4571 phenomena, a study of the beam hit profile in the detectors and of the event cluster size and cluster
 4572 multiplicity for each recorded trigger was performed with the source OFF data. The usage of data
 4573 without irradiation allows to study the potential effects that are not correlated with the background
 4574 radiation while focusing on the data corresponding to the time arrival of the muon beam provides
 4575 with information regarding the beam quality. Table 5.8 reveals that during the last testbeam the
 4576 detectors were subjected to higher fraction of beam events with a cluster size greater than 3 and with

4577 a greater number of reconstructed clusters per beam event. The only possible explanation is then that
 4578 the beam contained hadrons. Some of the hadrons or their products are likely to decay before the
 4579 chambers or while passing through the setup and produce multiple clusters per event or simultaneous
 4580 detections in neighbour channels artificially increasing the reconstructed cluster size.

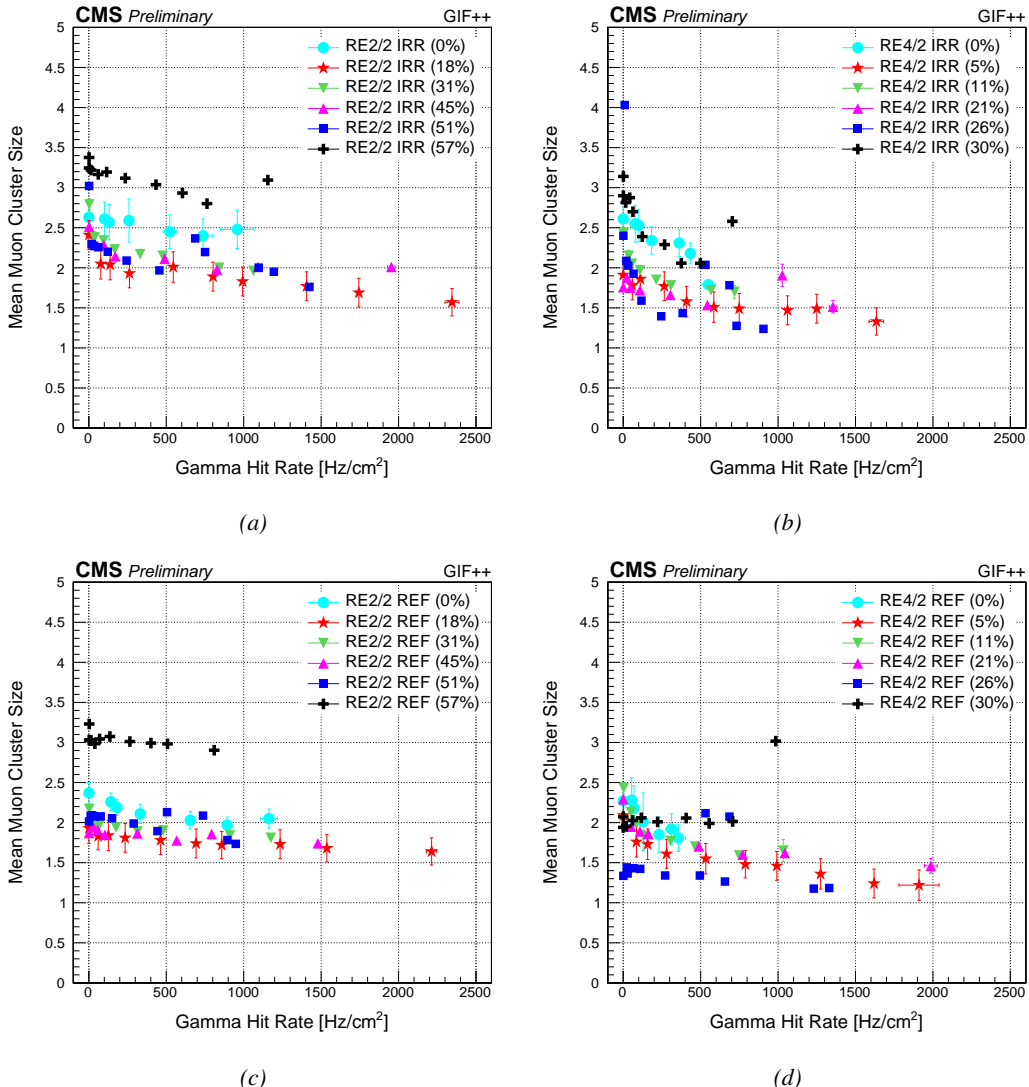


Figure 5.67: Superposition of the cluster size at working voltage as a function of the gamma rate measured in each of the CMS RPCs installed at the GIF++ during the six test beam periods.

Integrated charge in RE2	18%	31%	45%	51%	57%
Reference RE2					
Effective voltage (V)	9900	9800	9800	9800	9800
Mean cluster size	2.28	2.12	1.96	2.30	3.24
Mean cluster multiplicity	1.17	1.20	1.15	1.26	1.47
Percentage of events with...					
... cluster size > 3	6.5	5.7	5.7	8.6	21.4
... cluster multiplicity > 2	2.3	2.1	2.2	3.7	11.5
Irradiated RE2					
Effective voltage (V)	9900	9800	9900	9800	9800
Mean cluster size	2.80	2.73	2.70	2.67	3.55
Mean cluster multiplicity	1.06	1.04	1.05	1.10	1.29
Percentage of events with...					
... cluster size > 3	12.6	11.3	11.7	11.7	24.4
... cluster multiplicity > 2	1.2	1.1	0.8	2.1	7.0
Integrated charge in RE4	5%	11%	21%	26%	30%
Reference RE4					
Effective voltage (V)	9700	9500	9600	9500	9500
Mean cluster size	2.13	2.00	2.48	2.32	2.82
Mean cluster multiplicity	1.07	1.04	1.07	1.11	1.37
Percentage of events with...					
... cluster size > 3	8.0	6.4	9.1	9.9	19.7
... cluster multiplicity > 2	2.0	1.6	1.7	2.5	10.8
Irradiated RE4					
Effective voltage (V)	9500	9400	9600	9500	9400
Mean cluster size	2.34	2.27	1.86	2.18	3.03
Mean cluster multiplicity	1.15	1.06	1.06	1.11	1.38
Percentage of events with...					
... cluster size > 3	8.0	6.7	5.3	7.7	20.4
... cluster multiplicity > 2	2.9	1.8	1.8	2.5	10.4

Table 5.8: Summary of the percentage of large reconstructed clusters and of events with more than two reconstructed clusters of the CMS RPCs installed at the GIF+ during the five test beam periods after the start of irradiation. The HV points closest to the working voltage are used.

6

4581

4582

4583

Improved RPC investigation and preliminary electronics studies

4584 The extension in the endcap of the RPC sub-system towards higher pseudo-rapidity will bring the
4585 new detectors to be exposed to much more intense background radiations due to the proximity of the
4586 detectors with the beam line (Figure 4.5). The challenge will be to produce high counting rate de-
4587 tectors with limited ageing rate to ensure a stable operation of the detector over a period longer than
4588 ten years. In Chapter ?? was discussed the influence of the detector design (number and thickness
4589 of gas volumes, OR system, etc...) on the charge deposition and rate capability. Nevertheless, this
4590 question can also be addressed from the electronics point of view as a better signal-to-noise ratio
4591 would also mean the possibility to greatly lower the charge threshold on the signals to be detected,
4592 allowing to use the detector at lower gain, hence lowering the charge deposition per avalanche in the
4593 gas volume. Cardarelli showed that the production of low-noise fast FEEs could help decreasing the
4594 charge deposition per avalanche at working voltage by an order of magnitude, virtually increasing
4595 the life expectancy of such a detector in the same way [281].

4596 6.1 FEE candidates for the production of iRPCs

4597 The extension of the third or fourth endcap disks with improved RPCs has been presented in
4598 Chapter ?? together with the expected background levels (Figure 4.18). An important piece of
4599 these iRPCs will be the Front-End Electronics that will equip the chambers. A fast, low-jitter and
4600 low-charge sensitive electronics will help reducing further the charge deposition in the detector by
4601 making it possible to operate at lower gain.

4602 In the context of the CMS Muon Upgrade, two FEE solutions have been considered to equip the
4603 iRPCs. The baseline for the RPC upgrade is based on the PETIROC ASIC, initially for Time-of-
4604 flight (ToF) applications. A back-up solution is also under study and focusses on a new low-noise
4605 preamplifier designed in INFN laboratories in Rome to replace the preamplification stage of the
4606 already existing CMS RPC Front-End Board.

4607 The FEEs that are foreseen to equip the new RPCs need to be able to detect charges as small as
4608 10 fC. Not only the new electronics need to be fast and reliable, they also should be able to sustain